New Jersey Institute of Technology

Digital Commons @ NJIT

5-31-2018

Fluorescent probes and functionalized nanoparticles for bioimaging: synthesis, photophysical properties and applications

Xinglei Liu
New Jersey Institute of Technology

Follow this and additional works at: https://digitalcommons.njit.edu/dissertations

Part of the Biochemistry Commons, Biomedical Engineering and Bioengineering Commons, and the Chemistry Commons

ABSTRACT

FLUORESCENT PROBES AND FUNCTIONALIZED NANOPARTICLES FOR BIOIMAGING: SYNTHESIS, PHOTOPHYSICAL PROPERTIES AND APPLICATIONS

by
Xinglei Liu

The development of new organic molecular probes with excellent photophysical properties and high fluorescence quantum yields is of considerable interest to many research areas including one- and two-photon fluorescence microscopy, fluorescence-based sensing methodologies, and cancer therapy. Series of organic linear-/non-linear optical molecules including squaraine derivatives, and fluorene derivatives as well as other bioconjugates are designed and synthesized during the doctoral study for the aim of ion detection (Chapter 5), photo dynamic therapy, and deep-tissue imaging (Chapter 4). These optical probes are capable of absorbing light in the near infrared (NIR) window and thus have deeper penetration and cause less photodamage to the biological sample (Chapter 2). To realize the specific targeting, molecules are functionalized by peptide conjugation such as the recruitment of RGD-peptide.

There have been numerous fluorescent probes reported over the past few decades and many suffer from the ability to introduce them into biological systems, undergo fluorescent quenching in aqueous media, or are not biocompatible. Delivery of hydrophobic materials in biological materials into the biological systems, for example, contrast agents or drugs, is an obdurate challenge, severely restricting the use of materials with otherwise advantageous properties. Incorporating promising organic molecules in nanovessicles, nanoparticles, and polymeric carriers to achieve new types of biocompatible

probes and bioimaging is another vital aim for this doctoral research. Combining with powerful imaging methods, such as in *vivo* two-photon fluorescence microscopy (2PFM), vasculature imaging during angiogenesis (Chapter 4), cellular organelles labelling and tracking (Chapter 3, 6) is accomplished using nanostructured fluorescent probes or complex. These represent powerful new tools that should have broad impact as high fidelity fluorescent contrast agents.

FLUORESCENT PROBES AND FUNCTIONALIZED NANOPARTICLES FOR BIOIMAGING: SYNTHESIS, PHOTOPHYSCIAL PROPERTIES AND APPLICATIONS

by
Xinglei Liu

A Dissertation
Submitted to the Faculty of
New Jersey Institute of Technology
in Partial Fulfillment of the Requirements for the Degree of
Doctor of Philosophy in Chemistry

Department of Chemistry and Environmental Science

May 2018

APPROVAL PAGE

FLUORESCENT PROBES AND FUNCTIONALIZED NANOPARTICLES FOR BIOIMAGING: SYNTHESIS, PHOTOPHYSCIAL PROPERTIES AND APPLICATIONS

Xinglei Liu

Dr. Kevin D. Belfield, Dissertation Advisor   Date
Dean of College of Science and Liberal Science, and Professor of Chemistry and
Environmental Science, NJIT

Dr. Edgardo Farinas, Committee Member   Date
Associate Professor of Chemistry and Environmental Science, NJIT

Dr. Yong I. Kim, Committee Member   Date
Assistant Professor of Chemistry and Environmental Science, NJIT

Dr. Yuanwei Zhang, Committee Member   Date
Assistant Professor of Chemistry and Environmental Science, NJIT

Dr. Xuan Liu, Committee Member   Date
Assistant Professor of Electrical and Computer Engineering, NJIT

BIOGRAPHICAL SKETCH

Author: Xinglei Liu

Degree: Doctor of Philosophy

Date: May 2018

Undergraduate and Graduate Education:

- Doctor of Philosophy in Chemistry,
  New Jersey Institute of Technology, Newark, NJ, 2018

- Bachelor of Science in Applied Chemistry,
  Shaanxi Normal University, Xi'an, Shaanxi, China, 2013

Major: Chemistry

Presentations and Publications:

T. Liu, X. Liu, W. Wang, et al., Systematic molecular engineering of a series of aniline based squaraine dyes and their structure-related properties. *J. Phys. Chem. C* **2018**, *122*, 3994.

X. Liu and K. D. Belfield, High-selective, far-red emitting squaraine sensor for cyanide detection. *American Physical Society*, 2017 Conference Mid-Atlantic Section, Newark, NJ.

X. Liu, A. Ardizzone, B. Sui, M. Anzola, N. Ventosa, T. Liu, J. Veciana, K. D. Belfield, Fluorenyl-loaded quatsome nanostructured fluorescent probes. *ACS Omega* **2017**, *2*, 4112-4122.

T. Liu, X. Liu, M. A. Valencia, B. Sui, Y. Zhang, K. D. Belfield, Far-red-emitting TED-substituted squaraine dye: synthesis, optical properties, and selective detection of Cyanide in aqueous solution. *Eur. J. Org. Chem.* **2017**, *27*, 3957-3964.

X. Liu, A. Ardizzone, B. Sui, M. Anzola, T. Liu, J. Veciana, K. D. Belfield, Nanostructured quatsomes encapsulating fluorene-derivatives for lysosomal labeling and tracking. *Optics in the Life Sciences Congress*, OSA Technical Digest, paper OmTu3D.4.

S. Wang, Z. Li, X. Liu, S. Phan, F. Lv, K. D. Belfield, S. Wang, K. Schanze, Two-photon absorption of cationic conjugated polyelectrolytes: effects of aggregation and application to 2-photon-sensitized fluorescence from green fluorescence protein. *Chem. Mater.* **2017**, *29*, 3295-3303.

X. Liu, T. Liu, X. Yue, M. Komatsu, K. D. Belfield, RGD-conjugated PMAO Nanoparticles encapsulating a squaraine probe for tumor vasculature imaging. *Optics in the Life Sciences Congress*, OSA Technical Digest, paper OmM4D.5.

B. Sui, X. Liu, M. Wang, K. D. Belfield, A highly selective fluorescence turn-on sensor for extracellular calcium ion detection. *Chem. Eur. J.* **2016**, *22*, 10351-10354.

H. Wang, H. Cui, X. Liu, L. Li, Y. Cao, T. Liu, Y. Fang, Alternative copolymerization of a conjugated segment and a flexible segment and fabrication of a fluorescent sensing film −for HCl in the vapor phase. *Chem. Asian J.* **2013**, *8*, 101-107

To my parents,

Being the only child in the family, my parents still support me for study abroad and leaving the family. I always felt guilty because I can't stay by their side whenever they needed me, and I couldn't accompany them like a "real" daughter. I'm not the person that always say "I love you" to other people, and I always cover my emotions deep in my heart, but this is a great place for me to say love to my parents. Daddy and mommy, 我爱你们 (I love you)!

三十功名尘与土，

八千里路云和月。

莫等闲，白了少年头，

空悲切。

    --岳飞，《满江红》

ACKNOWLEDGMENT

First of all, I want to give special thanks to my advisor, Kevin Belfield. He is not only the academic advisor for me, but also the source of support, inspiration, and power to me. I met Dr. Belfield when I was just an undergraduate in China, and it was his encouragement and trust that made me believe that I can be a Ph. D. student overseas. Later, I was honored to join his group in University of Central Florida for the study of Chemistry in 2013. After Dr. Belfield joined NJIT at 2015, it was my great pleasure to still have the chance to follow him and start my new life in the great tri-state area. During my Ph.D study, Dr. Belfield gave me so much help and guidance in research. Besides, he encouraged me to participate in so many great conference and scientific events, and he would never hesitate to give good reference for me at any time. In summary, Dr. Belfield's exceptional enthusiasm and positive attitude towards research was the driving forces of my graduate career at New Jersey Institute Technology, and I would not be able to finish my doctoral study without his help.

I want to also thank every member of my Committee for their patience, professional advice and help: Dr. Yuanwei Zhang, Dr. Yong Kim, Dr. Edgardo Farinas and Dr. Xuan Liu. I also appreciate the National Science Foundation for the funding and support for my research.

During my doctoral study, members in our group became my best partners. We belong to a friendly and united group. I highly believe that even after graduation, we will still be really good friends for our whole life. Sweety Singh, Tinghan Zhao, Xiangshan Liu, and former members Dr. Taihong Liu and Dr. Xiling Yue, they all helped me a lot not only on research but also in my life. Especially for Dr. Taihong Liu, we came from the

same group in China, he is like a big brother to me, and we worked together in many projects. He taught so many tricks and skills, those that I cannot learn from books or classes. Dr. Xiling Yue is like a mentor to me. She passed on her knowledge and experience to me without conditions. I will remember everyone in this lab; those who helped me and support me during the five years.

Moreover, friends gave me a lot of support, joy, and accompaniment. We, Chinese kids like my age, belong to the "single kids" generation, which means one family is allowed to have only one child. Therefore, we don't have siblings, and friends are sisters and brothers to us. I believe we have closer relationship and deeper communication with friends than our parents' generation. I would like to give special thanks and love to all my sisters and brothers: Ying Du, who always goes to visit my parents every year while I'm away; Xiwen Wang, Jiawei Liu, Yuanhao Wang, Jun Zhang, Chenxi Wang, Jingyi Li, Qian Li, Xudong Hao and Haozhe Zhou, who are my best friends for more than 15 years; Nanami Kikuchi and Alfonso Ballestas, who treated me like a real family when I was in Orlando; Sandy Chen and Dan Yuan, who are my best friends in New Jersey, and they give me uncountable warm and love. They all believed in me and gave me great power while I'm down and blue.

Last, but not the least, parents are my strongest backing. I appreciate their understanding, support and their unconditional love to me. I could not have such a wonderful life without them and I will try my best to pay back their love.

TABLE OF CONTENTS

LIST OF TBALES

LIST OF FIGURES

LIST OF FIGURES

LIST OF FIGURES

LIST OF FIGURES

Figure   **Page**

CHAPTER 1

INTRODUCTION

1.1 Introduction of One- and Two-Photon Fluorescence

1.11 One-Photon Fluorescence

Fluorescence is the emission of photons from substances upon absorbing light or other electromagnetic radiation. The various molecular processes that occur between absorption and emission of light can be described by a Jablonski diagram.[1] A typical Jablonski diagram illustrates the singlet ground (S_0) state, as well as the first (S_1) and second (S_2) excited singlet states (Figure 1.1). With ultraviolet or visible light, a molecule is usually excited to some higher vibrational energy level of the S_1 or S_2 state. If the molecule returns to its ground state by radiative decay, this process is called fluorescence emission and the absorbing and emitting component of the molecule is often referred to as a fluorophore. Due to energy dissipation during the excited-state lifetime, the energies of emitted photons are lower than the excited photons, therefore, resulting in longer emission wavelength relative to the excitation wavelength. This difference between the absorbance and emission wavelengths is called the Stokes shift.
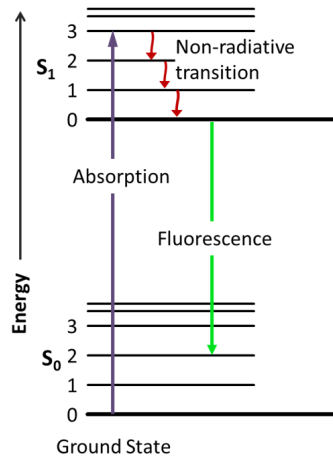
Figure 1.1 Jablonski diagram of one-photon fluorescence.
Source: J. R. Lakowicz in *Principles of Fluorescence Spectroscopy*, Springer, New York, N. Y. **1999,** pp. 1-25.

1.12 Two-Photon Fluorescence

Unlike one-photon excitation, two-photon excitation indicates that the fluorophore has reached the excited state by absorption of two photons simultaneously. As shown in Figure 1.2, the combined energy of the two-photons accesses a stable excited state of molecules and this process can lead to emission with a shorter wavelength than the excitation light, often referred to as upconverted fluorescence.[1]
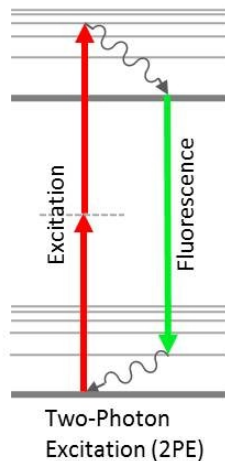
Figure 1.2 Two-photon excitation process.
Source: J. R. Lakowicz in *Principles of Fluorescence Spectroscopy*, Springer, New York, N. Y. **1999,** pp. 1-25.

1.2 Theoretical Background for One- and Two-Photon Fluorescence

1.21 Fluorescence Lifetime

The fluorescence and quantum yield are perhaps the most important characteristics of a fluorophore. The fluorescence lifetime is a measure of time a fluorophore spends in the excited state before returning to the ground state by emitting a photon. The fluorescence lifetime of a fluorophore can range from picoseconds and hundreds of nanoseconds.[2]

1.22 Fluorescence Quantum Yield

The fluorescence quantum yield is the ratio of the number of photons emitted to the number absorbed by the molecule. During the experiment, the fluorescence quantum yield is normally recorded and calculated relative to using standards, and the value is calculated according to equation (1.1):

$$\phi_{sample} = \phi_{ref} . \frac{OD_{ref} I_{sample} n_{sample}^2}{OD_{sample} I_{ref} n_{ref}^2} \qquad (1.1)$$

where Φ is quantum yield, I is integrated emission signal, OD is optical density at the excitation wavelength, and n is refractive index; the subscript 'ref' stands for reference samples, 'sample' stands for the sample being measured.[3, 4]

1.23 Fluorescence Anisotropy

Fluorescence anisotropy measures the rotational mobility of the fluorophores that are excited with polarized light. Upon excitation with polarized light., the emission from many samples is also polarized. The extent of polarization of the emission is described in terms

of the anisotropy (r).[1, 5] The intensity of the emission is measured through a polarizer. When the emission polarizer is oriented parallel ($\parallel$) to the direction of the polarized excitation the observed intensity is called $I_\parallel$. Likewise, when the polarizer is perpendicular ($\perp$) to the excitation the intensity is called $I_\perp$. These intensity values are used to calculate the anisotropy (1.2)[6]:

$$r = (I_\parallel - I_\perp) \,/\, (I_\parallel + 2I_\perp) \qquad (1.2)$$

Anisotropy measurements provide information on the size and shape of proteins or the rigidity of various molecular environments. Anisotropy measurements have been used to measure protein–protein associations,[7] fluidity of membranes,[8] and for immunoassays of numerous substances.[9]

1.3 Two-Photon Excitation Microscopy

Two-photon excitation microscopy is a fluorescence technique that uses two lower-energy photons that cooperate to cause a higher-energy electronic transition in fluorescent molecules. It is typically implemented in simple laser scanning microscopy (Figure 1.3). A laser is focused to a tight spot in the specimen plane and scanned in a raster over the sample. Fluorescence photons are generated selectively in the thin focal volume and detected by photodetectors when the laser focus overlaps with fluorescent molecules in the sample.[10] The advantage of 2-photon microscopy over confocal microscopy is that it can penetrate deeper into tissue due to absence of out-of-focus absorption, the longer excitation wavelength and less scattered light (Figure 1.4)**.**
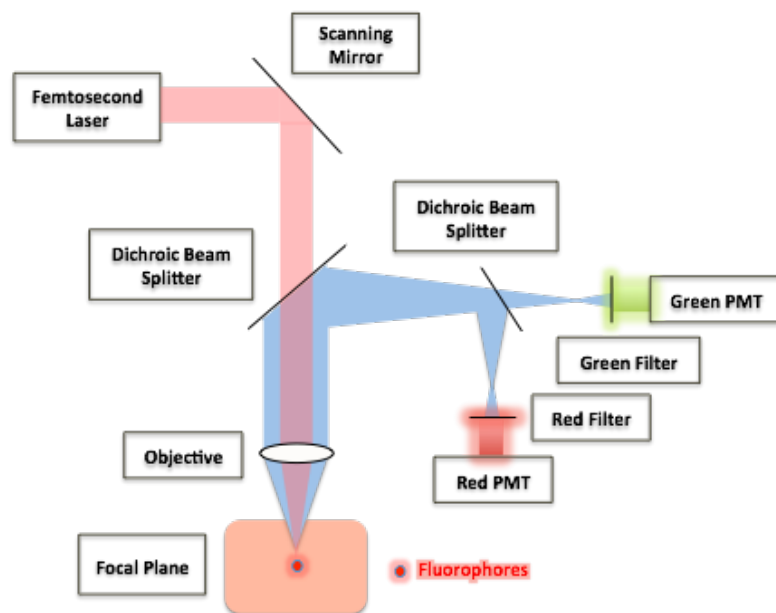
Figure 1.3 Illustration of two-photon excitation microscopy.
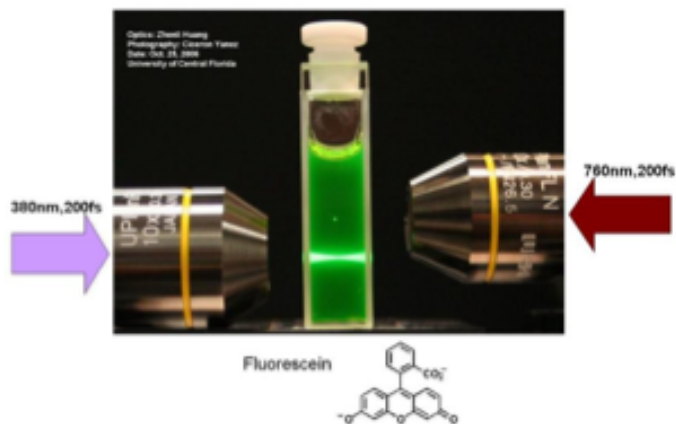
Figure 1.4 The comparation of one- and two-photon excitation.

Two-photon excitation microscopy or two-photon fluorescence microscopy (2PFM) has been widely used in many scientific fields, including solar energy conversion,[11,12] optical data storage,[13,14] fluorescence-based sensing methodologies,[15] and cancer therapy.[16,17,18] Time-dependent observation of biological specimens is challenged by light

scattering and photodamage caused by excessive excitation energy, particularly in the UV to the mid-visible spectral range.[19]

Most commercially available fluorescent probes photobleach rapidly and exhibit low two-photon absorption, hence are far from optimized for 2PFM. The combination of 2PFM with novel fluorescent probes processing high photostability, low toxicity, as well as high fluorescence quantum yields are of appreciable interest and the subject of this work.[17-20]

CHAPTER 2

SYSTEMATIC MOLECULAR DESIGN OF A SERIES OF SQUARAINE DERIVATIVES AND THEIR PROPERTIES STUDY

With the objective of developing new near-infrared fluorescent probes and understanding the effect molecular structure exerts on physical properties, a series of aniline-based squaraine dyes with different number and position of methoxy substituents adjacent to the squaraine core were synthesized and investigated. Using both computational and experimental methods, we found that the subtle changes of the number or position of the methoxy substituents influenced the twisting angle of the structure and led to significant variations in optical properties. Moreover, the methoxy substituent also affected aggregation behavior due to steric effects. The X-ray crystal structure of one of the key members of the series, SD-2a, clearly demonstrates the distortion between the four-membered squaraine core and the adjacent aniline ring due to methoxy substitution. Structure related fast relaxation processes were investigated by femtosecond pump−probe experiments and transient absorption spectra. Quantum chemical calculations and essential state models were exploited to analyze the primary experimental results. The comprehensive investigation of structure-related properties of dihydroxylaniline-based squaraine dyes, with systematic substitution of OH by OCH_3 functional groups, serves as a guide for the design of novel squaraine dyes for photonics applications.

2.1 Introduction

Fluorescent dyes that absorb near-infrared (NIR) radiation have an increasing number of applications in materials science, biomedical science, and nanotechnology.[21-26] Squaraines, as a promising class of NIR dyes, have garnered attention in organic solar cell materials,[27-30] optical storage media,[21-33] two-photon absorbing materials,[34,35] fluorescent probes,[36.37] and sensitizers for photodynamic cancer therapy.[38-40] Though significant attention has been paid to the design and synthesis of novel squaraine dyes, much less prevalent are systematic studies of structure-related photophysical properties of these promising photonic materials.[41]

Dihydroxylaniline-based squaraine derivatives with straight or branched terminal alkyl chains have been reported,[42-45] as have some relations between bulky terminal chains and intermolecular interactions and photophysical/photochemical properties.[44] In general, steric hindrance increases as the length of straight alkyl chains increases; meanwhile, branched alkyl chains such as isobutyl and 2-ethylhexyl have larger steric demands than straight-chain analogues. Chen et al. reported that both the terminal chains and the number of OH groups in the mono- or dihydroxylaniline-based squaraine dyes play important roles in determining aggregation behavior and photovoltaic performance.[45] Studies by Law showed that the electronic transitions of the squaraine dyes exhibited high sensitivity toward substitutional modifications and the surrounding solvent medium.[46] Thus, the impact of the molecular structure on intermolecular interactions as well as electronic and photophysical properties of squaraines can dramatically influence their behavior and potential applications, compelling us to further explore the fundamental structurerelated properties of this important class of materials.

The OH group at the ortho-position in dihydroxylaniline based squaraine dyes helps rigidify the squaraine core through intramolecular hydrogen bonding and increase stability.[47] We set out to study the influence of photophysical properties upon methodically replacing OH by OCH3 moieties at a given position in the squaraine structure. In this work, 2,4-bis{4-[N,N-di(2-ethylhexyl)amino]-2,6-dihydroxyphenyl}squaraine (SD-0), a derivative with four OH moieties, all ortho to the squaraine ring, was synthesized first, followed by reaction with dimethyl sulfate in the presence of potassium tert-butoxide in varying stoichiometries to prepare a series of novel methoxy containing squaraine derivatives with two and three methoxy groups (it was not possible to isolate the tetramethoxy derivative) as depicted in Figure 1. The effects of steric hindrance evoked by the presence of methoxy groups and disruption of intramolecular hydrogen bonding on the optical properties and resulting aggregation behavior of the dyes were examined experimentally and theoretically. Fast relaxation processes in the excited electronic states and two-photon absorption (2PA) spectra of the new squaraines were also investigated to further understand excited state dynamics and behavior.

2.2 Experimental Section

2.21 Crystal Structure Determination

Single-crystal X-ray diffraction data were collected at ChemMatCARS (Sector 15-ID-D) of the Advanced Photon Source, Argonne National Laboratory, USA. The crystals were mounted on a nylon loop with glycerol and cooled to 100 K with an Oxford Cryojet. The beam energy was 30 keV. Data were collected using a Bruker D8 fixed-chi diffractometer equipped with a Pilatus 3R 1 M detector. Data were processed with APEX2 suite

software.[48] The structure was solved by SHELXT[49] and refined by SHELXL.[50] The four-membered core was unstrained during refinement, while the branched alkyl chains were restrained with proper bond length. Non-hydrogen atoms were refined with anisotropic displacement parameters, and hydrogen atoms on carbons were placed in idealized positions. OLEX2[61] and COOT[62] software programs were used for modeling the disordered conformations. Crystals of SD-2a were grown using vapor diffusion with saturated DMSO solution.

2.22 Transient Absorption Pump-Probe Measurement

Femtosecond transient absorption spectra were recorded on a commercial transient absorption spectrometer Harpia (Light Conversion), built following a design described in detail previously.[63,64] In short, the pump and probe pulses are derived from an amplified Yb:KGW laser (Pharos, Light Conversion), providing 90 μJ pulses with the central wavelength of 1030 nm at a 66 kHz repetition rate. An optical parametric amplifier (Orpheus, Light Conversion) was used to obtain tunable pump pulses at 650 nm, while a white light continuum, generated in a sapphire window from the fundamental output of the laser, was used to probe absorption changes in the 450−950 nm range. A mechanical chopper (MC2000, Thorlabs) alternately blocked and unblocked the pump beam, the state of which (on or off) was monitored by a photodiode (Thorlabs DET10A/M). The squaraine dyes were dissolved in dichloromethane (DCM) at concentrations resulting in ~15−35% transmission through the cell with an optical path length of 1 mm. The transmittance spectra were recorded and binned according to the state of the chopper during each spectrum. Average pumped and dark spectra were obtained, from which the absorption change was calculated. A Berek polarization compensator (Newport 5540M) was used to

10

set the polarization of the pump beam at the magic angle (54.7°) with respect to the probe in order to avoid signals due to rotational diffusion of the sample molecules. The excitation pulse energy used in the experiments was 4.5 nJ; the probe beam diameter at the sample spot was ca. 90 μm (full width at half-maximum, fwhm); and the pump diameter was ~300 μm. The time resolution (fwhm) of the instrument response function was ~240 fs.

2.23 Two-photon Absorption (2PA) Measurements

Degenerate 2PA spectra of the new squaraines were obtained with a 1 kHz femtosecond laser system (Ti:sapphire regenerative amplifier (Legend Duo+) pumping an OPA (HETOPAS), all from Coherent, Inc.) using the open-aperture Z scan technique.[65] All measurements were performed in 1 mm quartz cells with dye concentrations ~10−3 M. The experimental Z-scan setup was calibrated with ZnSe, CdSe, and SiO2 as standards.

2.24 Synthesis of the Parent Dye SD-0

According to the previously published procedures,[64,65] the key intermediate 1 was prepared in a yield of 52% by reacting phloroglucinol with bis(2-ethylhexyl)amine. Condensation of 1 with squaric acid gave the parent dye SD-0 as dark blue viscous oil in 24% yield. Rf ≈ 0.67 (n-hexane/ethyl acetate, 9/1, v/v). ^{1}H NMR (CDCl3, 500 MHz, ppm): δ 10.96 (s, 4 H, phenol-H), 5.81 (s, 4 H), 3.32−3.28 (m, 8 H), 1.85−1.81 (m, 4 H), 1.35−1.24 (m, 32 H), 0.92−0.88 (m, 24 H). ^{13}C NMR (CDCl3, 126 MHz, ppm): δ (squaraine core) 181.36, 162.50, (anilinyl) 161.07, 158.27, 102.46, 94.46, 56.59 (−NCH2−), 38.12, 30.45, 28.50, 23.81, 23.09, 14.04, 10.63. HR-MS (m/z): [M + H]$^+$ Calculated for C48H77N2O6, 777.5776; Found, 777.5789.

2.5 General Procedure for the Synthesis of Novel Squaraine Derivatives

Reagents and general conditions for the synthesis of the squaraine dyes are presented in Figure 2.1. Compound SD-0, potassium tert-butoxide, and dry THF were placed in a round-bottom flask, which was then flushed with N2. Dimethyl sulfate in THF was added, and the solution was stirred at room temperature for 8 h. The resulting residue was concentrated, dissolved in DCM, washed with water, then dried over anhydrous $MgSO_4$. After filtering and removal of the solvent in vacuo, the crude product was purified by column chromatography with n-hexane/ethyl acetate as eluent, affording the corresponding methyl-substituted squaraine derivatives. We note that several of the desired compounds could be generated in the one-pot reaction and isolated, while their yields depended on the stoichiometry of starting material SD-0, dimethyl sulfate, and the base added to the reaction system. The overall yields of the derivatives were in the range of 60−70%, and structures of all dyes were fully confirmed using standard characterization methods.

SD-1: blue viscous oil. $R_f \approx 0.43$ (n-hexane/ethyl acetate, 9/ 1, v/v). ^1H NMR (CDCl3, 500 MHz, ppm): δ 12.66 (1 H, phenol-H), 11.95 (1 H, phenol-H), 11.65 (1 H, phenol-H), 5.84 (1 H), 5.80 (2 H), 5.70 (1 H), 3.91 (3 H, CH_3), 3.37−3.27 (8 H), 1.86−1.82 (4 H), 1.40−1.24 (32 H), 0.97−0.89 (24H). ^{13}C NMR (CDCl3, 126 MHz, ppm): δ 168.88, 163.83, 163.80, 162.92, 158.72, 156.56, 104.00, 102.14, 94.81, 94.26, 88.78, 56.68 (−NCH_2−), 56.53 (−NCH_2−), 55.45 (−OCH_3), 38.12, 30.65, 28.48, 23.78, 23.09, 14.03, 10.61. HR-MS (m/z): $[M + H]^+$ Calculated for $C_{49}H_{79}N_2O_6$, 791.5933; Found, 791.5939.

SD-2a: green solid. $Rf \approx 0.57$ (n-hexane/ethyl acetate, 4/1, v/v). ^1H NMR (CDCl3, 500 MHz, ppm): δ 13.98 (2 H, phenol-H), 5.83 (2 H), 5.67 (2 H), 3.91 (6 H, CH_3), 3.38−3.27 (8 H), 1.88−1.83 (4 H), 1.41−1.24 (32 H), 0.99−0.90 (24 H). ^{13}C NMR (CDCl3,

126 MHz, ppm): δ (squaraine core) 182.10, 171.71, (anilinyl) 165.83, 163.02, 156.88, 103.42, 94.82, 88.60, 56.64 (−NCH$_2$−), 55.45 (−OCH$_3$), 38.08, 30.64, 28.67, 23.94, 23.10, 14.04, 10.74. HR-MS (m/z): [M + H]$^+$ Calculated for C50H81N2O6, 805.6089; Found, 805.6078.

SD-2b: blue solid. R$_f$ ≈ 0.69 (n-hexane/ethyl acetate, 4/1, v/ v). ^{1}H NMR (CDCl$_3$, 500 MHz, ppm): δ 13.51 (2 H, phenol-H), 5.82 (2 H), 5.79 (2 H), 3.91 (6 H, CH$_3$), 3.40−3.27 (8 H), 1.88−1.83 (4 H), 1.40−1.24 (32 H), 0.98−0.88 (24 H). ^{13}C NMR (CDCl3, 126 MHz, ppm): δ (squaraine core) 182.84, 180.15, 165.29, (anilinyl) 163.97, 161.80, 160.50, 153.78, 107.07, 99.62, 94.28, 89.15, 56.93 (−NCH$_2$−), 56.71 (−NCH$_2$−), 55.69 (−OCH$_3$), 38.28, 37.77, 30.96, 30.41, 28.47, 23.77, 23.10, 14.04, 10.94, 10.61. HR-MS (m/z): [M + H]$^+$ Calculated for C50H81N2O6, 805.6089; Found, 805.6087. SD-3: blue solid. Rf ≈ 0.69 (n-hexane/ethyl acetate, 1/1, v/ v). 1H NMR (CDCl$_3$, 500 MHz, ppm): δ 15.73 (1 H, phenol- H), 5.83−5.80 (3 H), 5.64 (1 H), 3.93 (3 H, CH$_3$), 3.90 (6 H, CH$_3$), 3.39−3.31 (8 H), 1.87−1.83 (4 H), 1.37−1.24 (32 H), 0.94−0.90 (24 H). 13C NMR (CDCl$_3$, 126 MHz, ppm): δ (squaraine core) 188.44, 185.19, 177.21, 173.87, (anilinyl) 168.54, 164.24, 161.61, 158.98, 153.42, 106.75, 99.94, 94.91, 89.28, 88.70, 56.92 (−NCH$_2$−), 56.82 (−NCH$_2$−), 55.77 (−OCH$_3$), 55.44 (−OCH$_3$), 38.30, 37.69, 30.96, 30.91, 30.61, 28.97, 28.94, 28.64, 24.19, 24.16, 23.92, 23.11, 23.05, 14.05, 14.02, 10.93, 10.90, 10.73. HR-MS (m/z): [M + H]$^+$ Calculated for C$_{51}$H$_{83}$N$_2$O$_6$, 819.6246; Found, 819.6226.

2.3 Results and Discussion

2.31 Synthesis and Characterization

As illustrated in Figures 2.1 and 2.2, a series of methyl-substituted squaraine derivatives SD-1, SD-2a, SD-2b, and SD-3 were prepared via nucleophilic substitution reactions. SD-0 with four OH groups serve as both the parent compound and control.[66,67] The substitution of one hydroxy H provided the monomethylated derivative SD-1. Interestingly, substitution of two hydroxy H's of SD-0 produced two distinct dimethylated isomers SD-2a and SD-2b, with two methyl groups on different or the same aniline moiety, respectively. Likewise, substitution of three hydroxy H's of SD-0 generated trisubstituted squaraine SD-3. As indicated, the tetramethylated derivative SD-4 was not attained under either the same reaction conditions or an alternate route by reaction of N,N-bis(2-ethylhexyl)-3,5-dimethoxyaniline with squaric acid (cf. Figure 2.1). To this we ascribe strong steric forces evoked by the introduction of four methoxy groups ortho to the central squaraine core that would eliminate all intramolecular hydrogen bonding and impose severe intramolecular steric effects.

$R_1=CH_3$, $R_2=R_3=R_4=H$, **SD-1**;
$R_1=R_2=CH_3$, $R_3=R_4=H$, **SD-2a**;
$R_1=R_4=CH_3$, $R_2=R_3=H$, **SD-2b**;
$R_1=R_2=R_3=CH_3$, $R_4=H$, **SD-3**;
$R_1=R_2=R_3=R_4=CH_3$, **SD-4**
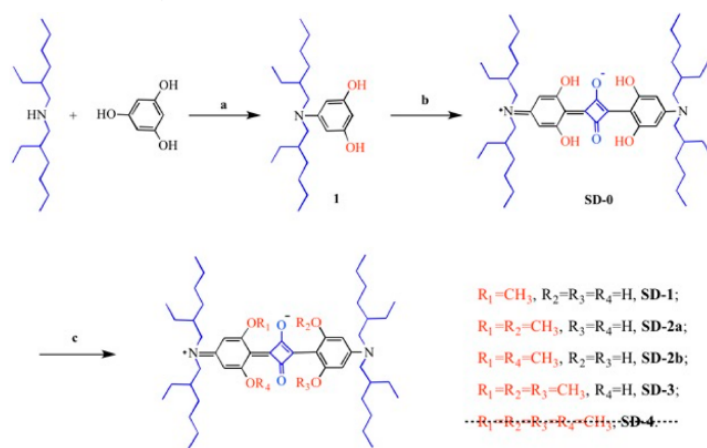
[a]Reaction conditions: (a) 1-butanol/toluene, Dean–Stark trap, reflux; (b) squaric acid, 1-butanol/toluene, Dean–Stark trap, reflux; (c) dimethyl sulfate, potassium *t*-butoxide, THF, rt.

Figure 2.1 Synthesis of the novel squaraeine dyes.
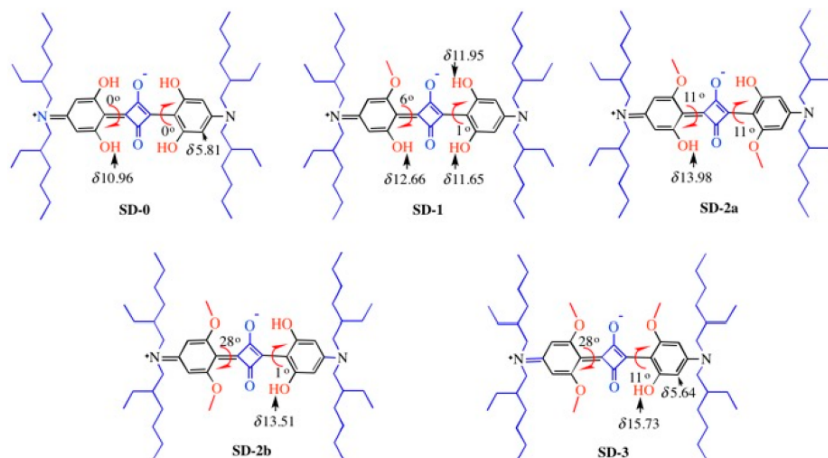
Figure 2.2 Zwitterionic structures, partial assignment of the proton NMR, and key dihedral angles of squaraine derivatives.

NMR data were helpful in confirming the structure of the dyes. As shown in Figures 2.1 and 2.3, the complete proton spectrum for each dye can be reasonably assigned. In detail, the protons of the benzene ring in SD-0 appeared as a singlet at δ 5.81 ppm, and the OH protons appeared at δ 10.96 ppm. Upon methylation, the OH proton at the ortho-position of the aniline experienced a large shift downfield compared with parent SD-0 (Δδ = 3.02 ppm for SD-2a, 2.55 ppm for SD-2b, and 4.77 ppm for SD-3). The proton signals at the ortho-position relative to N of the aniline ring show clear translocation, with one shifted upfield from 5.81 ppm in SD-0 to 5.64 ppm in SD-3. This means that the introduction of the methyl group exerts a significant influence on the effective conjugation and the intramolecular hydrogen bonding between OH and the squaryl oxygen in this series of dyes.[68,69]
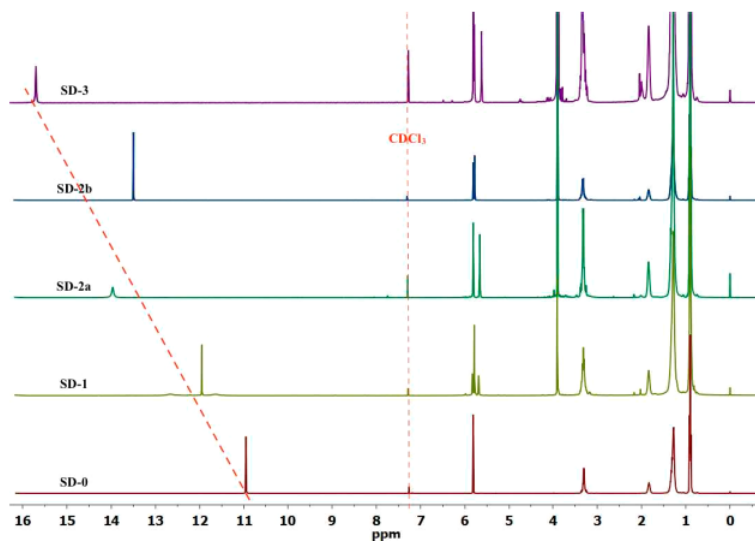
Figure 2.3 Overlay of ^{1}H NMR spectra of squaraines SD-0, SD-1, SD-2 and SD-3 in CDCl₃.

2.32 Crystal Structure of Dye SD-2a

The crystal structure was solved in the centrosymmetric triclinic space group with two half nonequivalent molecules in the asymmetry unit (Figure 2.4A). One of them is disordered in the crystal. The end branched alkyl chains are flexibly demonstrated by their large ellipsoid radius. The plane of the four-membered squaraine core is distorted by 16° away from the plane of phenol ring due to steric effects of the methoxy group on the aromatic ring (Figure 2.4B). The squaryl carbonyl is involved in hydrogen bonding with the nearby hydroxy group of the aromatic ring at a distance of 2.590 Å, which is slightly shorter compared to the value in SD-0 (2.642 Å).[64] Hydrogen bonding along with the steric hindrance imposed by the methoxy group results in distortion of the squaraine core with bond lengths of 1.475 and 1.469 Å and inner bond angles 88.4 ° and 91.6 ° (Figure 2.4C). The SD-2a molecules are compactly packed in the crystal cell with the terminal alkyl chain oriented toward the conjugated π system (Figure 2.4D).
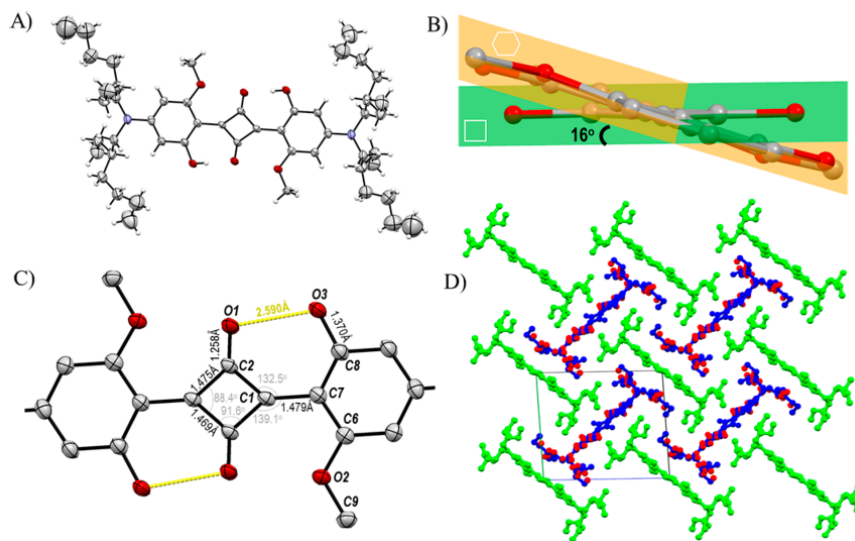
Figure 2.4 Crystal structure and packing of SD-2a. (A) Crystal structure of SD-2a is shown with ORTEP diagrams with thermal ellipsoid at the 20% level. Atom color scheme: C: gray; O, red; N, blue; H, white. (B) The crystal structure of SD-2a shows distortion of a four-carbon core plane (green) away from the plane of the phenol moiety (orange). (C) The bond lengths and angles of the four-carbon core are also labeled. The hydrogen bonds between carbonyl groups of the four-carbon core and hydroxyl groups of phenol are shown as yellow dash. (D) The crystal packing of SD-2a. The nonequivalent molecules are shown in different color including the disordered parts.

2.33 Spectral Properties

The optical properties of SD-0 and four methylated derivatives (SD-1, SD-2a, SD-2b, and SD-3) were investigated in DCM in order to evaluate the effect of the structural modification and are summarized in Table 2.1. Typical absorption and emission spectra of SD-0, SD-2a, and SD-3 are presented as examples in Figure 2.5A. As depicted, all the derivatives have sharp and intense absorption in the long wavelength region, similar to the parent dye SD-0. In particular, SD-2a has a sharp absorption peak at 651 nm and a strong fluorescence emission maximum at 668 nm as well as a characteristically small Stokes shift in DCM. A weak vibronic shoulder at 605 nm was found only in the absorption spectrum of SD-0.[65-67] The absorption maxima of SD-2b and SD-3 show hypsochromic shifts of 13 and 18 nm, respectively, relative to SD-0.
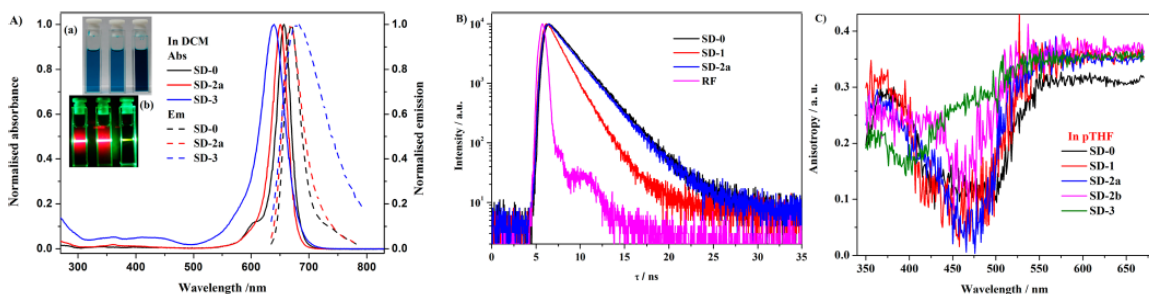
Figure 2.5 Spectra properties. (A) Normalized absorption and fluorescence spectra of SD-0, SD-2a, and SD-3 in DCM. Inset: images of these dyes in DCM under visible light (a) and laser beam (λ = 520−540 nm, from left to right: SD-0, SD-2a, and SD-3) (b). (B) Fluorescence decay curves of SD-0, SD-1, and SD-2a in DCM with instrument response function (RF). (C) Excitation anisotropy of the dyes in pTHF.

Table 2.1 Photophysical Properties of the Dyes in Different Solvents

Dyes	λ_{abs}[a] [nm]	λ_{em}[a] [nm]	ε[a] [10^5 M^{-1}·cm^{-1}]	$\Delta\lambda$[a] [nm/cm^{-1}]	FWHM[a] [nm]	τ_F[a] [ns]	$Eg_{expl.}$[b] [eV]	LUMO[c] [eV]	HOMO[c] [eV]	ΔE_{H-L}[d] [eV]	Φ_F[e]	$(\Phi_{ph}\cdot10^8)$[a]
SD-0	657	670	2.95	13/300	33	2.39	1.84	-2.53	-4.94	2.41	0.77	6.1
SD-1	652	668	2.71	16/370	33	1.49	1.85	-2.31	-4.73	2.42	0.41	1.7
SD-2a	651	668	2.82	17/390	41	2.32	1.85	-2.12	-4.52	2.40	0.72	7.8
SD-2b	644	682	1.93	38/865	63	~0.10	1.86	-2.13	-4.59	2.46	0.01	0.4
SD-3	639	690	1.16	51/1157	77	~0.10	1.87	-1.93	-4.36	2.43	0.01	4.1
SD-4	/	/	/	/	/	/	/	-1.80	-3.98	2.18	/	/

[a]Measured in DCM. [b]Optical band gap (Egexpl.) = 1240/λ onset from UV−vis spectra. [c]Calculated by B3LYP/6-31G(d). [d]ΔE_{H-L} = LUMO−HOMO. [e]Error limit ±5%.

The respective molar extinction coefficients of the squaraine series are in the range of (1.1−2.8) × 10^5 M^{-1}·cm^{-1}, the same order of magnitude as SD-0. The fluorescence spectra undergo a slight bathochromic shift and marked broadening as the number of methoxy groups increases. The fwhm values of the fluorescence emission increased from 33 nm of SD-1 to 77 nm of SD-3. Their fluorescence quantum yield, Φ_F, values follow the order of SD-0 > SD-2a > SD-1 ≫ SD-2b ≈ SD-3. Among the methylated derivatives (in DCM), SD-2a afforded a higher Φ_F value (0.72), while the Φ_F values of SD-2b and SD-3

were found to be very low (around 0.01). The suppression of Φ_F after attaching different methyl groups likely arises from intramolecular rotation of the substituent groups, which provides additional channels for nonradiative de-excitation.[35] The same order was observed for fluorescence lifetimes, which corresponded to a single exponential decay, e.g., 1.49 ns for SD- 1 and 2.32 ns for SD-2a (Figure 2.5B), while the fluorescence lifetimes of SD-2b and SD-3 were found to be very short (~0.1 ns). With respect to the optical properties, a comparison of SD- 2a and SD-2b revealed differences caused by the position of methyl substitution. The results suggest a large decrease in efficient delocalization throughout the conjugated backbone of SD-2b, a supposition further supported by computational results discussed below.

Excitation anisotropy spectra provided information regarding the nature of linear absorption bands. The excitation anisotropy spectra of the dyes in viscous polytetrahydrofuran (pTHF) are presented in Figure 2.5 C. We can see that the values of anisotropy were nearly constant in the main long-wavelength absorption band[68] and reached their maximum value r ≈ r_0 ≈ 0.37 for the modified dyes, and the value of SD-0 is around 0.31, reflecting a nearly parallel orientation of the absorption and the emission transition dipoles of new dyes in this spectral range. At higher energy, the anisotropy decreased and dips were observed near 470 nm for SD-0, SD-1, SD-2a, and SD-2b and 400 nm for SD-3, respectively, which suggests an additional electronic state with a transition dipole noncollinear with the main absorption band.[69] The photodecomposition quantum yields (Φ_{ph}) of the dyes in DCM were calculated in the range of $(0.4-7.8) \times 10^{-8}$, indicating very good photostability of the squaraine derivatives with substantial promise as probes for bioimaging.

2.34 Aggregation Studies

Squaraine dyes are known for their tendency to aggregate in different environments. Aggregate spectra are characterized by the appearance of new absorption bands and/or broadened spectra and sometimes by the quenching of the fluorescence intensity.[42-45]Figure 2.6A shows absorption spectra measured for the squaraine dyes in DMSO at the nominal concentration of $\sim 5.0 \times 10^{-6}$ M. The absorption spectrum of SD-0 shows a clear signature of aggregation: the small peak at 655 nm is clearly the monomer band, but the large peak at 557 can be safely ascribed to an H-aggregate. The solution color of SD-0 in DMSO is purple, and the dye existed mainly in its aggregated form. This is partially due to the fact that the end branch of bis(2-ethylhexane) may not efficiently prevent aggregation in poor solvents. In DMSO solution, SD-2a appeared as the typical blue color. All four derivatives showed characteristically sharp and intense absorption bands centered around 650 nm in DMSO that are indicative of the presence of mostly monomeric, i.e., nonaggregated, squaraine dyes.[66,70] The absorption spectra of SD-2a in DMSO with various concentrations are given in Figure 2.6B. SD-2a exhibited a well-defined absorption band with a maximum at 660 nm. No changes in the spectral bands were observed with increasing SD-2a concentration, thus indicating the dye's ability to remain in monomeric form even at relatively higher concentrations.
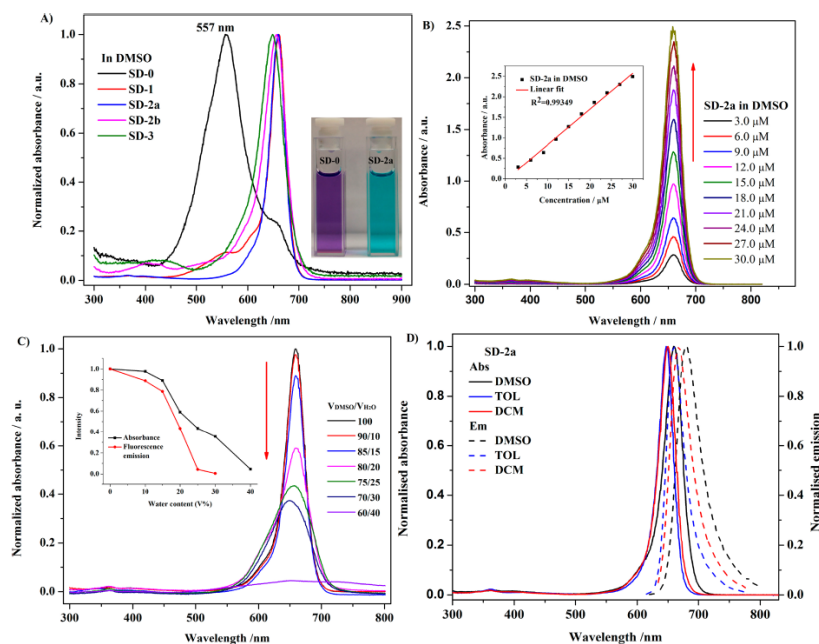
Figure 2.6 Aggregation studies. (A) Normalized absorption of SD-0 and four squaraine derivatives in DMSO. Inset: images of SD-0 and SD-2a in DMSO under visible light. (B) Absorption spectra of SD-2a in DMSO at different concentrations. Inset: plots of absorption intensity at 660 nm to the concentration of SD-2a. (C) Absorbance of SD-2a in the mixture of DMSO and water with different ratio. Inset: plots of the normalized absorbance and fluorescence intensity to the water content in the DMSO/H2O mixture (v/v). (D) Normalized absorption and fluorescence spectra of SD-2a in different solvents.

Meanwhile, the optical intensity and fluorescence emission of SD-2a at the same concentration level in the DMSO/H$_2$O mixture (Figure 2.6C) were also measured. With an increase in the water content in the mixture from 0 to 40%, SD-2a revealed no spectral broadening or aggregation-induced shoulder in the absorption spectra. Both the absorption intensity and fluorescence emission intensity decreased with increasing H$_2$O concentration, with fluorescence decreasing faster and not producing any new spectral peak. The results demonstrated that the modified squaraines appear unable to get close enough to interact with each other because of the steric effect introduced by the methoxy groups.

2.35 Solvent Effect

In an effort to gain further insight into the photophysical properties of the series of dyes, the absorption and emission behavior of the squaraines in toluene (TOL), tetrahydrofuran (THF), acetontrile (ACN), and dimethyl sulfoxide (DMSO) were conducted, and the corresponding photophysical data are summarized in Table 2.2. Typical absorption and emission spectra of SD-2a, as an example in DCM, TOL, and DMSO, are presented in Figure 2.6D. The steady-state absorption maximum and the fluorescence emission maximum and the fluorescence emission are weakly affected by the solvent. While in general a slight red-shift was observed with increasing solvent polarity, the behavior is nonmonotonic, suggesting the possibility of site-specific effects, most probably related to the presence of pH-sensitive groups in the squaraine systems. The fluorescence quantum yields and fluorescence lifetimes decreased from nonpolar to polar media. In the case of SD-2a, the results show that the fluorescence quantum yield can be observed to be relatively high in nonpolar solvents ($\Phi_F = 0.81$ in TOL) and low in polar solvents ($\Phi_F = 0.38$ in DMSO). Finally, a very interesting result comes from the analysis of the ΦF values and fluorescence lifetimes of SD-3 in different solvents. The Φ_F values decreased dramatically from 0.30 in TOL to 0.02 in THF and 0.01 in DMSO (Table 2.2). This phenomenon was confirmed by the Φ_F difference in cyclohexane (0.30) and dioxane (0.04). We can conclude that the involvement of a nonradiative channel is very sensitive to the rapid excited-state charge transfer or electronic redistribution in squaraines, and the polarity of the solvent favors the shortening of the fluorescence lifetimes by forming the solute solvent complexes.[46]

Table 2.2 Photophysical Properties of the Dyes in Different Solvents

Dyes	SD-1				SD-2a			
Solvents	TOL	THF	ACN	DMSO	TOL	THF	ACN	DMSO
λ_{abs} [nm]	647	650	650	660	646	647	648	660
λ_{em} [nm]	660	664	667	680	659	662	667	680
ε_{max} [$10^5\,M^{-1}\cdot cm^{-1}$]	2.59	2.44	2.58	1.05	2.53	2.50	2.34	2.04
$\Delta\lambda$ [nm]	13	14	17	20	13	15	19	20
Δv [cm^{-1}]	300	320	390	450	300	350	440	450
τ_F [ns]	0.75	1.05	0.73	0.81	2.26	1.92	1.38	1.64
Φ_F	0.25	0.34	0.23	0.14	0.81	0.64	0.40	0.38

Dyes	SD-2b				SD-3			
Solvents	TOL	THF	TOL	THF	TOL	THF	TOL	THF
λ_{abs} [nm]	630	636	630	636	630	636	630	636
λ_{em} [nm]	660	671	660	671	660	671	660	671
ε_{max} [$10^5\,M^{-1}\cdot cm^{-1}$]	1.53	1.73	1.53	1.73	1.53	1.73	1.53	1.73
$\Delta\lambda$ [nm]	30	35	30	35	30	35	30	35
Δv [cm^{-1}]	721	820	721	820	721	820	721	820
τ_F [ns]	0.15	0.12	0.15	0.12	0.15	0.12	0.15	0.12
Φ_F	0.01	0.01	0.01	0.01	0.01	0.01	0.01	0.01

[a]Measured in DCM. [b]Optical band gap (Egexpl.) = 1240/λ onset from UV−vis spectra. [c]Calculated by B3LYP/6 31G(d). [d]ΔEH-L = LUMO− HOMO. [e]Error limit ±5%.

2.36 Transient Absorption Spectroscopy and 2PA Spectra of Squaraine Derivatives

The nature of transient absorption processes in SD-0−SD-3 was investigated in DCM solution by femtosecond pump−probe experimental methodology.[63,64] The contour plots of the induced optical density signals, ΔD, time-resolved transient absorption spectra, where ΔD is a function of τ_D (ΔD = f(τ_D) and τ_D is the time delay between pump and probe pulses), of the new squaraine dyes were obtained under their excitation in the main absorption bands ($\lambda_{ex} \approx$ 650 nm) and presented in Figure 2.7. In general, the nature of the transient absorption spectra can be attributed to excited state absorption (ESA), saturable absorption (SA), and gain processes.[71] The first (positive) transient absorption contours at ∼500 nm (Figure 2.7B) are typical ESA bands for similar squaraine-type structures with the maxima absorption wavelengths in the spectral range 630−660 nm.[72] The second (negative)

transient absorption contours, with maximum at ~650 nm, are a combination of SA and gain signals with the dominant role of SA in the spectral range ~550−660 nm and gain processes for $\lambda > 680$ nm. Relatively narrow negative contours for SD-0 and SD-1 (Figures $2.7B_1$ and$2.7B_2$) and increased spectral width for SD-2b and SD-3 (Figures $2.7B_3$ and $2.7B_4$) were in good agreement with the corresponding steady-state spectral data in Table 2.1 and Figure 2.5A. The global fit of the experimental data (Figure 2.7A) gives several exponential components in the obtained kinetic curves $\Delta D = f(\tau_D)$. The short-wavelength ESA bands at ~500 nm arise in the first ~500 fs (Figure 2.7C) and then slowly relax to zero with characteristic times of ≈ 2.6 ns (SD-0), ≈ 2.0 ns (SD-1), ≈ 2.6 ns (SD-2a), ≈ 51 ps (SD-2b), and ≈ 46 ps (SD-3). In the spectral range of the maximum negative transient absorption signals (~650−660 nm) kinetic curves exhibit two main relaxation processes with characteristic times ~1−3 ps and ~2−3 ns (for SD-0, SD-1, SD-2a) or ~50−70 ps (for SD-2b, SD-3). The short relaxation time can be attributed to solvate relaxation processes in low viscosity dye solution.[73] The second relatively long characteristic time obviously is related to the electronic deactivation $S_1 \rightarrow S_0$. Relatively high fluorescence quantum yields ($\Phi_F \sim 0.4−0.8$) and efficient gain processes in SD-0, SD-1, and SD-2a (Figure 2.7B) suggest the potential for their super luminescence application.[71,74]
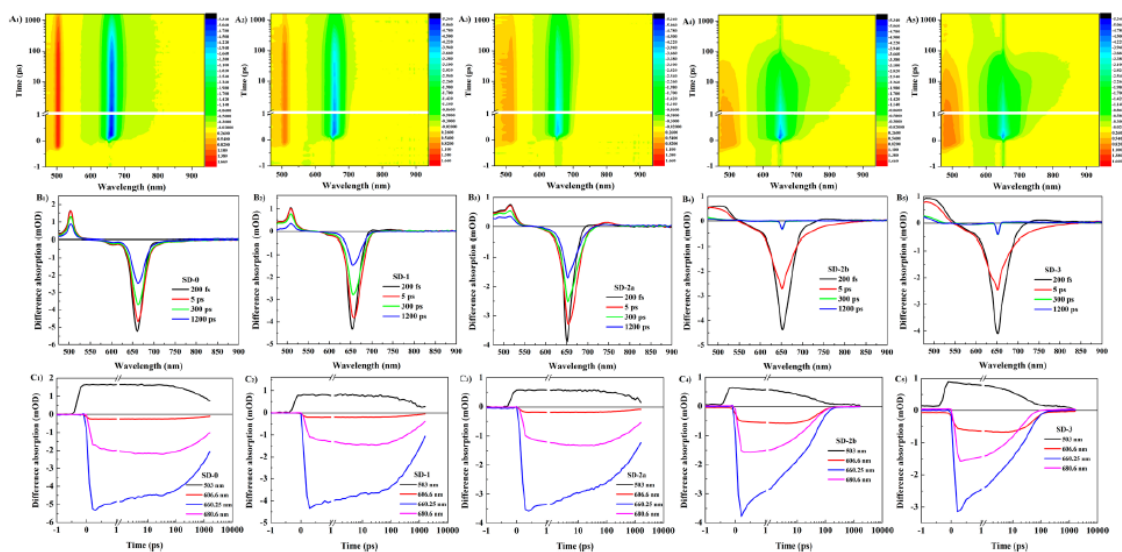
Figure 2.7 Transient absorption spectroscopy and 2PA spectra of new squaraine derivatives. (A) Contour plots of the difference absorption signals, ΔD, as a function of time delay, τ_D, for SD-0 (A_1), SD-1 (A_2), SD-2a (A_3), SD-2b (A_4), and SD-3 (A_5) in DCM ($\lambda_{ex} = 650$ nm). (B) Transient absorption spectra at selected delays, τ_D (see inserts), for SD-0 (B_1), SD-1 (B_2), SD-2a (B_3), SD-2b (B_4), and SD-3 (B_5) in DCM. (C) Transient absorption dependences ($\Delta D = f(\tau_D)$) at selected wavelengths (see insets) for SD-0 (C_1), SD-1 (C_2), SD-2a (C_3), SD-2b (C_4), and SD-3 (C_5) in DCM.

The degenerate 2PA spectra of SD-2a and SD-2b were obtained over a broad spectral range by the open-aperture Z scan technique and presented in Figure 2.8. The shape of these spectra is similar to known symmetrical squaraine derivatives with maximum linear absorption wavelengths at ~600−700 nm.[74,75] Absolute cross section values up to ~4000 GM were observed for the symmetrical squaraine SD-2a in the short wavelength two-photon allowed absorption range, in line with the typically large 2PA cross sections observed for squaraine dyes, also due to preresonance enhancement.[76] At long wavelengths, one-photon allowed 2PA efficiency decreased dramatically due to the selection rules for electronic dipole transitions. The small peak observed at ~1100 nm corresponds to a state located at 550 nm, almost 3000 cm−1 higher in energy than the one-photon state. Accordingly, it is difficult to ascribe this peak to a vibronically allowed

transition associated with the 1PA state, as it will be discussed below; we ascribe this state to an independent electronic state. The unsymmetrical compound SD-2b exhibited noticeably lower peak 2PA efficiency with a larger maximum at the vibrational shoulder of the main linear absorption band. Efficient 2PA properties of these new squaraines revealed their high potential for manifold two-photon applications.
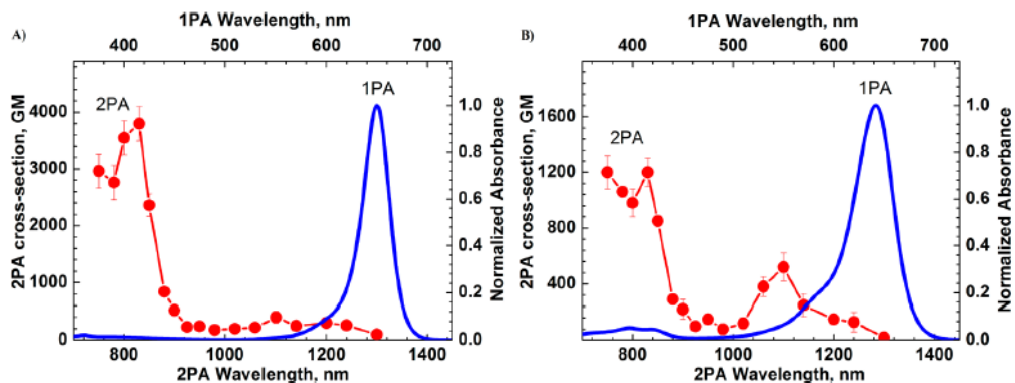
Figure 2.8 Degenerate 2PA spectra of SD-2a (A) and SD-2b (B) in DCM.

2.37 Quantum Chemical Calculations

The optimized structures, frontier molecular orbitals, and the orbital contours of the HOMO and LUMO, calculated by DFT calculations, are shown in Figure 2.9. In the central four-membered ring, the electronic distributions of HOMO orbitals are localized, while the LUMO orbitals are depleted. The energies of the dyes increase by 0.73 eV for LUMO and 0.96 eV for HOMO by changing the number of methoxyl groups, which can be related to their hypsochromic shifts in the absorption maxima. The nitrogen atoms in the dialkylamine groups become essentially conjugated with the benzene ring, mainly suggesting electron donation to the π system of the squaraines.[41] More importantly, the optimized geometry of SD-0 is almost planar, in agreement with the values reported in the literature.[43,77] Distorted dihedral angles between the methoxy-related aniline unit and the

four-membered squaraine core are summarized in Figure 2.2. The dihedral angle is calculated at ca. 11° in SD-2a and ca. 30° in SD-4. SD-2b has two different dihedral angles (ca. 28° and 1°) in order to minimize the steric repulsion, which gives limited delocalization of the excited state.[78] We can see that the larger nonplanarity in the squaraine molecule led to a greater decrease in conjugation of the whole π system, resulting in a larger change of the photophysical properties in comparison with the original dye SD-0.[79] SD-2a is considered to assume an anti-conformation on the basis of preliminary calculations. In fact, after geometry optimizations, this conformation resulted to be energetically more stable than the corresponding syn-conformation. The strong effect of steric hindrance is also evident in optimized SD-4, and the larger angle can equally explain its poor stability and the difficulty in synthesis as discussed above.[41,43]

The calculated energy gaps (ΔE_{H-L}) and the optical energy gaps ($Eg_{expl.}$) are also shown in Table 2.1. The optical band gaps of these dyes, obtained from their UV−vis spectra, show a similar increasing trend in the range of 1.84−1.87 eV. This provided further evidence for the decrease of effective conjugation in the squaraine dye from SD-1 to SD-3. The calculated energy gaps appear to be systematically higher than the optical band gaps, which is presumably because of the fact that the calculations were performed in vacuum.[80,81] According to the calculations and experimental data, the number and position of the substituent groups as well as distortion from planarity can influence the electronic delocalization and the photophysical properties of the dyes.
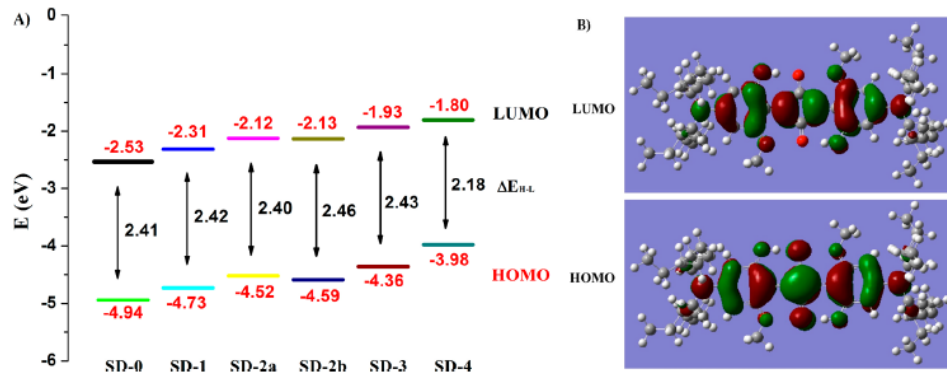
Figure 2.9 Quantum chemical calculations. (A) HOMO and LUMO energies and theoretical energy gaps of the dyes calculated at the B3LYP/6-31G(d) level. (B) Molecular orbital contours of the HOMO and LUMO for SD-2a.

2.38 Essential State Models

The minimal model for squaraine dyes describes them as D-π−A−π-D or quadrupolar dyes, where A represents the squaraic core that acts as an electron acceptor unit with respect to the lateral groups acting as electron donors.[82] The basic physics and low-energy spectroscopy of squaraine dyes is then explained in terms of three resonating structures: D-π−A−π-D ↔ D$^+$-π−A$^-$−π-D ↔ D$^-$-π−A−π-D$^+$. The three-state model accounts for the intense, narrow, and almost structureless 1PA band that characterizes squaraine spectra and the almost specular emission band with marginal Stokes shift. It also predicts a 2PA band located approximately at twice the energy of the linear absorption whose intensity is amplified by quasi-resonance effects.[82,83] Within the same model, squaraines are classified as class II quadrupolar dyes, a family of dyes that are not prone to symmetry breaking, that instead affects the lowest excited state of class I quadrupolar dyes and the ground state of class III dyes. The model was also extended to discuss asymmetric squaraines, explaining their anomalous solvatochromism.[84] However, there are a few features of the squaraine's spectra that cannot be accounted for in the three-state model.

The most obvious deviation from the predictions of the three-state model is the anisotropy dip observed in the spectral region comprised between the linear absorption band and the 2PA band,[85] pointing to the presence of an intermediate state with a polarization perpendicular to the main molecular axis. Dips in fluorescence anisotropy were also observed for cyanine dyes, usually located in the close proximity of the 2PA state.[85] The flexible and definitely nonperfectly linear structure of cyanine dyes allows ascribing these dips to the 2PA states that, for slightly bent cyanines, is expected to be orthogonal to the main absorption band, polarized along the main molecular axis. This explanation does not apply to squaraine dyes, which are characterized by a rigid and symmetric structure. The only possibility to account for states polarized perpendicularly to the main molecular axis then requires one to account for the inner degrees of freedom of the squaric ring, observing that actually each squaric core provides two acceptor sites corresponding to the two oxygen atoms. Accordingly, a squaraine dye can be described as a D(A)$_2$D, whose main resonating structures are schematically shown in Figure 2.10A.

The relevant Hamiltonian, accounting for the electron hopping among D and A sites (τ-terms), as well as for the charge resonance along the x direction (β term), reads:

$$H_{el} = \begin{matrix} 0 & -\tau_{1u} & -\tau_{1d} & -\tau_{2u} & -\tau_{2d} \\ -\tau_{1u} & 2z_{1u} & -\beta & 0 & 0 \\ -\tau_{1d} & -\beta & 2z_{1d} & 0 & 0 \\ -\tau_{2u} & 0 & 0 & 2z_{2u} & -\beta \\ -\tau_{2d} & 0 & 0 & -\beta & 2z_{2d} \end{matrix} \qquad (2.1)$$

where, to account for the most general case, we have assigned a different diagonal energy to the four zwitterionic states (the energy of the $|N\rangle$ state is set to zero) and a different hopping term for each state.
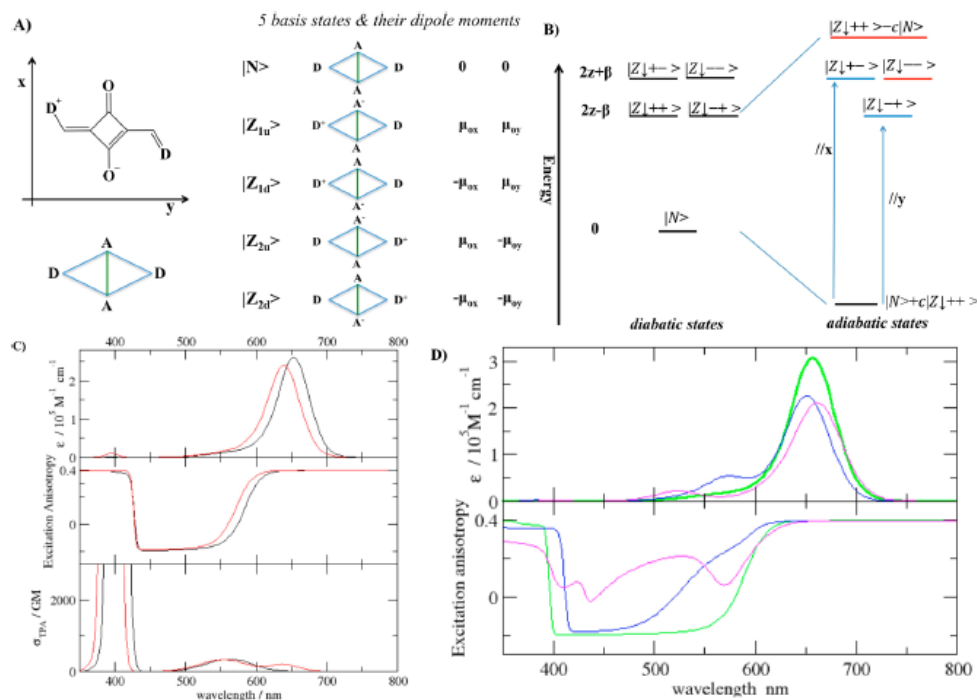
Figure 2.10 Essential structure models. (A) Structure of a squaraine and its schematic representation. The 5 basis states and their dipole moment along x and y (all off-diagonal dipole moments are neglected). (B) The case of a symmetric squaraine. On the left the basis (adiabatic) states with corresponding energies; on the right the corresponding eigenstates (the adiabatic state). Blue and red colors refer to adiabatic states. (C) Calculated spectra for SD-2a and SD-2b dyes are reported as black and red lines, respectively. Top panel: linear absorption (continuous lines) and fluorescence spectra (dashed lines, arbitrary units). Middle panel: fluorescence anisotropy spectra (calculated for emission at 670 nm). Bottom panel: 2PA spectra. (D) Calculated spectra for SD family. Top panel: absorbance (continuous lines) and fluorescence spectra (dashed lines, arbitrary units). Bottom panel: fluorescence anisotropy calculated for emission at 670 nm. Black, red, green, blue, and magenta lines refer to SD-2a, SD-2b, SD-0, SD-1, and SD-3, respectively.

It is instructive to start the analysis with symmetric squaraines, like SD-0 and SD-2a. In this case the four zwitterionic states are degenerate, and we set $z = z_{1u} + z_{1d} + z_{2u} + z_{2d}$ and $\tau = \tau_{1u} + \tau_{1d} + \tau_{2u} + \tau_{2d}$. We exploit the symmetry of the system and in particular the two C2 axes along the directions x and y to define the symmetrized basis states

$$|N\rangle \tag{2.2}$$

$$|Z_{++}\rangle = \frac{1}{2}(|Z_{1u}\rangle + |Z_{1d}\rangle + |Z_{2u}\rangle + |Z_{2d}\rangle)$$

$$|Z_{+-}\rangle = \frac{1}{2}(|Z_{1u}\rangle - |Z_{1d}\rangle + |Z_{2u}\rangle - |Z_{2d}\rangle)$$

$$|Z_{-+}\rangle = \frac{1}{2}(|Z_{1u}\rangle + |Z_{1d}\rangle - |Z_{2u}\rangle - |Z_{2d}\rangle)$$

$$|Z_{--}\rangle = \frac{1}{2}(|Z_{1u}\rangle - |Z_{1d}\rangle - |Z_{2u}\rangle + |Z_{2d}\rangle)$$

where the first and second subscripts in the symmetrized functions refer to the parity with respect to the y and x-axis, respectively. As illustrated in Figure 2.10B, $|N\rangle$ and the totally-symmetric state Z_{++} mix to give the ground state |G> and a totally-symmetric excited state |E>, which is forbidden in 1PA but 2PA allowed. The Z_{-+} state stays unmixed at energy $2z$-β, and corresponds to a 1PA allowed with polarization along the long molecular axis (2PA forbidden) state. Finally, the two states Z_{+-} and Z_{--} stay unmixed at energy $2z$+β and are allowed in 1PA (x-polarization) and 2PA, respectively. Since the molecule is very elongated, we expect that $\mu_x < \mu_y$ or, in other terms, we expect that optical spectra are mainly governed by transitions along the main molecular axis. As long as we are interested in the main spectral features, a three-state model accounting for N, Z_{++} and Z_{+-} states is enough and easily maps into the three-state model originally proposed and successfully developed for squaraine-dyes.[77]

In a more detailed analysis, the five-state model immediately suggests the presence of a 1PA state polarized perpendicularly to the main molecular axis located between the 1PA, then explaining the observation of dips in the fluorescence anisotropy spectra in the region between the main 1PA and 2PA band, due to the Z_{-+} state. Indeed the model predicts

the presence of a weak 2PA state, Z_{--}, degenerate with the Z_{-+} state, responsible for the dip in the fluorescence anisotropy. We ascribe to this state the small 2PA peak to the red of the main 1PA band (at $\sim$550 and 560 nm for SD-2a and SD-2b, respectively, see Figure 2.5C). Of course this degeneracy is maintained only in the simple model, and a splitting between the two states is expected due to the interactions with other states not accounted for in this simplified picture.

In order to actually compare with experimental spectra and specifically to address line shapes, we introduce the coupling between electronic degrees of freedom and molecular vibrations. Following a similar strategy as with the three-state model,[82] we introduce two effective vibrations that account for the different geometry on the left and right molecular arm when charge transfer occurs on the specific arm. The Hamiltonian reads

$$H_{mol} = H_{el} - \sqrt{\varepsilon_v}\,\omega_v Q_1 (|Z_{1u}\rangle \langle Z_{1u}| + \ |Z_{1d}\rangle\langle Z_{1d}|) \tag{2.3}$$

$$-\sqrt{\varepsilon_v}\,\omega_v Q_2 (|Z_{2u}\rangle \langle Z_{2u}| + \ |Z_{2d}\rangle\langle Z_{2d}|) +$$

$$\frac{1}{2}[\omega_v^2(Q_1^2 + Q_2^2) + P_1^2 + P_2^2]$$

where Q1 and Q2 are the two effective molecular coordinates associated with the two molecular arms; P1 and P2 are the conjugated momenta; and ω_v and ε_v are the vibrational frequencies and relaxation energy, assumed for simplicity equal for the two arms, even in asymmetric molecules. Finally, to reproduce the inhomogeneous broadening due to polar solvation, we introduce the coupling with the solvent in terms of the reaction field, F, as follows

$$H = H_{mol} - \vec{F} \cdot \vec{\mu} + \frac{F^2}{4\varepsilon_{or}} \qquad (2.4)$$

where ε_{or} is the solvent relaxation energy that increases with solvent polarity.

Linear absorption spectra of SD-2a and SD-2b are well reproduced, with a blue shift and a slight decrease of intensity when going from the symmetric SD-2a to the asymmetric SD- 2b dye. 2PA spectra reproduce fairly accurately the experimental data, with a band at ~560 nm ascribed to the Z— state and a secondary band at ~650 nm related to a vibronically allowed contribution from the 1PA state. As for the high frequency region, we reproduce the main 2PA band, which, due to preresonant enhancement, has large 2PA intensity. However, experimental spectra show an additional structure on the shoulder of the 2PA band. This structure points to the presence of additional states, not included in our model. Additional data, and specifically excited-state absorption spectra, would be needed to precisely parametrize the relevant states, as was done to explain similar structures in the 2PA band of cyanine dyes.[86] The main success of our 5-state model concerns the inclusion of a state with polarization perpendicular to the main molecular axis, then explaining the puzzling observation of a dip in the fluorescence anisotropy spectra of squaraine dyes. In cyanine dyes a dip in anisotropy is always observed at frequencies corresponding to the main 2PA band and can be therefore ascribed to the slightly bent quadrupolar structure of the cyanine skeleton.[85] However, in squaraines, the dip is located somewhere between the main 1PA and 2PA bands, and in view of the rigid and strictly linear molecular structure of squaraine dyes, it calls for a different origin. Our results suggest it can be ascribed to the presence of a charge resonance across the squaraine core. Indeed, the dip we calculate is

red-shifted with respect to the experiment, and it is too wide. Both features could be improved, accounting for additional states, as already discussed with reference to 2PA spectra. Indeed, it is very clear that, while the proposed 5-state model is an improvement over the basic 3-state model for squaraines, additional states are required to address 2PA spectra, as well as to remove the degeneracy of the Z_{-+} and Z_{--} states moving the Z_{-+} state, responsible for the dip at higher energy with respect to the Z_{--} state.

Table 2.3 Primary Model Parameters for the SD Dyes

	SD-2a	*SD-2b*	*SD-0*	*SD-1*	*SD-3*
$z_{1u}=z_{2u}$	0.48	0.48	0.32	0.48	0.68
$z_{1d}=z_{2d}$				0.32	0.48
$\tau_{1u}=\tau_{1d}$	0.74	0.83	0.83	0.74	0.68
$\tau_{2u}=\tau_{2d}$		0.68			0.74

We can now transfer the information to build the model for other dyes: for SD-0, we take the same τ as for the flat arm of SD-2b but decrease 2z to account for the decreased energy of zwitterionic states related to the stronger electron-accepting character of the squaraic oxygen when involved in two hydrogen bonds, with respect to a single hydrogen bond, as for SD-2a and SD-2b dyes. Along similar lines we define the model parameters for SD-1 and SD-3, as listed in Table 2.3. Calculated spectra are shown in Figure 2.10D and compare favorably with experimental results, suggesting that the proposed model captures the main physics of this family of squaraine dyes.

2.4 Conclusion

In summary, we prepared and characterized a series of novel squaraine dyes to serve as a basis to understand molecular design and photophysical properties in an important class of organic photonic materials. These dyes show favorable absorption and emission suitable for potential NIR optical applications such as imaging and photovoltaics. The numbers and positions of methyl substituents affect the LUMO and HOMO energy levels of the related squaraine dyes in discrete manners. Meanwhile, the substituents also impact aggregation behavior in DMSO/H2O solutions. For example, SD-2a was not prone to aggregation, a process that plagues many similar molecules in polar media, and maintained high fluorescence quantum yield. On the other hand, the low quantum yields and fluorescence lifetimes of SD-2b and SD-3 revealed the pronounced effect of rather subtle changes in structure, i.e., arrangement and number of methyl substituents, on the optical properties of this series of squaraine dyes. Comprehensive photophysical studies were complemented with theoretical computations and analysis. We found that there was reasonable qualitative agreement between experimental and calculated results using a five-state model. Transient absorption spectral investigations elucidated fast temporal processes, such as excited state absorption, saturable absorption, and gain that were dependent on the number and position of methyl substitution. Additionally, two of the squaraine dyes exhibited large two-photon absorption. This systematic study helps to clarify the parameters by which squaraine dyes, especially dihydroxylaniline-based squaraine dyes, may be fine-tuned for particular purposes and provides a better understanding of the relationship between structural and optical properties that may be valuable in developing new or improved near-IR absorbing chromophores for solar cells and biological imaging.

CHAPTER 3

FLUORENYL-LOADED QUATSOME NANOSTRUCTURED FLUORESCENT PROBES

Delivery of hydrophobic materials in biological systems, for example, contrast agents or drugs, is an obdurate challenge, severely restricting the use of materials with otherwise advantageous properties. The synthesis and characterization of a highly stable and water-soluble nanovesicle, referred to as a quatsome (QS, vesicle prepared from cholesterol and amphiphilic quaternary amines), that allowed the nanostructuration of a nonwater soluble fluorene-based probe are reported. Photophysical properties of fluorenyl−quatsome nanovesicles were investigated via ultraviolet−visible absorption and fluorescence spectroscopy in various solvents. Colloidal stability and morphology of the nanostructured fluorescent probes were studied via cryogenic transmission electronic microscopy, revealing a "patchy" quatsome vascular morphology. As an example of the utility of these fluorescent nanoprobes, examination of cellular distribution was evaluated in HCT 116 (an epithelial colorectal carcinoma cell line) and COS-7 (an African green monkey kidney cell line) cell lines, demonstrating the selective localization of C-QS and M-QS vesicles in lysosomes with high Pearson's colocalization coefficient, where C-QS and M-QS refer to quatsomes prepared with hexadecyltrimethylammonium bromide or tetradecyldimethylbenzylammonium chloride, respectively. Further experiments demonstrated their use in time-dependent lysosomal tracking.

3.1 Introduction

The development of new organic molecular probes with excellent photophysical properties and high fluorescence quantum yields is of considerable interest to many research areas including one- and two-photon fluorescence microscopy, fluorescence-based sensing methodologies, and cancer therapy. [87-95] However, the hydrophobicity and poor availability in aqueous media of a preponderance of organic fluorescent molecules often severely limit their utility in biological applications, instigating a number of approaches to overcome this challenge.[88,97,98] The chemical modification of nonwatery soluble fluorene derivatives, via the addition of carboxylic[87] or salicylic acid moieties,[98] improved their solubility in biological media, overcoming in part this drawback. Alternative strategies consist of dispersing the hydrophobic probes in water as nanoparticles (NPs), for example, or by encapsulation in micelles,[99] conjugation to polymers, or incorporation in hydrophilic nanostructures.[100,101] Here, we present a new strategy to disperse in aqueous media a hydrophobic fluorene derivative. This strategy consists in the nanostructuration of the dye in a class of small unilamellar vesicles, referred to as a quatsome (QS), in which the bilayer membrane is composed of a quaternary ammonium surfactant and a sterol.[102] Quatsomes are generally very stable, and they have been recently studied and developed as a multifunctional carrier of bioactive molecules.[103]

Lysosomes are terminal degradative compartments of mammalian cells that play significant roles in cellular metabolism, endocytosis, and the synthesis/assembly of hydrolases involved in macromolecule digestion.[104,105] Dysfunction of lysosomes result in severe problems, including inflammation, cancer, and specific lysosomal storage disease, among others.[106-111] Therefore, efforts have been devoted to design and synthesize effective

fluorescent probes for the study of lysosome trafficking in cancer invasion and metastasis in recent years.[112,113] In this work, a hydrophobic fluorene derivative, DiC18 (Figure 3.1), possessing desirable photophysical properties, was designed and synthesized. Dye-loaded QSs were prepared by processing the dye along with the surfactant, cetyltrimethylammonium bromide (CTAB) or tetradecyldimethylbenzylammonium chloride (MKC), and cholesterol via a compressed CO_2 methodology named depressurization of an expanded liquid organic solution-suspension (DELOS-SUSP),[114] which leads to the formation in a single step of a highly homogeneous dispersion of functionalized quatsomes (<100 nm) in an aqueous environment. DiC18-loaded quatsomes exhibited, in both cases, advantageous photophysical characteristics and high selectivity for the lysosomes of HCT 116 and COS-7 cells, suggesting their potential as probes for short- and long-term lysosomal labeling and tracking.

3.2 Results and Discussion

3.21 Synthetic Strategy

The synthesis of target compound **DiC18** (Figure 3.1) began with 2-bromo-9H-fluorene, which was used to prepare 2-bromo-7-iodo-9H-fluorene (1) according to a literature procedure.[115] Fluorene 2 was obtained from substitution of the 9-position benzylic hydrogens of 2-bromo-7- iodo-9H-fluorene with bromoethane.[116] The Stille coupling reaction was performed between 2 and 2-(tri-n-butylstannyl)- benzothiazole with Pd(PPh$_3$)$_4$, as a catalyst, to prepare 3. Benzothiazolylfluorene 3 was reacted with N, N-di-n-octadecylamine via an Ullmann coupling reaction to produce the final product, **DiC18**,

as a yellow oil, which is nonsoluble in water but highly soluble in organic solvents of different polarities.
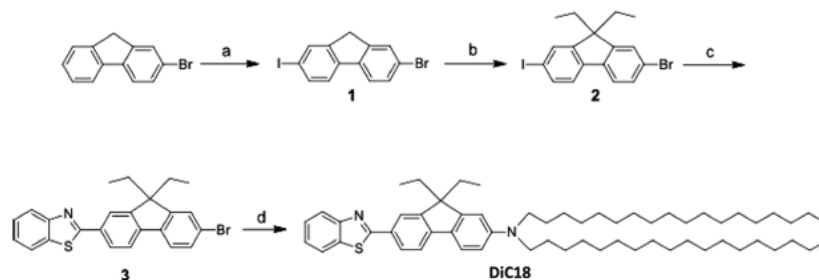
*Reagents and conditions: (a) I$_2$, KIO$_3$, HOAc, H$_2$SO$_4$, H$_2$O, 100 °C, 2 h, 80%; (b) bromoethane, KI, KOH, dimethyl sulfoxide (DMSO), room temperature, 12 h, 73%; (c) 2-(tri-n-butylstannyl)benzothiazole, Pd(PPh$_3$)$_4$, toluene (TOL), reflux, 8 h, 43%; (d) dioctadecylamine, Pd(OAc)$_2$, (t-Bu)$_3$P, t-BuONa, toluene, reflux, 16 h, 84%.

Figure 3.1 Synthetic route for preparation of **DiC18.**

3.22 Preparation of DiC18-Loaded Quatsomes

DiC18-loaded quatsomes were prepared by the CO$_2$-based method, DELOS-SUSP. First, cholesterol and **DiC18** were dissolved in EtOH and then added to a high-pressure vessel, previously heated at T_w = 308 K. Afterward, CO$_2$ was added until reaching the working pressure (P_w = 10 MPa), to obtain a CO$_2$-expanded solution of the compounds. In the last stage, the **DiC18**-loaded quatsomes were formed by depressurizing the CO$_2$-expanded solution over an aqueous solution of the surfactant (CTAB or MKC). The obtained samples were then purified by diafiltration to remove the EtOH and excess surfactant. This procedure enabled the preparation of aqueous suspensions of quatsomes based on cholesterol and CTAB, as the surfactant, with **DiC18** loadings (moles$_{DiC18}$/(moles$_{surfactant}$ + moles$_{cholesterol}$)) of 0.9×10^{-3}, 7.0×10^{-3}, and 1.3×10^{-2} for samples **C-QS-1, -2**, and **-3**, respectively. The same procedure was followed with another quaternary ammonium surfactant, MKC, which should be more suitable for parenteral drug delivery than CTAB, as it is more biocompatible obtaining dyeloaded QSs with **DiC18** loadings of 0.5×10^{-3}, 4.8×10^{-3}, and 9.7×10^{-3} for samples **M-QS-1, -2**, and **-3**, respectively.

3.23 Colloidal Stability and Morphology of DiC18-Loaded Quatsomes

Figure 3.2 shows cryogenic transmission electronic microscopy (CryoTEM) micrographs of samples **C-QS-1, -2**, and **-3** 1 week after their preparation, which appeared mostly of round-shaped nanovesicles with average hydrodynamic diameters of 70, 58, and 60 nm, as measured by dynamic light scattering (DLS) (see Table 3.1), respectively. The zeta potential of the three samples was higher than 70 mV, and average sizes were maintained over 2 months, supporting the very high colloidal stability of such systems (Table 3.1). No changes were detected in the morphology of the samples, as shown in the case of **C-QS-3** comparing 1 week versus 1 month (Figure 3.2, right). Similarly, to **C-QS, M-QS-1, -2**, and **-3** samples also possessed good colloidal stabilities.

CryoTEM images illustrate that DiC18-loaded quatsomes constituted a mix of different nanostructures. Interestingly, along with small quatsomes, the presence of some vesicles with a "patch" was detected (in all of the cases only one patch per vesicle was detected). The patches (indicated with a red arrow in Figure 3.2) can be recognized due to the higher contrast to electrons in the cryoTEM images. This new structure, named patchy-quatsomes (patchy-QSs), has not been reported in previously studied quatsomes.[102,103,114] The presence of this particular architecture is attributed to the aggregation on the surfaces of QSs of the nonwater soluble, nonamphiphilic **DiC18** molecules, favored by the multiple van der Waals interactions among their alkyl chains and the CH−p interactions with the aromatic fluorene cores, minimizing the direct contact of most of the **DiC18** molecules with the aqueous media. It is hard at this time to speculate on the exact composition/structure of these patches because they can be formed only by **DiC18** or a combination of **DiC18** and surfactant or cholesterol molecules that could stick to the QS

surfaces providing isolation from water molecules. Nevertheless, a point worth mentioning of such new structures is the fact that the presence of patches is advantageous for optical applications because they enable larger dye concentrations in aqueous suspensions without quenching or compromising too much their fluorescence properties (vide infra).
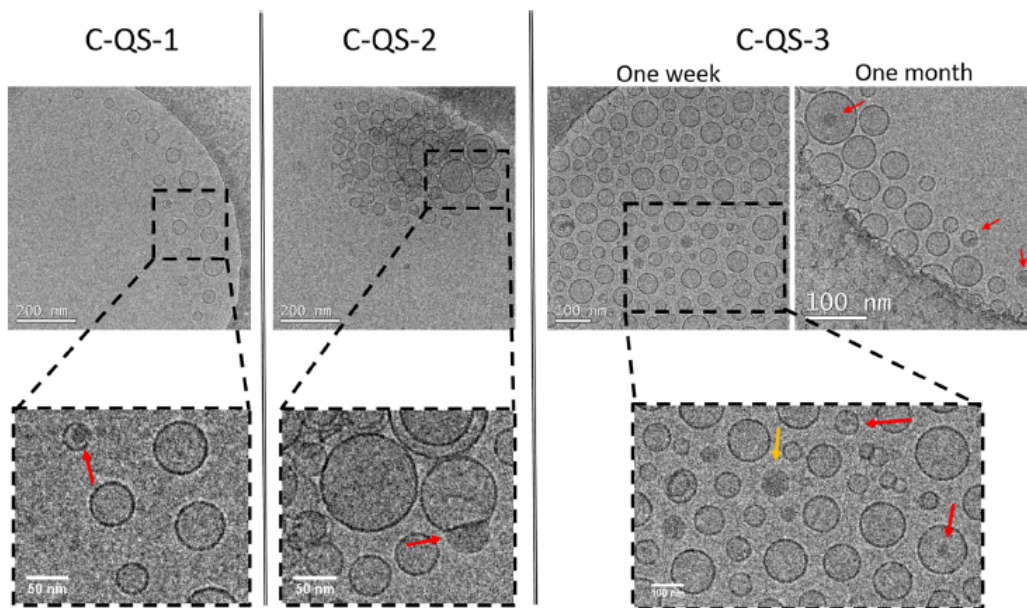
Figure 3.2 CryoTEM micrographs of **DiC18**-loaded quatsomes at increasing loading of **DiC18**: (left) **C-QS-1**; (middle) **C-QS-2**; (right) **C-QS-3** 1 week and 1 month after the preparation. Enlargements of the images are shown in the bottom part of the picture. The red arrows indicate patchyquatsomes, whereas the blue ones indicate other supramolecular organization of **DiC18**.

Table 3.1 Average Hydrodynamic Diameters of **DiC18**-Loaded Quatsomes and **DiC18** NPs

Sample	Average size one week (nm)[a]	Average size two months (nm)[b]	zeta-potential (mV)
C-QS-1	70 ± 38	73± 35	86 ± 20
C-QS-2	58 ± 30	55 ± 28	78 ± 27
C-QS-3	60 ± 32	60 ± 30	75 ± 18
M-QS-1	93 ± 48	103 ± 52	86 ± 23
M-QS-2	87 ± 49	94 ± 50	94 ± 18
M-QS-3	75 ± 37	81 ± 41	85 ± 18
DiC18 NPs	101 ± 40	184± 57	-1 ± 21

[a] Loading = $moles_{DiC18}/ (moles_{surfactant} + moles_{cholesterol})$

Along with QSs and patchy-QSs, other sparse nonvesicular structures were detected, indicated by the blue arrow in Figure 3.1 (bottom right). These structures, never detected in the case of plain QSs made with cholesterol and CTAB, are ascribed to supramolecular assemblies of DiC18 but were completely isolated and not bound to the vesicles, in contrast to that observed for patchy-QSs. **DiC18**-loaded QSs made with MKC/cholesterol showed similar structures.

3.24 Photophyscial Properties

Photophysical properties of **DiC18** were investigated in solvents with different polarities including DMSO, acetonitrile (ACN), toluene (TOL), dichloromethane (DCM), cyclohexane (CHX), and hexane (HEX). The linear absorption, emission spectra, and photophysical properties of DiC18 are shown in Figure 3.3 and summarized in Table 3.2. The absorption spectra for DiC18 displayed maximum intensity in the range of 387−411 nm, with only nominal variation as a function of solvent polarities. In comparison,

fluorescence emission of this asymmetrical (D−π−A) compound results from excitation in the main absorption band, exhibiting a bathochromic shift with strong solvent polarity dependencies, where D and A refer to electron-donor and electron-acceptor moieties, respectively, joined by a π- conjugated structure. **DiC18** emission exhibited a well-resolved vibrational structure with a maximum at 418 nm in a nonpolar solvent (hexane) and was replaced by a broader, structureless peak with the maximum shifted to 541 nm in a polar solvent (DMSO). The solvatochromic behavior of DiC18 is consistent with some other fluorene derivatives that are sensitive to the environmental polarity.[98,117,119] The compound exhibited excellent quantum yield in different solvents (all close to 1), indicating that it is a promising candidate for further chemical and biological applications.
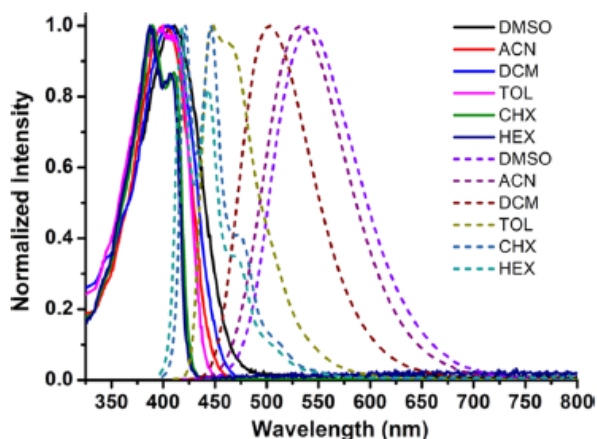
Figure 3.3 Normalized absorption (solid lines) and emission spectra (dashed lines) of DiC18 in DMSO, ACN, DCM, TOL, CHX, and HEX.

Table 3.2 Photophysical Properties for Fluorene **DiC18**

	HEX	CHX	TOL	DCM	ACN	DMSO
$\lambda_{ab}{}^{a}$ [nm]	387, 406	389, 410	400	404	401	411
$\lambda_{em}{}^{a}$ [nm]	418, 444	422, 446	447	503	532	541
$\Delta\lambda^{b}$ [nm]	31	33	47	99	131	130
$\varepsilon_{max}{}^{c}$ [10^3 M^{-1}cm^{-1}]	52	52	46	40	44	38
$\Phi_f{}^{d}$	0.92	1.00	1.00	1.00	1.00	1.00
T^{e}[ns]	1.33	1.35	1.44	2.10	2.39	2.44
$P(\varepsilon)^{f}$	0.229	0.338	0.408	0.798	0.924	0.938

[a]Absorption and emission maxima ±1 nm; [b]Stokes shift ±2 nm; [c]molar absorptivity, [d]fluorescence quantum yield ±10%; [d]fluorescence lifetimes ±5%; [e]polarity factor calculated as $P(\varepsilon) = (\varepsilon-1)/(\varepsilon+2)$, where ε is the dielectric constant.

The photophysical properties of **C-QS-1**, **-2**, and **-3** and **MQS-1**, **-2**, and **-3** are summarized in Table 3.3. The steady-state absorbance, excitation, emission, and excitation anisotropy of **C-QS-1**, **-2**, and **-3** are presented in Figure 3.4 As a consequence of their nanometric size distribution, quatsomes scatter light in the ultraviolet−visible (UV−vis) range. Especially at low **DiC18** loading (**C-QS-1**, Figure 3.4a), for which the absorption to scattering ratio is low, the absorption spectrum may be misinterpreted. The absorption spectra of the other two samples (**C-QS-2** and **-3**) are shown as originally acquired, without any mathematical treatment. The slight positive solvatochromism in absorption (from 391

to 394 nm for **CQS- 1** to **-3**) and emission (from 452 to 461 nm for **C-QS-1** to **-3**), as a function of increasing the **DiC18** loading in the QSs, suggests a change in the polarity around the fluorophore.
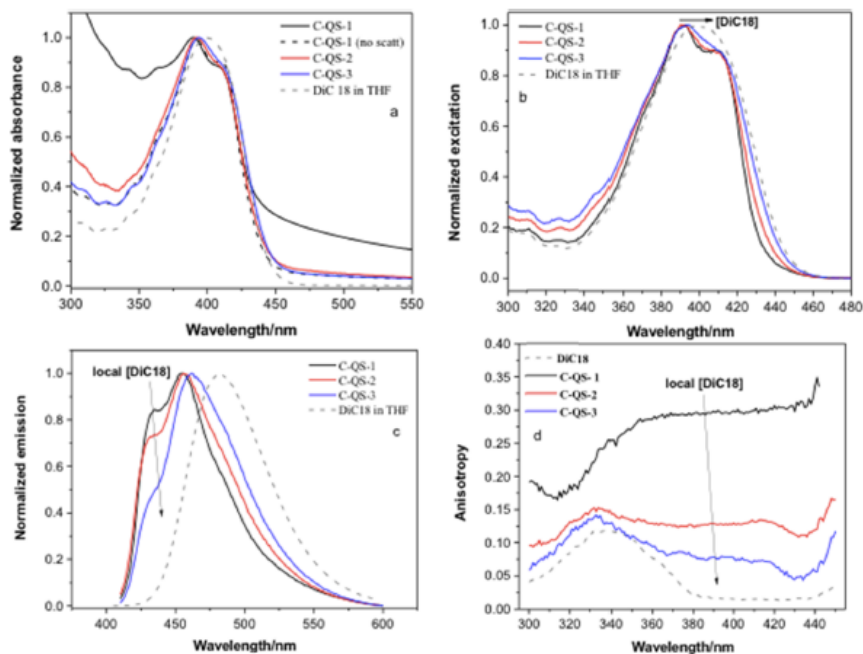
Figure 3.4 Normalized (a) absorption; (b) excitation; and (c) emission spectra of **DiC18** in THF, **C-QS-1, -2**, and **-3** in Milli-Q water. (d) Excitation anisotropy of **DiC18** and **C-QS-1, -2,** and **-3** in glycerol.

Table 3.3 Photophysical Properties of C-QS and M-QS Nanovesicles

	$\lambda_{ab}{}^a$ [nm]	$\lambda_{em}{}^a$ [nm]	$\Delta\lambda^b$ [nm]	$\Phi_f{}^c$	τ^d [ns]
DiC 18 in THF	400	482	82	0.85	1.80
C-QS-1	392	431,452	60	0.46	2.45
C-QS-2	394	455	61	0.37	2.30
C-QS-3	394	461	67	0.21	0.73 (46.48%) 3.05 (53.52%)
M-QS-1	394	430,453	59	0.40	2.28
M-QS-2	395	459	64	0.33	2.06
M-QS-3	395	468	73	0.25	0.87 (57.60%) 3.35 (42.40%)
DiC18 NPs	395	472	77	0.1	-

[a] Absorption and emission maxima ±1nm; [b] Stokes shift ±2 nm; [c] Fluorescence quantum yield ±10%; [d] fluorescence lifetimes ±5%.

However, normalized excitation spectra of **C-QS-1**, **-2**, and **-3** and **DiC18** in THF were well overlapped. The excitation anisotropy of **DiC18**-loaded QSs decreased at a higher loading of the dye (Figure 3.4d), likely as an effect of the homoresonance energy transfer between DiC18 molecules experiencing close proximity at higher loadings. The higher anisotropy showed by the **C-QS** samples compared to that by **DiC18** in glycerol proves that the incorporation in QSs effectively restricted its rotational diffusion, reducing the possibility of nonradiative decay. The decrease of quantum yields and lifetime for QSs with increasing loading of **DiC18** further supported the homoenergy transfer process. Absorption, excitation, and emission spectra of **DiC18** nanoparticles, prepared by

reprecipitation, are displayed in Figure 3.5. In comparison with **DiC18**-loaded QSs, the emission band for the NPs exhibited a slight bathochromic shift to 472 nm, and the fluorescence quantum yield decreased from 0.46 for **C-QS-1** to 0.1 for the NPs. The desirable photophysical properties and generally high quantum yields of **DiC18**-loaded QSs indicated that quatsomes are promising vehicles to disperse hydrophobic probes in aqueous environments, achieving bright and stable fluorescent architectures that possess significant potential in fluorescence bioimaging. Similar results were obtained for **MKC**-based QSs (**M-QS**, Table 3.3).
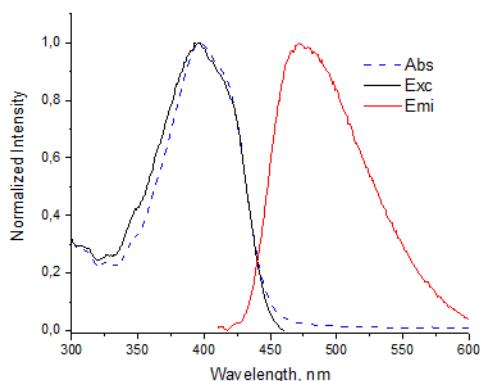
Figure 3.5 Normalized absorbance, excitation, and emission of **DiC18** NPs prepared by reprecipitation.

The optical stability of the **C-QS** and **M-QS** samples was studied by monitoring their absorption spectra over time Notably, no changes in the absorption band shapes or in intensities were detected over 2 months, evidencing the superior stability of these fluorescent nanostructures.

3.25 pH Sensitivity Measurements

A primary function of lysosomes in cells is to work as a digestive system by using an array of enzymes that are capable of breaking down many types of biological macromolecules.

It is essential for a lysosomal probe to be stable in an acidic environment because all of the lysosomal enzymes are acidic hydrolases, which are active at the acidic pH (about 5) that is maintained within lysosomes.[104, 120] The pH stability of **C-QS-1**, **-2**, and **-3** and **M-QS-1**, **-2**, and **-3** was investigated by measuring the steady-state absorption and emission spectra in a phosphate-buffered saline (PBS) solution at various pHs. As illustrated in Figure 3.6, only small fluctuations were observed in the absorption and emission spectra, indicating the good stability of **C-QS-1**, **-2**, and **-3** and **M-QS-1**, **-2**, and **-3** over the pH range of 4.10−10.32 (representative data for **C-QS-3** and **M-QS-3** are provided).
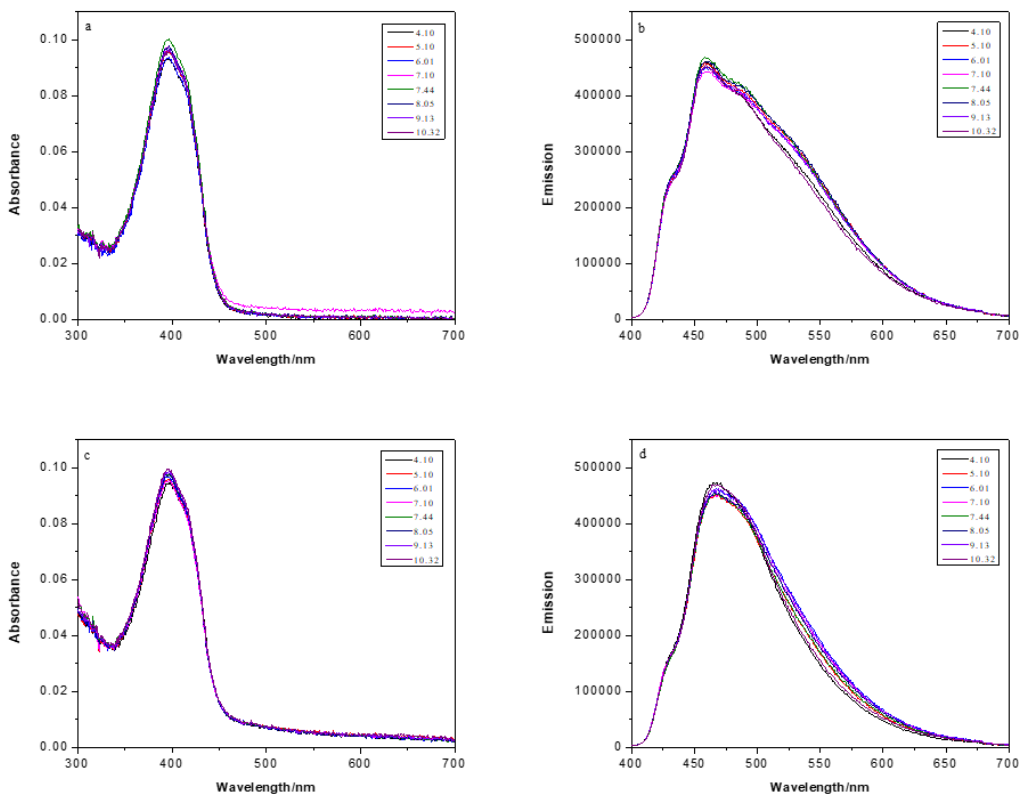
Figure 3.6 pH sensitivity measurements.

3.26 Cell Viability

To ascertain the potential utility of fluorescent probe DiC18 and DiC18-loaded QSs for cellular imaging, cell viability assays in HeLa and HCT 116 cells were conducted via the MTS assay.[104,117]Cell viability experiments in HeLa cells were performed for **C-QS-1**, **-2**, and **-3** and **M-QS-1**, **-2**, and **-3** (Figure 3.7). CTAB and MKC are quaternary ammonium surfactants, and their cytotoxicity to different human cells was previously reported.[121,122] The results show that the effect of DiC18 loading is negligible, and the cytotoxicity is governed by the concentration of the surfactant (CTAB or MKC). Good viability was obtained for **C-QS** at a concentration of 0.022 mM CTAB and for **M-QS** at a concentration of 0.044 mM MKC, respectively.

CTAB nominal concentration (mM)

Group	1	2	3	4	5	6
CTAB (mM)	0.022	0.044	0.88	0.175	0.35	0.70
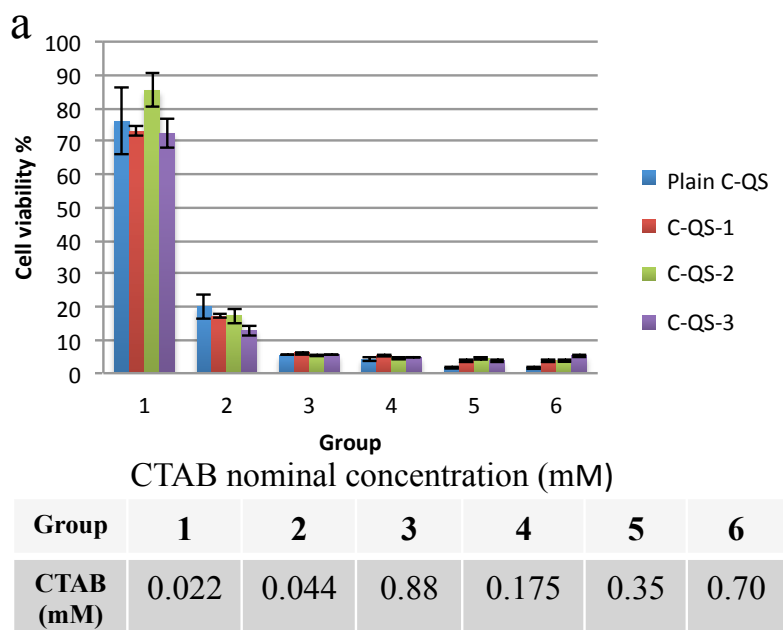
Figure 3.7 Cell viability assay of HeLa cells incubated with (a) plain **C-QS** and **C-QS-1**, **-2**, and **-3**; (b) plain **M-QS** and **M-QS-1**, **-2**, and **-3**, at various concentrations. (continued)

b

Group	1	2	3	4	5
MKC (mM)	0.044	0.088	0.18	0.35	0.7
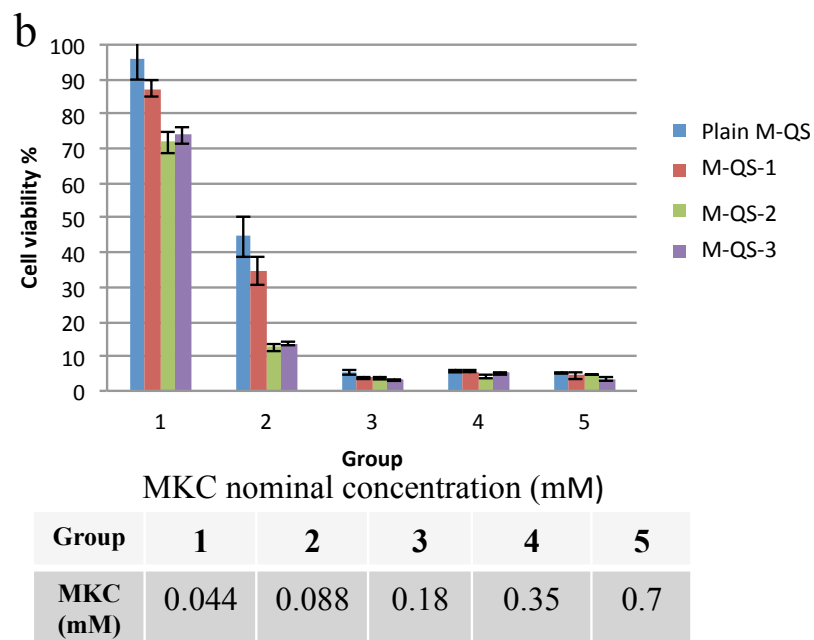
Figure 3.7 (continued) Cell viability assay of HeLa cells incubated with (a) plain **C-QS** and **C-QS-1**, **-2**, and **-3**; (b) plain **M-QS** and **M-QS-1**, **-2**, and **-3**, at various concentrations.

3.27 Cell Imaging and Cellular Colocalization Study

For demonstration purposes, fluorescence imaging was performed in an epithelial colorectal carcinoma cell line, HCT 116, for organic probe DiC18 and QS probes C-QS-1, -2, and -3 and M-QS-1, -2, and -3. On the basis of the cell viability test results, 20 μM of DiC18 and various amounts of C-QS-1, -2, and -3 and M-QS-1, -2, and -3 were employed for cell incubation and fluorescence imaging. Cells treated with DiC18 for 2 h displayed no fluorescence upon excitation, likely because DiC18, after dissolution in DMSO, underwent aggregation when diluted by a growth medium and was not uptaken by cells. In comparison, cells incubated with C-QS-3 and M-QS-3 provided bright images, manifesting the good biological compatibility of QSs and the capability of introducing organic fluorescent molecules into cells for in vitro (Figure 3.8) or in vivo applications. Images acquired from cells treated with C-QS-1 and -2 and M-QS-1 and -2 showed weaker

fluorescence due to the low loading of DiC18 in QSs (not shown) and hence studies focused

on **C-QS-3** and **M-QS-3**.
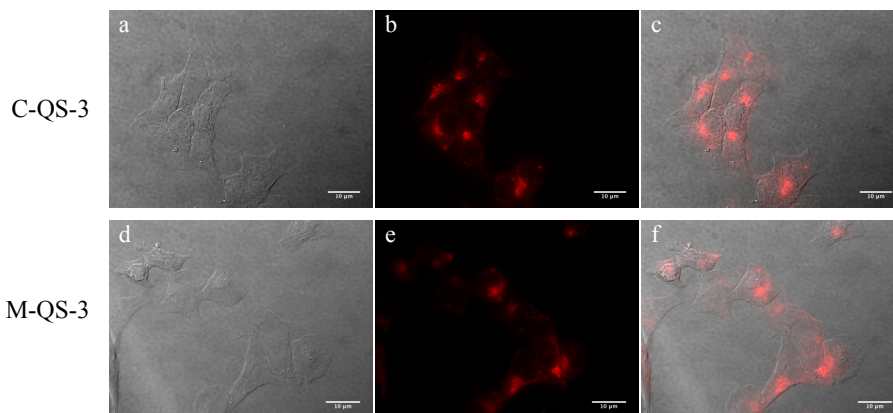
Figure 3.8 Fluorescence images of HCT 116 cells incubated with **C-QS-3** (0.022 mM, 2 h) and **M-QS-3** (0.044 mM, 2 h). (a,d) DIC; (b, e) fluorescence images; (c, f) merged images; 60x oil immersion objective.

Subsequently, to demonstrate the cellular distribution of **C-QS-3** and **M-QS-3**, colocalization experiments were conducted in both HCT 116 and COS-7 cells, two commonly employed cell lines.[104,105,112] The lysosomal marker, Lysotracker Red, and the mitochondria marker, Mitotracker Red, were employed for comparison to determine potential organelle selectivity. Fluorescence images collected for cells coincubated with commercial markers and QSs indicate that the localization of **C-QS-3** and **M-QS-3** was coincident to that of Lysotracker Red (Figures 3.9, 3.10, 3.11, and 3.12). Pearson's correlation coefficient, determined using freely available Fiji software, for **C-QS-3** and **M-QS-3** relative to Lysotracker Red was 0.89 and 0.92, respectively, whereas relative to Mitotracker Red the values were 0.32 and 0.30, respectively, demonstrating high selectivity toward lysosomes.
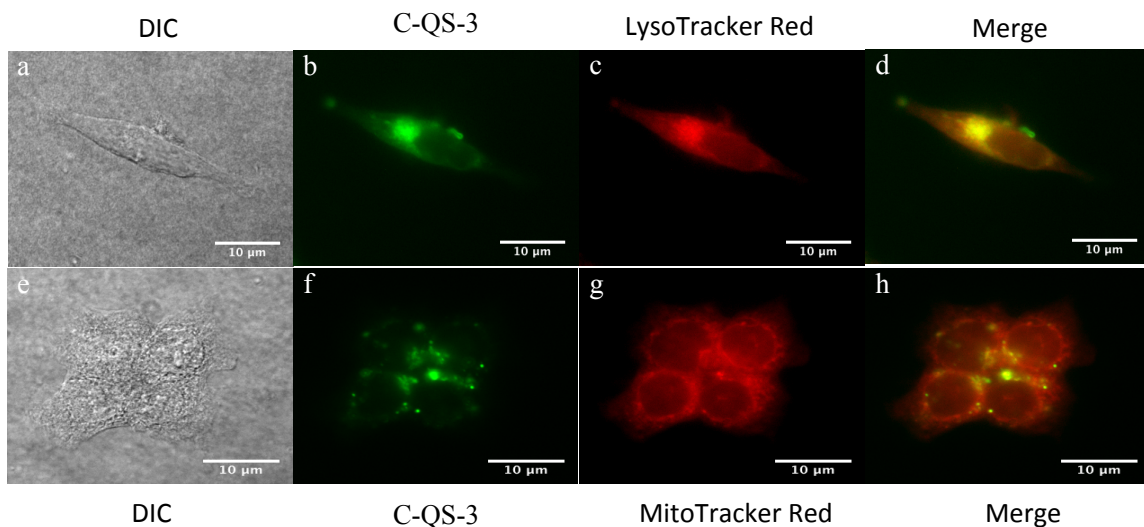
Figure 3.9 Fluorescence and colocalization images of HCT 116 cells incubated with **C-QS-3** (0.022 mM, 2 h), and Lysotracker Red (75 nM, 2 h) or Mitotracker Red (400 nM, 45 min). (a, e) DIC; Fluorescence images of (b, f) **C-QS-3**; (c) Lysotracker Red (f) Mitotracker Red; and (d, h) merged images; 60x oil immersion objective.
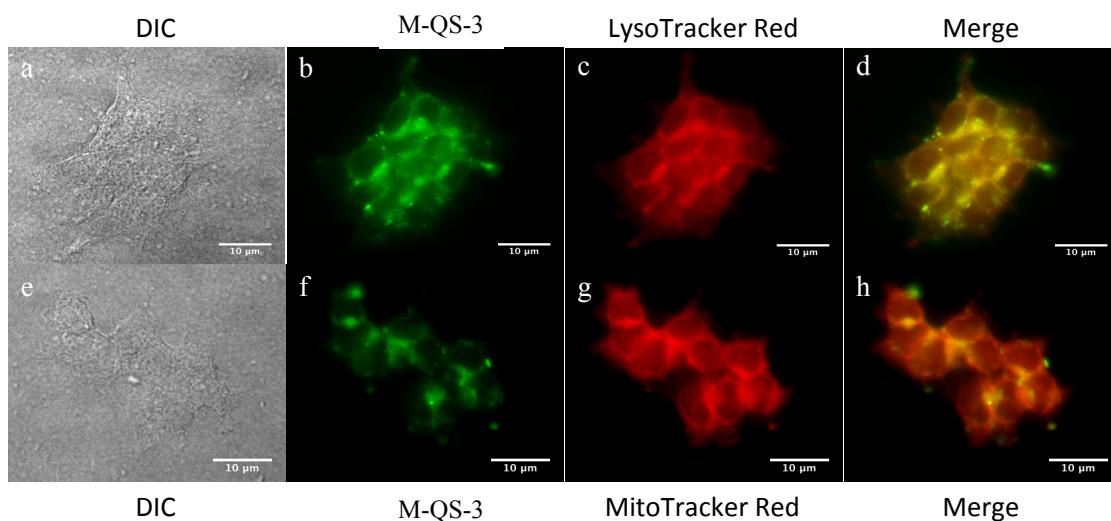
Figure 3.10 Fluorescence and colocalization images of HCT 116 cells incubated with **M-QS-3** (0.044 mM, 2 h), and Lysotracker Red (75 nM, 2 h) or Mitotracker Red (400 nM, 45 min). (a, e) DIC; Fluorescence images of (b, f) **M-QS-3**; (c) Lysotracker Red (f) Mitotracker Red; and (d, h) merged images; 60x oil immersion objective.

C-QS-3   LysoTracker Red   Merge

C-QS-3   Mitotracker Red   Merge
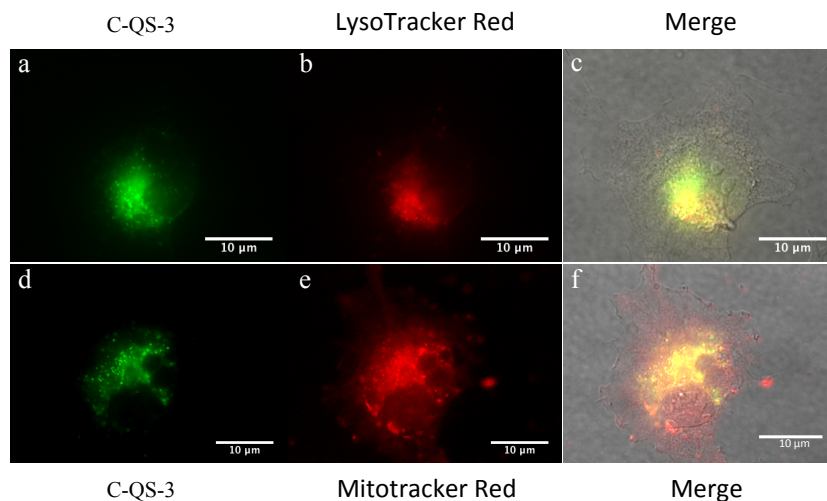
Figure 3.11. Fluorescence and colocalization images of COS-7 cells incubated with **C-QS-3** (0.022 mM, 2 h), and Lysotracker Red (75 nM, 2 h), or Mitotracker Red (400 nM, 45 min). Fluorescence images of (a, d) **C-QS-3**; (b) Lysotracker Red; (e) Mitotracker Red; and (c, f) merged images; 60x oil immersion objective.

M-QS-3   LysoTracker Red   Merge

M-QS-3   Mitotracker Red   Merge
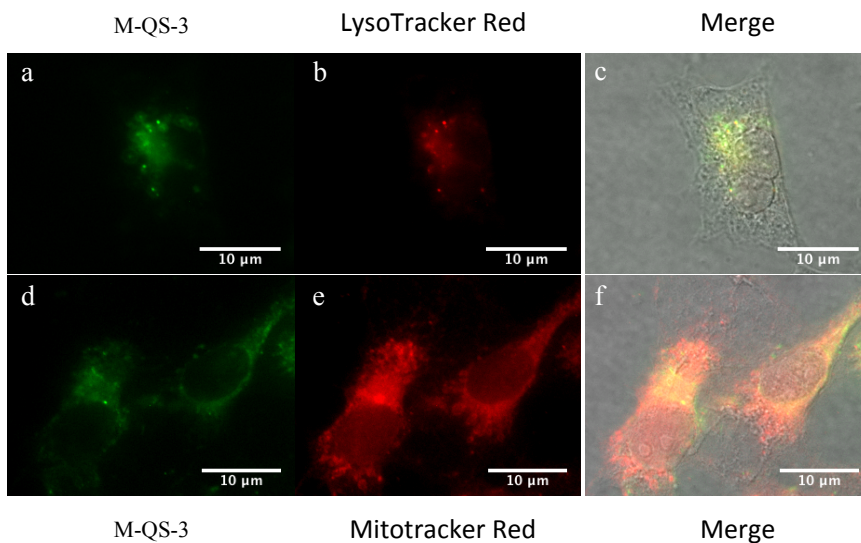
Figure 3.12 Fluorescence and colocalization images of COS-7 cells incubated with **M-QS-3** (0.044 mM, 2 h), and Lysotracker Red (75 nM, 2 h), or Mitotracker Red (400 nM, 45 min). Fluorescence images of (a, d) **M-QS-3**; (b) Lysotracker Red; (e) Mitotracker Red; and (c, f) merged images; 60x oil immersion objective.

3.28 Time-Dependent Lysosome Tracking Experiment

Time-dependent lysosome tracking experiments were performed to assess the intracellular retention of quatsome probes in cancer cells.[104,112] After a 2 h treatment with Lysotracker Red and **C-QS-3** or **M-QS-3**, HCT 116 cells were incubated for an additional 2, 4, and 6 h, respectively. As shown in Figures 3.13 and 3.14, there remained significant fluorescence in cells 8 h after initial incubation with the fluorenyl QS probes, maintaining its colocation with lysosomal markers, suggesting that **C-QS-3** and **M-QS-3** are promising candidates for long-term lysosomal tracking applications that can be used for monitoring lysosome distributions, activities, and related cell death.
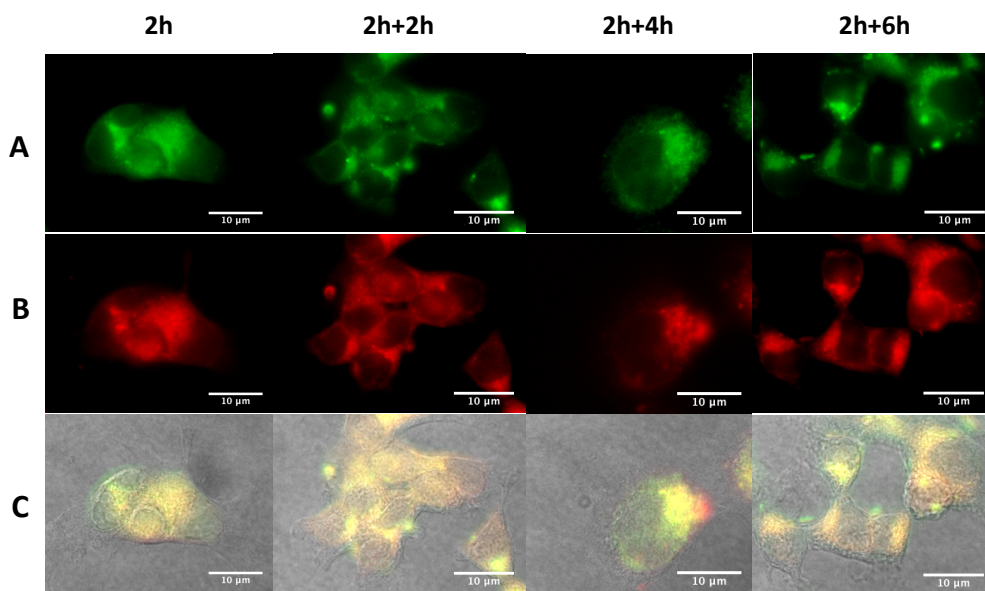
Figure 3.13 Time-dependent lysosome tracking of HCT 116 cells incubated with **C-QS-3** (0.044 mM, 2 h), and Lysotracker Red (75 nM, 2 h). Fluorescence images of (A) **C-QS-3**; (B) Lysotracker Red; and (C) merged images; 60x oil immersion objective.
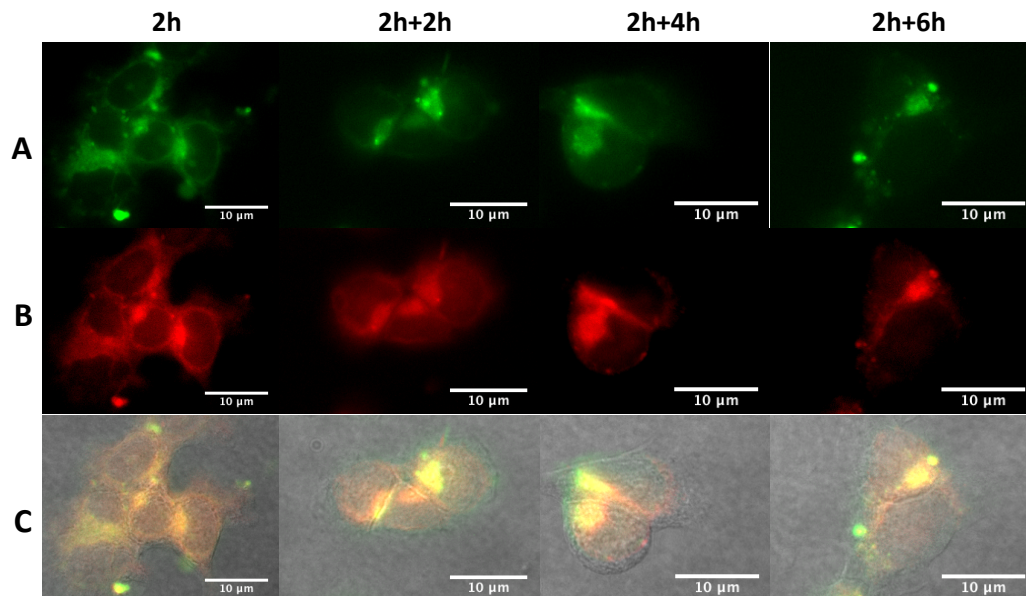
Figure 3.14 Time-dependent lysosome tracking of HCT 116 cells incubated with **M-QS-3** (0.044 mM, 2 h), and Lysotracker Red (75 nM, 2 h). Fluorescence images of (A) **M-QS-3**; (B) Lysotracker Red; and (C) merged images; 60x oil immersion objective.

3.3 Experimental Section

3.31 Materials

5-Cholesten-3β-ol (Chol, purity 95%) was purchased from Panreac (Barcelona, Spain). Hexadecyltrimethylammonium bromide (CTAB, BioUltra for molecular biology ≥99.0%) was purchased from Sigma-Aldrich. Tetradecyldimethylbenzylammonium chloride (MKC) was purchased from FeF Chemicals. All other chemicals reagents were purchased from Fisher Scientific or Sigma Aldrich, and used as received unless otherwise noted. Milli-Q water was used for all the samples preparation (Millipore Ibérica, Madrid, Spain). Ethanol (Teknocroma Sant Cugat del Vallès, Spain) was purchased in high purity. Carbon dioxide (99.9% purity) was purchased from Carburos Metálicos S.A. (Barcelona, Spain). All reagents and solvents were purchased from commercial suppliers and used without further purification. Intermediates **1** and **2** were prepared according to their respective literature reports. ^{1}H and ^{13}C NMR spectra were carried out in CDCl$_3$ solution on a Bruker AVANCE spectrometer (400 MHz).

3.32 Synthesis of 2-(7-bromo-9,9-diethyl-9H-fluoren-2-yl)benzo[d]thiazole (3)

To a solution of **2** (0.85 g, 2.0 mmol) and 2-(tri-*n*-butylstannyl)benzothiazole (0.84 g, 2.0 mmol) in 10 mL anhydrous toluene was added Pd(PPh$_3$)$_4$ (0.23 g, 0.2 mmol) under N$_2$ atmosphere. The reaction mixture was heated to reflux for 8 h under N$_2$. After cooling to room temperature, the solvent was removed under reduced pressure. The crude mixture was purified by flash column chromatography using ethyl acetate/hexanes (1/10), affording the desired compound **3** as white powder (0.37 g, 43%). ^{1}H NMR (400 MHz, CDCl$_3$): δ (ppm) 8.13 – 8.09 (m, 2H), 8.04 (d, *J* = 7.9 Hz, 1H), 7.92 (d, *J* = 7.9 Hz, 1H), 7.77 (d, *J* = 7.9 Hz, 1H), 7.62 (d, *J* = 8.4 Hz, 1H), 7.50 (s, 3H), 7.40 (t, *J* = 7.5 Hz, 1H), 2.20 – 2.03 (m, 4H), 0.35 (t, *J* = 7.3 Hz, 6H). ^{13}C NMR (101 MHz, CDCl$_3$): δ (ppm) 168.54, 154.53, 153.13, 150.73, 143.61, 139.80, 135.29, 133.12, 130.53, 129.17, 127.80, 127.51, 126.67, 126.51, 125.31, 123.35, 122.32, 121.96, 121.72, 120.33, 57.03, 32.80, 8.65. HRMS (ESI, m/z): calcd for C$_{24}$H$_{20}$BrNS ([M+H]$^+$) 434.0573; found 434.0587.

3.33 Synthesis of 7-(benzo[d]thiazol-2-yl)-9,9-diethyl-N,N-di-*n*-octadecyl-9H-fluoren-2-amine (DiC18)

A mixture of **3** (0.13 g, 0.3 mmol), N, N-di-*n*-octadecylamine (0.31 g, 0.6 mmol), Pd(OAc)$_2$ (0.020 g, 0.03 mmol), (*t*-Bu)$_3$P (0.012 g, 0.06 mmol), and *t*-BuONa (0.058 g, 0.6 mmol) in 5 mL anhydrous toluene was heated to reflux under N$_2$ atmosphere for 16 h. Toluene was removed *in vacuo* after the reaction mixture was cooled to room temperature. The residue was dissolved with 10 mL CH$_2$Cl$_2$ and washed twice with 10 mL brine. The organic layer was dried over MgSO$_4$, then concentrated under reduced pressure. The crude product was purified by flash column chromatography using ethyl acetate/pentane (1/200) as eluent, providing **DiC18** as yellow oil (0.22 g, 84%). ^{1}H NMR (400 MHz, CDCl$_3$): δ (ppm) 8.13

– 8.06 (m, 2H), 7.99 – 7.90 (m, 2H), 7.62 – 7.58 (m, 1H), 7.53 – 7.49 (m, 2H), 7.37 – 7.42

(m, 1H), 6.66 (d, J = 8.4 Hz, 1H), 6.60 (s, 1H), 3.45 – 3.27 (m, 4H), 2.20 – 1.99 (m, 4H),

1.65 (s, 4H), 1.29 (s, 60H), 0.93 – 0.89 (m, 6H), 0.42 (t, J = 7.2 Hz, 6H). ^{13}C NMR (101

MHz, CDCl$_3$): δ (ppm) 169.47, 154.69, 152.78, 150.01, 149.29, 146.03, 135.18, 131.08,

130.20, 129.18, 127.81, 127.44, 126.46, 126.26, 125.34, 124.82, 123.53, 123.02, 121.59,

121.32, 118.24, 111.43, 106.59, 56.30, 51.66, 44.07, 33.15, 32.10, 29.87, 29.72, 29.51,

29.37, 27.56, 27.43, 22.83, 22.34, 14.19, 8.77. HRMS (DART, m/z): calcd for C$_{60}$H$_{94}$N$_2$S

([M+H]$^+$) 875.7210; found 875.7239.

3.34 Preparation of DiC18-loaded quatsomes by DELOS-SUSP

DELOS-SUSP (*depressurization of an expanded liquid organic solution-suspension*), a

compressed fluids (CFs) based method, was used for the preparation of **DiC18**-loaded

quatsomes (QSs). Cholesterol (111 mg) was first dissolved in 4.2 mL of EtOH at working

temperature T_w (T_w=308 K) along with a determined amount of **DiC18** (described below

and in the Supporting Information). The solution was then added to a high-pressure vessel

(V=11.8 mL) at atmospheric pressure and T_w. After 20 minutes of equilibration, the vessel

was pressurized with CO$_2$ at the working pressure P_w (P_w=10 MPa) in order to have an

expanded liquid ethanol solution with a molar fraction of CO$_2$ of X_{CO2}=0.63. The reactor

was kept at the working condition for 1 h in order to homogenize the system. The organic

solution was then depressurized over 35 mL of water, where 100 mg of CTAB (or 202 mg

of MKC) had been previously dissolved. N$_2$ at 10 MPa was added to the vessel during the

depressurization in order to maintain constant Pw inside. The vessel was equipped with a

gas filter, in order to prevent any unsolved compound present in the CO$_2$-expanded solution

to reach the aqueous solution of the surfactant. With this one-step method, unilamellar

vesicles with high vesicle-to-vesicle homogeneity were preparedenabling the straightforward loading of quatsomes with hydrophobic compounds such as **DiC18**.

The loading L is expressed as the ratio $L=\text{moles}_{DiC18}/(\text{moles}_{cholesterol} + \text{moles}_{surfactant})$. In the case of QSs made of CTAB/cholesterol (1:1 molar ratio), three different samples, referred to as **C-QS-1**, **-2**, and **-3**, having $L=$ 0.9, 7, and 13 x 10^{-3}, respectively, were prepared. In the case of MKC/cholesterol (1:2 molar ratio) QSs, three samples, **M-QS-1**, **-2**, and **-3**, with $L=$0.5, 4.8, and 9.7 x 10^{-3}, respectively, were synthesized. The concentrations of **DiC18** in the respective samples were determined as explained in the Supporting Information, while the nominal concentrations of surfactants and cholesterol were used for the determination of L. All samples were purified by diafiltration by using Kros Flo Research Ii*i* TFF System (Spectrum Labs, USA) equipped with mPES Micro Kros filter column (100 kDa MWCO) in order to remove ethanol and excess of CTAB or MKC.

3.35 Preparation of DiC18 NPs by Reprecipitation

A solution of 0.5 mM **DiC18** in THF was filtered using a 220 nm pore size Teflon filter, and 100 µL of the filtered solution was then dropped into 9.9 mL of Milli-Q water at room temperature under vigorous stirring for 1 h.

3.36 Physical Characterization of DiC18-Loaded Quatsomes

Size and zeta potential of DiC18-loaded quatsomes were studied using dynamic light scattering (Malvern Zetasizer Nano ZS, Malvern Instruments, U.K.) with noninvasive backscattering optics, equipped with a He−Ne laser at 633 nm. All values reported were the average of three consecutive measurements of the same samples at 25 °C (standard deviation over the three measurements <7%). Values were reported as average

hydrodynamic diameters ± PDI (polydispersity index in nm). CryoTEM images were acquired with a JEOL JEM microscope (JEOL, Tokyo, Japan) operating at 120 kV. The sample was placed in a copper grid coated with a perforated polymer film and then plunged into liquid ethane to freeze it. It was then placed into the TEM.

3.37 Photophysical Properties Measurements

Linear absorption, fluorescence, and excitation spectra of **DiC18**, **C-QS-1**, **-2**, and **-3**, and **M-QS-1**, **-2**, and **-3** were investigated in spectroscopic grade HEX, CHX, TOL, DCM, ACN, DMSO, glycerol, and Milli-Q water at room temperature. The steady state absorption spectra were measured with a Tecan Infinite M200 PRO plate reader spectrometer in 1 cm path length quartz cuvettes. The fluorescence and excitation spectra were obtained using an Edinburgh Instruments FLS980 fluorescence spectrometer. Solutions studied during all of the measurements had optical densities less than 0.1. The fluorescence spectra were corrected for the spectral responsivity of the photomultiplier tube detector. Excitation anisotropy measurements for **DiC18** were performed in a viscous solvent to impede molecular rotational relaxation. The fluorescence quantum yields were determined relative to 9,10-diphenylanthracene in cyclohexane (Φ = 0.95) as the standard.[117,119] The values were calculated according to

$$\phi_{sample} = \phi_{ref} \frac{OD_{ref} I_{sample} n_{sample}^2}{OD_{sample} I_{ref} n_{ref}^2} \tag{3.1}$$

where Φ is the quantum, I is the integrated emission signal, OD is the optical density at the excitation wavelength, and n is the refractive index; subscript "ref" stands for reference

sample, "sample" stands for experimental sample. It is important to take into account that at the concentrations studied, Quatsomes scatter UV−vis light. To accurately measure and calculate the quantum yield for **C-QS-1** and **M-QS-1** (samples with a low absorption/scattering ratio), contribution of scattered light was subtracted from the absorption spectra. The signal detected from the spectrophotometer can be partitioned into light that is actually absorbed ($A_{corrected,\lambda}$) and the apparent absorption that is due to light scattering at a given wavelength ($A_{LS,\lambda}$). The apparent absorption spectrum of plain QSs can be modeled with eq 3.2, in accordance with Rayleigh−Tyndall approximation

$$A_{LS,\lambda} = a\lambda^n \tag{3.2}$$

where *a* and *n* were determined by the least squares fitting of the measured absorption spectrum at wavelengths larger than those in which absorption of **DiC18** was observed. After scattering subtraction, the condition $Abs_{333nm} = 0.32Abs_{MAX}$, verified for **C-QS-2** and **-3** samples and, therefore, independent of the **DiC18** loading, was also verified for **C-QS-1**. However, owing to this mathematical treatment for scattering removal, the fluorescence quantum yield of **C-QS-1** shall be considered as an approximated value and simply used for comparison purpose with the other samples studied.

For pH sensitivity measurements, the steady-state absorption spectra of **C-QS-3** and **M-QS-3** at various pHs in the PBS solution were recorded using a Tecan Infinite M200 PRO plate reader spectrometer in 1 cm path length quartz cuvettes. Likewise, pH-dependent fluorescence spectra were obtained using an Edinburgh Instruments FLS980 fluorescence spectrometer.

3.38 Cell Viability, Imaging and Colocalization Study

To assess the cytotoxicity of **DiC18**, **C-QS-1**, **-2**, and **-3**, and **M-QS-1**, **-2**, and **-3**, HCT 116 and HeLa cells were cultured in the minimum Eagle's essential medium (MEM) and Dulbecco's modified Eagle's medium (DMEM) cell medium supplemented with 10% fetal bovine serum, 1% penicillin, and streptomycin at 37 °C and 5% CO_2. Cells were placed in 96 well plates and incubated until there were no fewer than 6×10^3 cells per well for the experiments. Next, HCT 116 cells were incubated with different concentrations of **DiC18** (1.25, 2.5, 5, 10, 20, and 40 μM) for an additional 22 h. HeLa cells were incubated with different concentrations of **C-QS-1**, **-2**, and **-3** (0.022, 0.044, 0.088, 0.175, 0.35, and 0.70 mM) and **M-QS-1**, **-2**, and **-3** (0.044, 0.088, 0.18, and 0.35 mM) for an additional 22 h, where the values within parentheses refer to the nominal concentrations of the surfactants. After that, 20 μL of the CellTiter 96 Aqueous One solution reagent (for MTS assay) was added into each well, followed by further incubation for 2 h at 37 °C.[104,118,123] The respective absorbance values were read on a Tecan Infinite M200 PRO plate reader spectrometer at 490 nm to determine the relative amount of formazan produced. Cell viabilities were calculated on the basis of the following equation

$$Cell\ Viability\,(\%) = \frac{Abs^s{}_{490nm} - Abs^D{}_{490nm}}{Abs^c{}_{490nm} - Abs^{D2}{}_{490nm}} \times 100\% \tag{3.2}$$

where Abs^s 490nm is the absorbance of the cells incubated with different concentrations of experimental probe solutions, Abs^D 490nm is the absorbance of cell-free well containing only dye at the concentration that was studied, Abs^c 490nm is the absorbance of cells only incubated in the medium, Abs^{D2} 490nm is the absorbance of the cell-free well.

For cell imaging, HCT 116 cells were placed onto poly-Dlysine- coated coverslips and transferred into 24-well glass plates (5×10^4 cells per well), and incubated for 48 h before incubating with the quatsome. A stock solution of the fluorescent probe of **DiC18** dissolved in DMSO was prepared as a 2 mM solution. The solution was diluted to 5, 10, 15, and 20 μM by the complete growth medium, DMEM, and freshly incubated with HCT 116 cells for 2 h. After incubation, the dye solutions were extracted and the coverslipped cells were washed twice with the PBS solution. Cells were then fixed with 3.7% formaldehyde solution in the PBS solution for 10 min. The fixing agent was extracted and washed twice with PBS. To reduce the autofluorescence, a fresh solution of $NaBH_4$ (1 mg/ mL) in the PBS buffer was used to twice treat the fixed cells for 10 min. The coverslipped cells were then washed twice with PBS and then with deionized (DI) water and mounted on microscope slides using an antifade mounting media (Prolong Gold).

Stock solutions of **C-QS-1**, **-2**, and **-3** were diluted to a nominal concentration of 0.022 μM of CTAB by the DMEM cell medium, whereas stock solutions of **M-QS-1**, **-2**, and **-3** were diluted to a nominal concentration of 0.044 μM of MKC by the DMEM cell medium. The incubation and fixation procedures were repeated for these six experimental solutions. Fluorescence microscopy images were observed and recorded on an inverted microscope (Olympus IX70) equipped with a QImaging cooled charge-coupled device (CCD) and a 100 W mercury lamp. To improve the fluorescence background-to-image ratios, fluorescence images were obtained using a customized filter cube (Ex: 377/50; DM: 409; Em: 460/60).

For colocalization study, to investigate the efficiency and specificity of **C-QS-3** and **M-QS-3**, HCT 116 and **COS-7** cell lines were employed. All cells were seeded on poly-

D-lysinecoated coverslips at the density of 4×10^4 cells per well and incubated for 48 h. Stock solutions of **C-QS-3** and **M-QS-3** dissolved in DI water were prepared at a nominal concentration of 1 mM. Lysotracker Red DND-99 (LT Red) was purchased as a 1 mM stock solution in anhydrous DMSO, and MitoTracker Red FM (MT Red) containing 50 μg of lyophilized solid per vial was dissolved in 69 μL of DMSO and prepared as a 1 mM stock solution. For coincubating cells with **C-QS-3** or **M-QS-3** and LT Red, the stock solution was diluted to 0.022 mM for CTAB and 0.044 mM for MKC and 75 nM LT Red with the DMEM cell medium and freshly placed over cells for a 2 h incubation period. For coincubating cells with **C-QS-3** or **M-QS-3** and MT Red, the stock solution was diluted to 0.022 mM for CTAB and 0.044 mM for MKC with the DMEM cell medium and freshly incubated with cells for 2 h, followed by incubation with 400 nM MT Red in the DMEM cell medium for an additional 45 min. Cells were washed twice with PBS and then fixed with 3.7% formaldehyde solution in PBS for 10 min. The fixing agent was extracted and washed twice with PBS. A fresh solution of NaBH4 (1 mg/mL) in PBS was used to twice treat the fixed cells for 10 min. The coverslipped cells were then washed twice with PBS and then with deionized water and mounted on microscope slides using an antifade mounting media (Prolong Gold). Fluorescence images of the fixed cells were obtained using a customized filter cube (Ex: 377/50; DM: 409; Em: 460/60) for **C-QS-3** and **MQS-3**; a Texas Red filter cube (Ex: 562/40; DM: 593; Em: 624/40) was employed for Lysotracker Red and MitoTracker Red FM imaging. Pearson's correlation coefficient for **C-QS-3** and **M-QS-3** was calculated using Fiji, a freely available image processing software.

3.39 Time-Dependent Lysosome Tracking Experiment

To track the QS probe cellular distribution in cancer cells, HCT 116 cells were placed onto poly-D-lysine-coated coverslips and transferred into 24-well glass plates (5×10^4 cells per well) and then incubated for 48 h before incubating with the QS probe. The stock solution was diluted to a final concentration (0.022 mM for CTAB and 0.044 mM for MKC) and 75 nM LT Red with the DMEM cell medium. Cells were incubated with solutions for a 2 h incubation period and washed thoroughly and then incubated with fresh DMEM medium for an additional 2, 4, and 6 h. After incubation, cells were washed twice with PBS and then fixed with 3.7% formaldehyde solution in PBS for 10 min. The fixing agent was extracted and washed twice with PBS. A fresh solution of NaBH4 (1 mg/mL) in PBS was used to twice treat the fixed cells for 10 min. The coverslipped cells were then washed with the PBS buffer twice and then with deionized water and mounted on microscope slides with Prolong gold mounting media. Fluorescence microscopy images were recorded on an inverted microscope (Olympus IX70) equipped with a QImaging cooled CCD and a 100 W mercury lamp. Fluorescence images of the fixed cells were taken using a customized filter cube (Ex: 377/50; DM: 409; Em: 460/40) for **C-QS-3** and **M-QS-3**; a Texas Red filter cube (Ex: 562/40; DM: 593; Em: 624/40) was utilized for imaging Lysotracker Red.

3.4 Conclusion

A new lysosome-specific fluorescent nanostructured probe has been obtained by using quatsomes to stably disperse a nonwater soluble fluorene derivative (**DiC18**) in aqueous media. Despite the morphological heterogeneity, QS probes **C-QS-1**, **-2**, and **-3** and **M-QS-1**, **-2**, and **-3** formed patchy quatsomes and exhibited good stability, both in terms of

colloidal and spectral properties, over 2 months. Fluorescence quantum yields were generally high for the fluorenyl-based probes, and fluorescence anisotropy spectra indicated that DiC18 exists in a highly anisotropic environment in the patchy- QSs. The study of their photophysical properties indicates that these QS nanovesicles are desirable fluorescent probes for in vitro cell imaging. The cytotoxicity of these patchy-quatsomes was assessed in HCT 116 cell lines and found to be suitable for fluorescence image acquisition. Fluorescence microscopy images showed that **C-QS-3** and **M-QS-3** are two highly selective lysosomal probes with high Pearson's correlation coefficients relative to commercial Lysotracker Red. In conclusion, **C-QS-3** and **M-QS-3** were useful in time dependent lysosomal tracking, fulfilling a number of requirements necessary for an efficient lysosome-selective fluorescent probe, including high stability and specificity, possibility of long-term imaging, and pH insensitivity. These properties make the fluorenyl-loaded QS nanoprobes particularly intriguing candidates for further studies, such as the inclusion of activities for lysosomal-addressed drug delivery and photodynamic therapy.

CHAPTER 4

TUMOR VASCULAR IMAGING USING POLYMER NANOPARTICLES IN THE NEAR-INFRARED WINDOW

Deep tissue neovasculature imaging and the observation of tumor angiogenesis represent important aspects of early cancer diagnosis and treatment. Here, novel, peptide-functionalized lipophilic nanoparticles (NPs) were synthesized to encapsulate a squaraine-based fluorophore that can be excited via one-photon absorption in the far-red or two-photon absorption in the near-infrared (NIR) window, both resulting in far-red to NIR emission. Poly(maleic anhydride-alt-octadec-1-ene) (PMAO) as the coating shell was prepared by a co-precipitation method followed by two modification steps. Vasculature imaging was facilitated by conjugation of a cyclic RGD peptide (c(RGDfK)), to target $\alpha_v\beta_3$ integrin proteins expressed by the endothelial cells of neovasculature. Efficient cellular uptake and bright two-photon fluorescence microscopy (2PFM) tissue imaging demonstrated the potential application of the functionalized NP probe in tumor angiogenesis imaging and as a potential contrast agent for early stage cancer detection and therapeutic monitoring.

4.1 Introduction

Angiogenesis, the development of new capillaries by sprouting and branching from pre-existing microcapillaries, is an essential process in organ development and tissue repair, yet also promotes chronic inflammation, tumor progression, and tumor metastasis.[123,124] Pathological angiogenesis occurs in growing tumors as well as in a range of non-neoplastic diseases that could be classed as "angiogenesis-dependent diseases".[125] Therefore, it is of

great importance to target, observe, and monitor the activation and inhibition of angiogenesis processes. The abnormalities of tumor tissues provide the opportunity to target and destroy tumors without damaging the microvasculature of healthy tissue.[126] The expression of certain types of integrin proteins in tumor vasculature that is undergoing angiogenesis is a prominent molecular difference to normal blood vessels.[127] Integrins are divalent cation-dependent membrane glycoproteins that promote cell attachment and migration in the surrounding extra cellular matrix (ECM), are composed of non-covalently associated α and β subunits, and are key regulators of tumor angiogenesis.[128,129] Linear arginine-glycine-aspartic acid (RGD)-containing peptides have the ability to interact with the integrin families with distinctively different affinities due to the variance in the conformation and sequential environment of RGD sites.[130,131] It has been demonstrated that the cyclic peptide c(RGDfK) binds to $\alpha_v\beta_3$ integrin with high selectivity.[131,132] Therefore, targeted delivery of contrast agents or therapeutic materials to $\alpha_v\beta_3$ integrin during angiogenesis can be accomplished by the use of materials conjugated to RGD-containing peptides.[133-135]

The development of new organic probes with excellent photophysical properties, e.g., high fluorescence quantum yield and high photostability, is of considerable interest to a number of emerging technologies, including solar energy conversion,[136,137] optical data storage,[133,138,139] fluorescence-based sensing methodologies,[134,140] and cancer therapy.[141-143] Time-dependent observation of biological specimens is challenged by light scattering and photodamage caused by excessive excitation energy, particularly in the UV to the mid-visible spectral range.[142] Near-infrared (NIR) emitting compounds, capable of undergoing two-photon absorption (2PA), such as squaraine dyes, are desirable for noninvasive

67

quantification and visualization via optical imaging in the window between 700 and 1000 nm. The applications of combining powerful imaging methods, such as two-photon fluorescence microscopy (2PFM), with novel fluorescent probes having high photostability, low toxicity, as well as high fluorescence quantum yields are of appreciable interest.[141-145]

The hydrophobicity and poor availability in aqueous media of organic fluorescent molecules often severely limits their utility in biological applications. Several approaches have been pursued to overcome this critical issue, with each having merits and restrictions.[145,146] Strategies consisting of dispersing organic probes in water-compatible nanostructures have been sought in various research areas.[147-150] Poly(maleic anhydride-*alt*-octadec-1-ene) (PMAO) is an amphiphilic alternating copolymer consisting of long aliphatic side chains and anhydride repeat units. Coating inorganic nanocrystals and organic compounds with PMAO has been reported with the ability to transfer them into aqueous media for biological imaging.[151-153] PMAO is expected to form nanoparticles via self-assemble in water, exposing the anhydride groups on the micelle's exterior, ready for further modification while sequestering the long alkyl chain interior to form a highly hydrophobic microenvironment for encapsulation of lipophilic organic compounds. [154]

Herein, a squaraine derivative (SD) was designed and synthesized. Its photophysical properties were investigated in solvents with various polarities by UV-visible absorption and fluorescence spectroscopy. To achieve water solubility while reducing fluorescence quenching caused by aggregation, PMAO was employed to encapsulate the hydrophobic **SD** fluorophore. Furthermore, $\alpha_v\beta_3$ integrin targeting was achieved by activating the nanoparticles' surface-functional groups, followed by

conjugation with a cyclic RGD-containing peptide (c(RGDfK)), where R, G, D, f, and K are the amino acids arginine, glycine, aspartate, D-phenylalanine, lysine, respectively. The c(RGDfK) functionalization resulted in nanoparticles containing multiple targeting moieties that is expected to lead to high target avidity. One- and two-photon fluorescence cell and tissue images support the integrin-dependent cell uptake and neovasculature endothelial cell targeting of the probes.

4.2 Results and Discussion

4.21 Synthetic Strategy

Figures 4.1 and 4.2 depicts the design of the novel squaraine probe **SD** and the amine terminated cyclic RGD-peptides conjugated nanoparticle. We prepared a D-A-D archetype squaraine derivative, where A represents an electron-withdrawing moiety and D represents an electron-donating moiety. It is known that squaraine compounds have the tendency to form aggregates in aqueous media, resulting in fluorescence quenching that severely limits their application in bioimaging.[155] In order to reduce the self-association of squaraine molecules, bulky groups were incorporated to the squaraine termini by coupling bis(2-ethylhexyl)amine with phloroglucinol.[156] In addition, two methoxy groups were introduced to the compound by modifying the OH groups *ortho* to the squarainyl ring in **SD**, by reaction of tetrahydroxy squaraine **B** with dimethyl sulfate, to further increase steric hindrance and attenuate its aggregation propensity.[157]
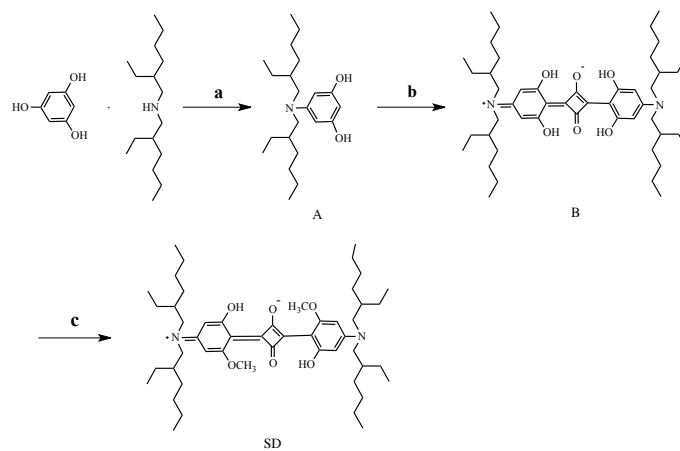
Reaction conditions: a) 1-butanol/toluene, refluxing; 51.8%. b) squaric acid, 1-butanol/toluene, refluxing with azeotropic distillation; 24.4%. c) dimethyl sulfate, potassium *tert*-butoxide, THF, r. t..

Figure 4.1 Synthesis of squaraine **SD**.
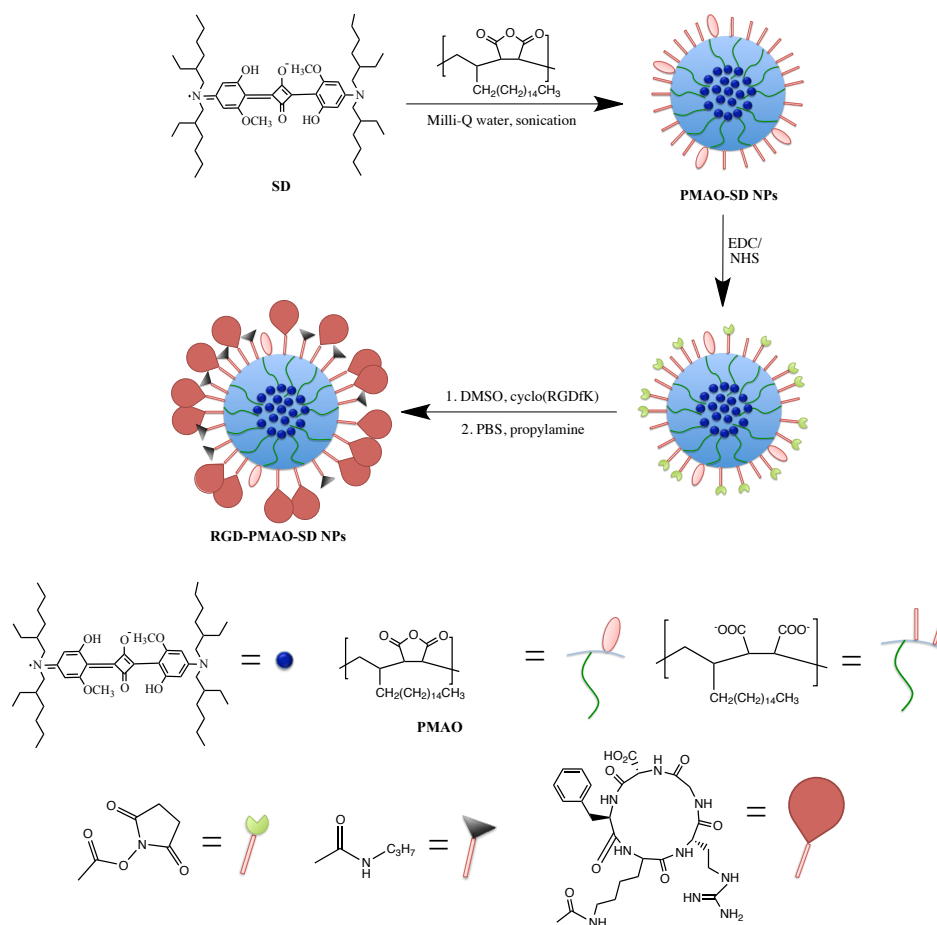
Figure 4.2 The synthetic route for the preparation of RGD-PMAO-SD nanoparticles.

To dissolve the hydrophobic squaraine, **SD** was encapsulated in PMAO nanoparticles by co-precipitating a mixture of poly(maleic anhydride-alt-octadec-1-ene) (PMAO) and **SD** in a THF solution into Milli-Q water under sonication, affording water-soluble PMAO-SD NPs.[154] The formation of PMAO-SD nanoparticles was confirmed using infrared spectroscopy. The anhydride repeat units on the nanoparticle's surface were hydrolyzed to provide carboxylate moieties that were further esterified with N-hydroxysuccinimide (NHS) in the presence of 1-ethyl-3-(3-dimethylaminopropyl)carbodiimide (EDC), providing activated ester functional groups on the NPs' surface. To achieve the specific $\alpha_v\beta_3$ integrin targeting, activated ester, amine-reactive nanoparticles were then conjugated with a cyclic peptide (Ar-Gly-Asp-D-Phe-Lys) c(RGDfK) at room temperature, affording the RGD-conjugated PMAO nanoparticles (pre-RGD-PMAO-SD NPs). Cellular uptake enhancement was achieved by the activation of the remaining carboxylic groups with NHS/EDC followed by reacting with *n*-propylamine to increase the zeta, ζ, potential of the NPs' surface (RGD-PMAO-SD NPs).

4.22 Photophysical Properties

Photophysical properties of **SD** were investigated in solvents with different polarities, including dimethyl sulfoxide (DMSO), acetonitrile (ACN), toluene (TOL), dichloromethane (DCM), and tetrahydrofuran (THF). The linear absorption, emission spectra, and photophysical properties of **SD** are shown in Figure 4.3 and Table 4.1. The absorption spectra exhibited maximum intensity in the range of 646 to 660 nm, with only nominal variation as a function of solvent polarity. Fluorescence spectra resulting from the excitation in the main absorption displayed a weak solvatochromic pattern with the maximum emission wavelength at 680 nm in DMSO and 659 nm in TOL, and extending

71

into the near-IR (NIR). The highest quantum yield was achieved in DCM (Φ_F=0.72) and decreased with increasing solvent polarity. However, no fluorescence could not be detected for **SD** in aqueous media (Figure. 4.4). The aggregation behavior of various squaraine derivatives have been widely studied in Langmuir-Blodgett films, aqueous solution and mixed aqueous-organic solution, and it is reasonable to assume that many squaraine aggregates exhibiting similar absorption spectra in microcrystals, films, or other media may show similar intermolecular arrangements based on previous studies.[158-160] The dimer absorbance band for squaraine derivatives that have similar structures with SD occurred in the range of 580 to 600 nm, consistent to what we observed.[159,160] Therefore, the loss of fluorescence of **SD** in aqueous media is likely the result of dimer formation caused by intermolecular interactions.[161,162] These properties and values are typical for squaraine dyes.[158, 163,164]

Figure 4.4 shows the comparative absorption and fluorescence spectra of water-dispersed PMAO-SD NPs with compound **SD** itself. The absorption spectrum of PMAO-SD NPs in water displayed red shift ($\lambda_{abs, max}$= 651 nm) compared to the squaraine derivative **SD** ($\lambda_{abs, max}$= 628 nm). Importantly, the quantum yield was increased to ten percent after PMAO encapsulation, which suggested that **SD** has been successfully protected from aggregation and fluorescence quenching through embedding in the hydrophobic domain of the amphiphilic polymer. Moreover, the photophysical properties of RGD-PMAO-SD nanoparticles were investigated in DI water, PBS, Minimum Essential Media (MEM) without serum, and MEM. As shown in Figure 4.4, the absorption and emission spectra, no aggregation was evident in these media, and RGD-PMAO-SD

nanoparticles exhibited maximum absorption at 654 nm as well as maximum emission around 678 nm. The results demonstrate relatively high stability of the nanoparticle.
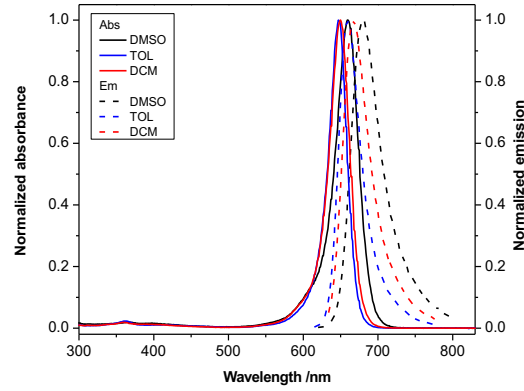
Figure 4.3 Normalized absorption and emission spectra of **SD** in DMSO, TOL, and DCM.
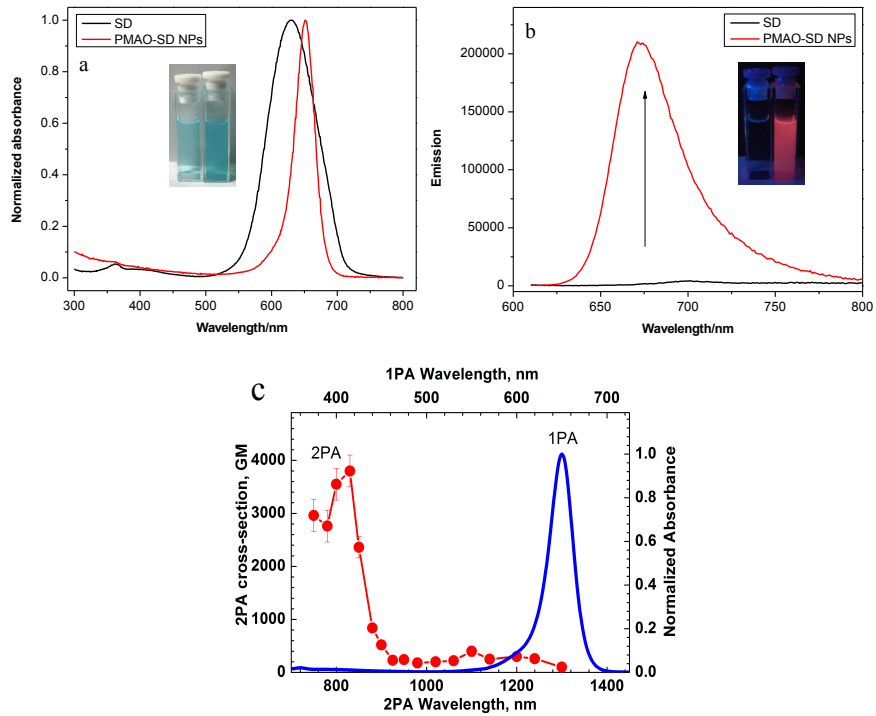
Figure 4.4 Normalized a, b) absorption and emission spectra of **SD** and PMAO-SD NPs in PBS buffer; c) 1PA spectrum (blue) and degenerate 2PA spectrum (red circles) of **SD**.

Table 4.1 Photophysical Properties for Compound **SD**

Solvent	λ_{ab}^a[nm]	λ_{em}^a [nm]	$\Delta\lambda^b$ [nm]	τ^c [ns]	Φ_f^d	$P(\varepsilon)^e$
DMSO	660	680	20	1.64	0.38	0.938
ACN	648	667	19	1.38	0.40	0.924
DCM	651	668	17	2.32	0.72	0.798
THF	647	662	15	1.92	0.64	0.687
TOL	646	659	13	2.26	0.81	0.408

[a] Absorption and emission maxima ±1 nm; [b] Stokes shift ±2 nm; [c] fluorescence lifetimes ±5%; [d] fluorescence quantum yield ±10%; [e] polarity factor calculated as $P(\varepsilon) = (\varepsilon-1)/(\varepsilon+2)$, where ε is the dielectric constant.

Squaraine **SD**, designed based on insight learned from previous efforts in our laboratory, was predicted to possess desirable 2PA properties.[165,166] The degenerate two-photon absorption spectra of **SD** were obtained over a broad spectra range by the open aperture Z-scan technique[167] and presented in Fig. 4.4C. The shape of these spectra is similar to known symmetrical squaraine derivatives with maximum linear absorption wavelengths at ~600-700 nm.[166, 168-170] The absolute cross section values up to ~4,000 GM were observed for symmetrical squaraine **SD** in the short wavelength two-photon allowed absorption range, and can be explained by the extremely high maximum extinction coefficient (molar absorptivity) of $2.82 \cdot 10^5$ $M^{-1}cm^{-1}$ (see Table 4.2) and due to pre-resonant enhancement.[171] In the long wavelength one-photon allowed spectral range, 2PA efficiency decreased dramatically due to the selection rules for electronic dipole transitions. The small maximum at ~1,100 nm can likely be attributed to an independent electronic state or vibronic coupling, resulting in corresponding changes in the selection rules and increased 2PA efficiency.

Table 4.2 Photophysical Properties Comparison of **SD** and PMAO-SD NPs

	λ_{abs}[a] [nm]	λ_{em}[a] [nm]	$\Delta\lambda$[b] [nm]	τ[c] [ns]	Φ_F[d]
SD	628	701	73	-	-
PMAO-SD NPs	651	671	20	2.09	0.10

[a] Absorption and emission maxima ±1 nm; [b] Stokes shift ±2 nm; [c] fluorescence lifetimes ±5%; [d] fluorescence quantum yield ±10%.

4.23 Nanoparticle Characterization

The ζ potential and number-weighted hydrodynamic sizes of the NPs were analyzed by dynamic light scattering (DLS). PMAO-SD nanoparticles have a considerable negative charge on the surface (-57.0 mV), due to the negatively charged carboxylate moieties formed by hydrolysis of cyclic anhydride groups in aqueous media (Table 4.3). The ζ potential of PMAO-SD NPs dispersed in water changed only slightly during the 5-day incubation at 37 °C.[154] After conjugation with a cyclic RGD-peptide, the NP size increased from 30 nm for PMAO-SD NPs to 38 nm for pre-RGD-PMAO-SD NPs, and further increased slightly to 40 nm for RGD-PMAO-SD NPs after the *n*-propylamine surface functionalization. A similar trend was observed for the ζ potential: RGD-PMAO-SD NPs exhibited a ζ potential of -6.9 mV supporting successful surface modification by *n*-propylamine. It is reasonable that the slightly negative charge emanates from unreacted carboxylic groups on NP surface.

Table 4.3 The Hydrodynamic Size and ζ Potential of Different Groups of Nanoparticles

Nanoparticle groups	Size [nm]	Potential [mV]
Group 1	30.44± 0.9	-57.00 ± 2.10
Group 2	38.02± 1.1	-34.9 ± 0.44
Group 3	40.13± 1.7	-6.93 ± 1.53

Group 1: PMAO-SD NPs; Group 2: pre-RGD-PMAO-SD NPs; Group 3: RGD-PMAO-SD NPs.

4.24 Cytotoxicity, One- and Two-photon Cell Imaging

Before employing the RGD-PMAO-SD NPs for cell imaging, their cytotoxicity was investigated with HeLa and U87MG cells (to provide diversity in cell type) using an MTS assay.[172,173] The concentration of RGD-PMAO-SD NPs solution was determined from its absorption at 651 nm (molar absorptivity of **SD**, $\varepsilon_{651\ nm} = 4.03 \times 10^5$ L·mol^{-1}·cm^{-1} in DCM). As shown in Figure S9, low cytotoxicity was obtained over a concentration range from 12.5 to 200.0 nM for RGD-PMAO-SD NPs, appropriate for cell imaging.

To enhance cell uptake and achieve target selectivity, the Arg-Gly-Asp (RGD) motif was selected as it is recognized by $\alpha_v\beta_3$ integrin, which is selectively expressed by neovasculature endothelial cells engaged in angiogenesis.[130, 174] Three comparison groups were performed to demonstrate the enhanced uptake and integrin-targeting specificity: bright fluorescence was displayed in a granular pattern associated with vesicles around perinuclear areas by cells incubated with RGD-PMAO-SD NPs (Fig. 4.5a, b, and c); low fluorescence was exhibited by cells incubated with free RGD prior to NP incubation, indicating saturation of $\alpha_v\beta_3$ binding sites reduced the uptake of RGD-conjugated NPs (Fig. 4.5d, e, and f); blurry fluorescence found mainly outside U87MG cells incubated with PMAO-SD NPs (lacking RGD-functionalization) demonstrates their poor biological compatibility and cell uptake (Fig. 4.5g, h, and i). Additionally, the MCF-7 cell line (Breast

Adenocarcinoma cells), which was reported as$\alpha_v\beta_3$ negative, was used as a negative control group for the study of RGD-PMAO-SD nanoparticles' selectivity. MCF-7 exhibited no noticeable fluorescence after 2 h incubation with RGD-PMAO-SD nanoparticles.
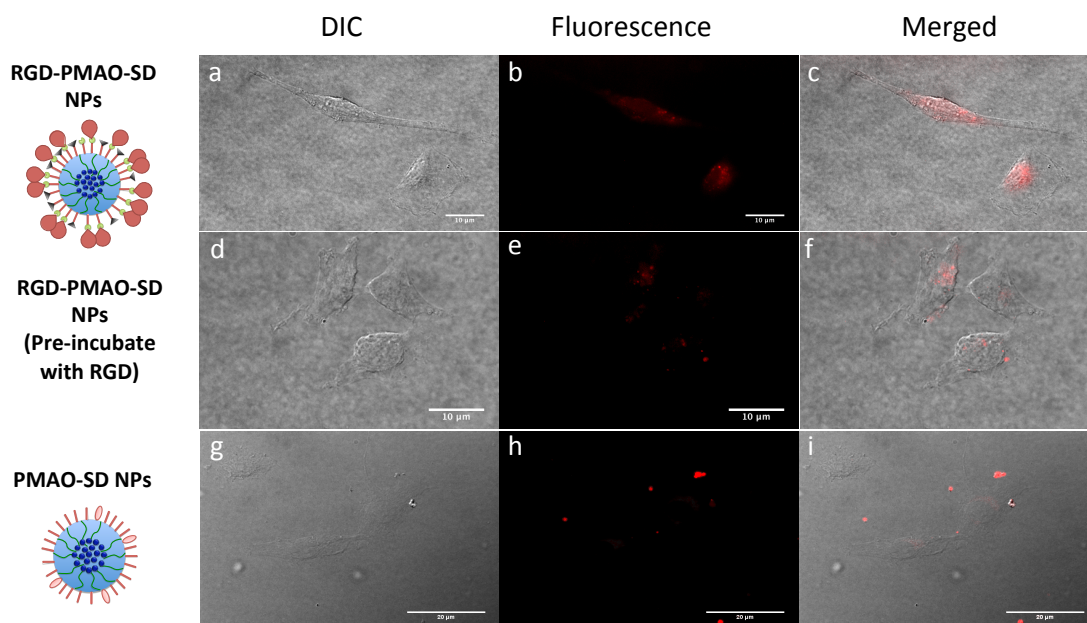
Figure 4.5 DIC (a, d, g), fluorescence (b, e, h), and overlay images (c, f, i) of U87MG cells incubated with RGD-PMAO-SD NPs (a, b, c), pre-incubated with RGD-peptide and then RGD-PMAO-SD NPs (d, e, f), and PMAO-SD NPs (c, f, i). Scale bars are 10 μm.

In advance two-photon fluorescence tumor imaging, 2PFM *in vitro* cell imaging was conducted firstly. As presented in Figure 4.6, U87MG cells (a cell line that expresses high levels of $\alpha_v\beta_3$ integrin) incubated with RGD-PMAO-SD nanoparticles exhibited bright fluorescence around perinuclear areas. The excitation wavelength employed in 2PFM imaging experiments was 820 nm, which is in the NIR window, facilitating deeper penetration compared with typical one-photon excitation in the visible range. This result, and low cytotoxicity, demonstrated that the RGD-PMAO-SD NP probe is a promising candidate for *in vivo* use tumor imaging.
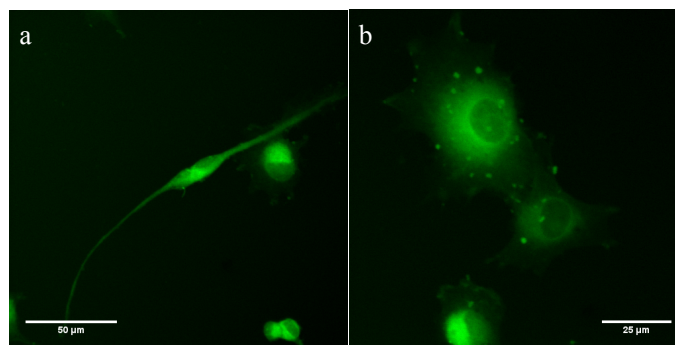
Figure 4.6 Two-photon images of U87MG cells after 2h incubation with RGD-PMAO-SD NPs, all taken with 20X, water immersion objective (NA=1.00, Olympus). Scale bars are: (a) 50 μm; and (b) 25 μm. 3D reconstruction from overlaid two-photon fluorescence images (76 MHz, 200 fs pulse width, Ex: 820 nm; Em: 624/40 nm).

4.25 2PFM Tumor Imaging

The in *vitro* one-photon fluorescence microscopy (1PFM) and 2PFM cell images indicated effective cell uptake and good integrin targeting for RGD-PMAO-SD NPs, providing motivation to investigate the NPs for tumor imaging. Lewis Lung Carcinoma (LLC) tumors were grown in mice as a xenograft model. After tail vein injection of the RGD-PMAO-SD NP probe and controls, LLC tumor tissues were excised from mice and fixed in 35 mm petri dishes. Bright fluorescence was collected from vessel endothelium illuminated by the fluorescence from the RGD-conjugated NPs, demonstrating their specific targeting (Figure 4.7a) and revealing clear vascular structure (Fig. 4.7b). The depth of observed fluorescence was around 150 μm. No significant fluorescence was detected for two negative control groups.
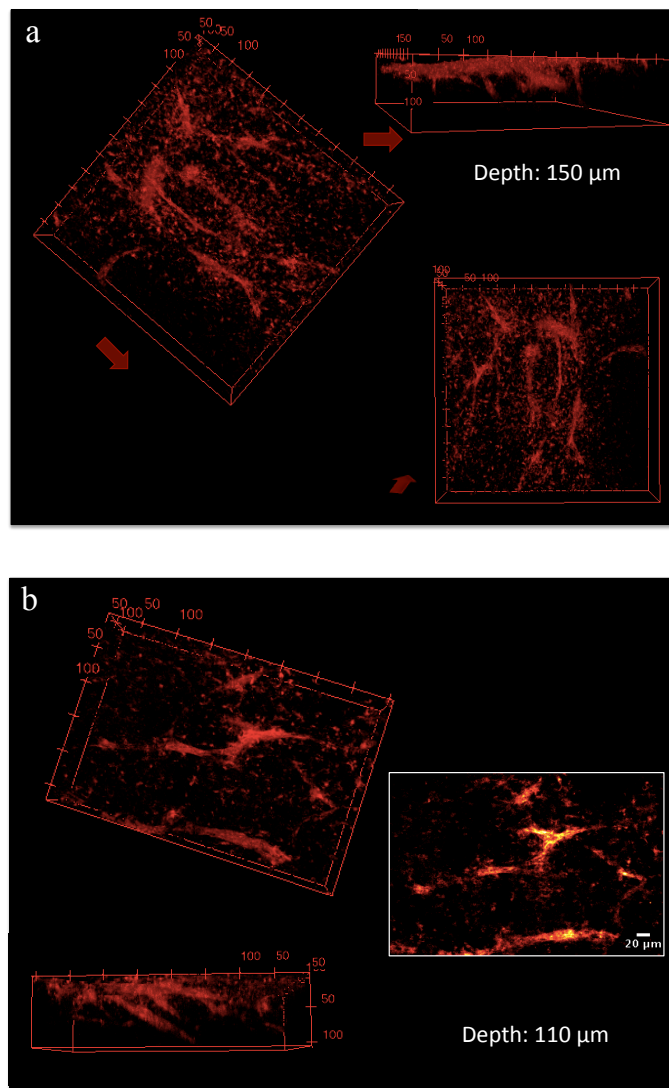
Figure 4.7 3D reconstruction images of the vasculature in the LLC tumor implants that were extracted from mice injected with RGD-PMAO-SD NPs, all taken with 20X, water immersion objective (NA=1.00, Olympus). 3D reconstruction from overlaid two-photon fluorescence images (76 MHz, 200 fs pulse width, Ex: 820 nm; Em: 624/40 nm).

4.3 Methods

4.31 Materials

The cyclic peptide (Ar-Gly-Asp-D-Phe-Lys) c(RGDfK) was purchased form Peptides International, Inc. All other chemicals reagents were purchased from Fisher Scientific or Sigma Aldrich, and used as received unless otherwise noted. The ^{1}H and ^{13}C NMR measurements were performed at room temperature using a 500 MHz Bruker Avance III

NMR spectrometer at 500 and 126 MHz, respectively. ^{1}H NMR spectra were referenced to TMS at δ=0.0 ppm while ^{13}C NMR spectra were referenced to CDCl$_3$ at δ=77.0 ppm. High-resolution mass spectrometry (HR-MS) analysis was performed with an Apex Ultra 70 Hybrid Fourier transform mass spectrometer (BrukerDaltonics) using ESI techniques in the Department of Chemistry, Rutgers University-Newark, Newark, NJ.

4.32 Synthesis of Compound B

Reagents and conditions for the synthesis of the squaraine probe are presented in Scheme 1. According to the previously published procedures, the key intermediate A was prepared by reacting phloroglucinol with bis(2-ethylhexyl)amine in a yield of 52%. Treatment of **A** with squaric acid provided the dye **B** as dark blue viscous oil in 24% yield. R$_f$≈0.67 (*n*-hexane/ethyl acetate, 9/1, v/v). ^{1}H NMR (CDCl$_3$, 500 MHz, ppm): δ 10.96 (s, 4 H, phenol-*H*), 5.81 (s, 4 H), 3.32-3.28 (m, 8 H), 1.85-1.81 (m, 4 H), 1.35-1.24 (m, 32 H), 0.92-0.88 (m, 24 H). ^{13}C NMR (CDCl$_3$, 126 MHz, ppm): δ 181.36, 162.50, 161.07, 158.27, 102.46, 94.46, 56.59, 38.12, 30.45, 28.50, 23.81, 23.09, 14.04, 10.63. HR-MS (*m/z*): [M+H]$^+$ Calculated for C$_{48}$H$_{77}$N$_2$O$_6$, 777.5776; Found, 777.5789.

4.33 Synthesis of Compound SD

Squaraine **B** (1 equiv.), potassium *tert*-butoxide (4 equiv.), and dry THF were placed in a round bottom flask, which was then flushed with N$_2$. Dimethylsulfate (2 equiv.) in THF was added and the solution was stirred at room temperature for 8 h. The resulting residue was concentrated, dissolved in DCM, washed with water, and then dried over anhydrous MgSO$_4$. After removal of the solvent *in vacuo*, the crude product was purified by column chromatography with *n*-hexane/ethyl acetate (4/1, v/v)) as eluent, affording the corresponding methyl-substituted squaraine dye. We noted that not only the desired compound could be separated in the one-pot reaction, other by-product derivatives could

be generated and their yields depended on the ratio of starting material **B**, dimethyl sulfate, and the base added to the reaction system. The overall yield of compound **SD** was in the range of 30% and result in green solid, $R_f \approx 0.57$ (*n*-hexane/ethyl acetate, 4/1, v/v). ^{1}H NMR (CDCl$_3$, 500 MHz, ppm): δ 13.98 (2 H, phenol-*H*), 5.83 (2 H), 5.67 (2 H), 3.91 (6 H, C*H*$_3$), 3.38-3.27 (8 H), 1.88-1.83 (4 H), 1.41-1.24 (32 H), 0.99-0.90 (24 H). ^{13}C NMR (CDCl$_3$, 126 MHz, ppm): δ 182.10, 171.71, 165.83, 163.02, 156.88, 103.42, 94.82, 88.60, 56.64, 55.45, 38.08, 30.64, 28.67, 23.94, 23.10, 14.04, 10.74. HR-MS (*m/z*): [M+H]$^+$ Calculated for C$_{50}$H$_{81}$N$_2$O$_6$, 805.6089; Found, 805.6078.

4.34 Preparation of the PMAO-SD Nanoparticles

The synthesis of the PMAO-SD NPs by a coprecipitation technique described by Lee *et al.* and presented in Figure 4.2 in the manuscript. Briefly, 20.0 mg PMAO and 0.1 mg **SD** was dissolved in 8.0 mL THF and mixed homogeneously by stirring for 1 h. The nanoparticle formation and dye encapsulation were accomplished simultaneously by coprecipitation through one-shot injection of 1.0 mL above mixed solution into 5.0 mL Milli-Q water under sonication. Subsequently, THF was removed under vacuum at 30 °C given an aqueous suspension containing squaraine-encapsulated PMAO nanoparticles (PMAO-SD NPs).

4.35 Synthesis of RGD-peptide Conjugated Nanoparticles

The NHS/EDC activation and RGD-peptide coupling reaction was based on published reports. To obtain the NHS-modified PMAO-SD NPs, the pH of 5.0 mL of NPs suspension was adjusted to 6.0 by MES buffer. Then, 1 mL mixture of 0.6 mg NHS and 1 mg EDC in PBS (phosphate-buffered saline) was added to the suspension by syringe pump at a rate of 1 mL/h. The solution was stirred for another 5 h under the protection of N$_2$, then the pH

was adjusted to 7.5 followed by the addition of 1 mL PBS containing 3 mg c(RGDfK) peptide. Subsequently, the mixture was incubated overnight at room temperature with gentle stirring under N_2. Finally, the unreacted NHS, EDC, and cyclic-RGD peptide were removed from the NPs by dialysis using a 3500 molecular weight cut-off dialysis cassette, and the resulting NPs suspension was filtered with a membrane filter (0.22 μm pore size).

4.36 Synthesis of RGD-PMAO-SD NPs

The NHS/EDC coupling reaction was repeated as described above to activate the remained carboxylic acid on the nanoparticle surface. Unreacted NHS-activated moieties of the pre-RGD-PMAO-SD NPs (5 mL solution containing 2 mg of PMAO NPs) were reacted with 0.15 mg n-propylamine and the mixture was gently stirred overnight under N_2. Unreacted NHS, EDC, and n-propylamine were removed from the NPs by dialysis using a 3500 molecular weight cut-off dialysis cassette, and the resulting nanoparticles suspension was filtered with a membrane filter (0.22 μm pore size).

4.37 Photophyscial Property Measurement and Nanoparticle Characterization

Absorbance and fluorescence spectra of **SD** were investigated in spectroscopic grade toluene (TOL), dichloromethane (DCM), acetonitrile (ACN), dimethyl sulfoxide (DMSO), tetrahydrofuran (THF) and PBS. Absorbance and fluorescence spectra of PMAO-SD NPs were measured in PBS. The steady-state absorption measurements were carried out using a Tecan Infinite® M200 PRO plate reader spectrometer in 10 mm path length quartz cuvettes. The fluorescence spectra were obtained using an Edinburgh Instruments FLS980 fluorescence spectrometer. The fluorescence spectra were corrected for the spectral responsivity of the PMT.

The fluorescence quantum yields were recorded and calculated by using crystal violet in methanol (Φ_F=0.55) as standard. The values were calculated according to equation (4.1):

$$\phi_{sample} = \phi_{ref} \cdot \frac{OD_{ref} I_{sample} n_{sample}^2}{OD_{sample} I_{ref} n_{ref}^2} \qquad (4.1)$$

where Φ is the quantum, I is integrated emission signal, OD is optical density at excitation wavelength, and n is the refractive index; subscript 'ref' stands for reference samples, 'sample' stands for samples.

The nominal concentration for each type of nanoparticles was calculated by the molar absorptivity based on the Beer-Lambert law.

Zeta potential measurements and particle size analysis by a light scattering method were performed using the Zetasizer Nano series (Malvern Instruments).

4.38 2PA Measurements

Degenerate 2PA spectra of **SD** was obtained with a femtosecond 1 kHz laser system (Ti:sapphire regenerative amplifier (Legend Duo+) pumping an optical parametric oscillator (OPO, HE-TOPAS) from Coherent, Inc.) using an open aperture Z-scan technique. All measurements were performed in 1 mm quartz cuvettes with dye concentrations $\sim 10^{-3}$ M. The experimental Z-scan setup was calibrated with ZnSe, CdSe, and SiO_2 as standards.

4.39 Cell Viability, One- and Two-Photon Fluorescence Imaging

To estimate the cytotoxicity of the RGD-PMAO-SD NP probe, U87MG and HeLa cells were cultured in Minimum essential medium supplemented with 10% fetal bovine serum and 1% penicillin and streptomycin at 37 °C and 5% CO_2. Cells were placed in 96 well plates and incubated until there were no fewer than 6×10^4 cells per well for the experiments. Next, U87MG and HeLa cells were incubated with different concentrations of RGD-PMAO-SD nanoparticles (12.5, 25.0, 100.0, 200.0, and 400.0 nM) for an additional 22 h. After that, 20 µL of CellTiter 96 Aqueous One solution reagent was added to each well followed by incubation for an additional 2. The respective absorbance values were recorded with a Tecan Infinite® M200 PRO plate reader/spectrometer at 490 nm to determine the relative amount of formazan produced. Cell viabilities were calculated based on following Equation (4.2):

$$Cell\ Viability\ (\%) = \frac{Abs_{490nm}^{S} - Abs_{490nm}^{D}}{Abs_{490nm}^{C} - Abs_{490nm}^{D2}} \times 100\% \tag{4.}$$

where Abs^{S}_{490nm} is the absorbance of the cells incubated with different concentrations of experimental solutions, Abs^{D}_{490nm} is the absorbance of cell-free well containing only dye at the concentration studied, Abs^{C}_{490nm} is the absorbance of cells only incubated in medium, and Abs^{D2}_{490nm} is the absorbance of the cell-free well.

To investigate the efficiency and specificity of RGD-PMAO-SD NPs, three control groups were employed in the experiment: U87MG cells incubated with (1) RGD-PMAO-SD NPs; (2) free RGD-peptide (saturation experiment) then with RGD-PMAO-SD NPs; (3) PMAO-SD NPs.

U87MG cells were placed onto poly-D-lysine coated coverslips placed in 24-well plates in the density of 5×10^4 cells per well and incubated for 48 h. Nanoparticles were

diluted to 200 nM from a stock solution and added to cells. After 1.5 h incubation, the NPs solution was removed and the coverslipped cells were washed abundantly with PBS (2×). Then, cells were fixed with 3.7% formaldehyde solution in PBS for 10 min. The fixing agent was removed and washed (2×) with PBS. A fresh solution of $NaBH_4$ (1mg/mL) in PBS was used to treat the fixed cells for 10 min (2×) to reduce the autofluorescence. The coverslipped cells were then washed with PBS (2×) and deionized water then mounted on microscope slides using the antifade mounting media (Prolong Gold).

Conventional single-photon fluorescence (1PFM) cell images were obtained on an inverted microscope (Olympus IX70) equipped with a QImaging cooled CCD and a 100 W mercury lamp. The TexRed filter cube (Ex: 562/40; DM: 593; Em: 624/40) was used to match the excitation wavelength of NPs and to capture most of its emission profile. 2PFM imaging was performed using a Bruker Ultima fluorescence microscopy system equipped with a Coherent Mira 900F laser source (76 MHz, mode-locked, 200 fs pulse width). Cells were excited at 820 nm and the emission was collected using an external non-descanned PMT detector (NDD) (Em: 624/40 nm). A 20x, 1.0 N.A. water immersion objective was employed for the 2PFM imaging. 3D reconstruction and statistical analysis of scanned images was performed with the Fiji software.

For the two-photon fluorescence tissue imaging, images were recorded with a Bruker Ultima fluorescence microscopy system equipped with a Coherent Mira 900F laser source (76 MHz, mode-locked, 200 fs pulse width). The fs laser excitation was tuned to 820 nm in order to achieve cellular-level imaging of tumors. The tumors dissected from mice were cut from the edge, where the angiogenesis occurred, and imaged. Images acquired were then analyzed with Fiji software for 3D reconstruction.

4.4 Conclusion

We developed a general method to prepare peptide-functionalized amphiphilic polymer NPs, encapsulating a squaraine dye with high 2PA, to form a biocompatible probe to enable 2PFM tumor neovasculature imaging. We also reported that a novel squaraine derivative, **SD**, exhibits advantageous photophysical properties in a number of organic solvents while fluorescence quenching was observed in aqueous media similar to other squaraine analogs. However, after PMAO encapsulation, the fluorescence quantum increased over 100-fold to 0.10, supporting successful embedding of **SD** in the hydrophobic domain of the polymer NP assembly, protecting the dye from aggregation and fluorescence quenching. Further modification of the PMAO-SD NP, including conjugation with a cyclic RGD-containing peptide and *n*-propylamine improved cell uptake and realized effective $\alpha_v\beta_3$ integrin targeting in both cell culture and *in vivo*. *Ex vivo* 2PFM imaging of LLC tumor tissue allowed visualization of tumor microvasculature up to 150 μm in depth, a limitation imposed by the small size of the tissue rather than the probe or 2PFM technique. The dye-encapsulating PMAO NPs conjugated with functional targeting groups will provide a versatile pathway to develop fluorescent probes for a number of important biological-imaging applications. This approach capitalizes on the ability to encapsulate hydrophobic fluorescent dyes that would not normally be used in aqueous media.

CHAPTER 5

FAR-RED-EMITTING TEG-SUBSTITUTED SQUARAINE DYE: SYNTHESIS, OPTICAL PROPERTIES, AND SELECTIVE DETECTION OF CYANIDE IN AQUEOUS

A comprehensive study of the photophysical properties of triethylene glycol monomethyl ether (TEG)-substituted squaraine dye SQ**1** is presented. SQ**1** exhibits strong absorption and intense fluorescence emission in the far-red spectral region and high photostability. Interestingly, bis-tegylated SQ**1** was characterized to exhibit properties different from its tetrahydroxy analog (SQ**2**), to which we ascribe attenuation of intermolecular interactions as a result of steric hindrance through introduction of two TEG chains adjacent to the squaraine core. The photophysical properties of SQ**1** were also investigated asa function of temperature and pH. In cetyltrimethylammonium bromide (CTAB) micellar media (1.0 mM), the fluorescence quantum yield of SQ**1** increased dramatically to 0.22, compared with 0.02 in water. Based on this discovery, SQ**1** was found to display excellent sensitivity and selectivity to the presence of cyanide ions (CN^-), with a limit of detection of 1.7 μM. The hypothesized CN^- sensing mechanism was probed, and visual test strips were developed. This work broadens the family of squaraine dyes and demonstrates SQ**1** for use as a fluorescent or visual sensing probe.

5.1 Introduction

Squaraine dyes are well-known fluorophores with long wavelength absorption, large molar absorptivity, high fluorescence quantum yields, and high photostability.[175, 176] Their unique photophysical properties make them promising candidates in a variety of scientific and technological applications such as organic electronics,[177-179] optical data storage,[180-182]

chemosensing,[183-185] nonlinear optics,[186,187] photodynamic therapy of cancer,[188-190] and fluorescence probes.[191-193] Squaraine dyes can be considered as neutral molecules with a resonance-stabilized zwitterionic structure and the planar donor–acceptor–donor (D–A–D) type of electronic distribution with a strong tendency to aggregate in aqueous solution and the solid state, often causing fluorescence quenching that severely limits their practical applications.[194-196] Meanwhile, squaraine dyes demonstrate a wide range of optical properties strongly dependent on structural modification,[197,198] molecular symmetry,[192,199] and micelle-related microenvironment.[200-201] In this regard, the synthesis of novel squaraine derivatives and the investigation of their optical properties are subjects of intense interest for important applications.

Detection of anions in biological systems and the environment within specified concentration ranges in a timely manner is central to determining compliance with federal and state regulations regulating commercial chemical and biological processes.[202,203] The cyanide anion (CN^-) is known to be extremely toxic because of its propensity to bind to the active site of cytochrome oxidase, which eventually inhibits electron transport in mitochondria.[204,205] Exposure to higher concentrations of gaseous HCN (> 300 ppm) within a few minutes will cause human death by depressing the central nervous system.[206] The U.S. Environmental Protection Agency (EPA) has set a CN^- limit of 0.2 ppm (7.69 μM) in drinking water.[207] Although previous reports detail a wide variety of chemical and physical sensors for the detection of CN^-, a number of known chemosensors suffer from some disadvantages, such as complex and environmentally compromised organic synthesis, water insolubility, poor photostability, high detection limits, or deleterious interference from other anions.[206] From a practical perspective, it is still a challenge to develop CN^-

sensors with high selectivity and sensitivity.[208-211] There have been ongoing efforts to develop a rapid, reliable and economical technique for on-site determination of CN⁻. Certain squaraine dyes have been reported to selectively react with nucleophiles such as thiols and cyanides

In this study, we report the synthesis and comprehensive characterization of the linear spectroscopic and photochemical properties of a novel TEG-substituted squaraine derivative SQ**1**. Linear photophysical investigations include a detailed analysis of the nature of absorption bands by excitation anisotropy,[218] along with fluorescence lifetime and quantum yield measurements. The tetrahydroxy analog SQ**2** served as a control. The results show that modification by two TEG groups close to the squaraine core can alter intra- and intermolecular interactions aimed to prevent aggregation and increase water solubility. Meanwhile, SQ**1** was developed as a sensitive and selective fluorescent sensor for the detection of CN⁻ in DMSO and CTAB micellar solution. Upon the addition of trace CN⁻, the characteristic blue solution of SQ**1** turned colorless immediately. SQ**1** was also further developed to be a visual sensor toward CN– as a paper test strip.

5.2 Results and Discussion

5.21 Synthetic Route and Photophysical Properties

The synthesis of SQ**1** is illustrated in Figure 5.1, starting from piperidinylcarbamate **A** through esterification, forming the triethyleneoxy ester, followed by deprotection and condensation with phloroglucinol to produce **C**. Tegylation of one of the phenolic groups of **C** followed by condensation with squaric acid resulted in bis(hydroxy) SQ**1**. SQ**2** was prepared in an analogous manner, as detailed in the Supporting Information. The main

linear spectroscopic characteristics and photochemical parameters of SQ**1** are presented in Figure 5.2 and Table 5.1. SQ**1** is readily soluble in organic solvents, yielding a blue solution with a sharp absorption band located in the far-red spectral region as well as intense fluorescence emission. For instance, in DMSO, the absorption maximum at 652 nm ($\varepsilon = 1.95 \times 10^5$ M^{-1} cm^{-1}) is independent of concentration.
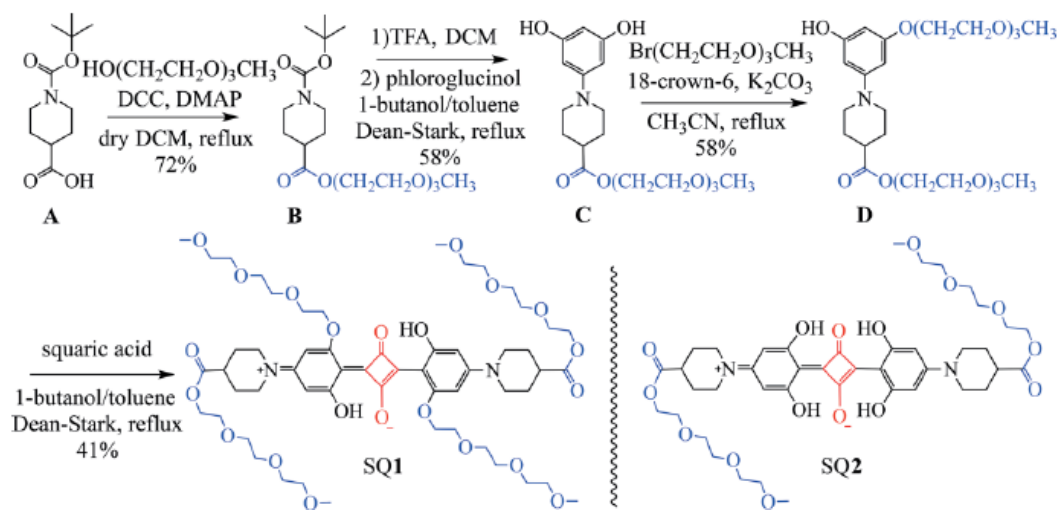
Figure 5.1 Synthetic route for SQ1 and chemical structure of SQ2.

Table 5.1 Main Photophysical and Photochemical Parameters of SQ1

Solvents	λ_{abs}	$\varepsilon \times 10^{-5}$	λ_{em}	$\Delta\lambda$	τ_F	Φ_F	$\Phi_{ph} \times 10^7$
TOL	643	2.22	661	18	0.86	0.21	0.11
DCM	643	2.04	664	21	0.75	0.23	0.40
THF	641	2.14	661	20	0.79	0.19	0.25
MeOH	639	2.22	664	25	0.43	0.13	1.6
CAN	638	2.20	666	28	0.41	0.12	1.3
DMSO	652	1.95	678	26	0.86	0.28	10.8
H₂O	645	1.20	674	29	0.15	0.02	6.74
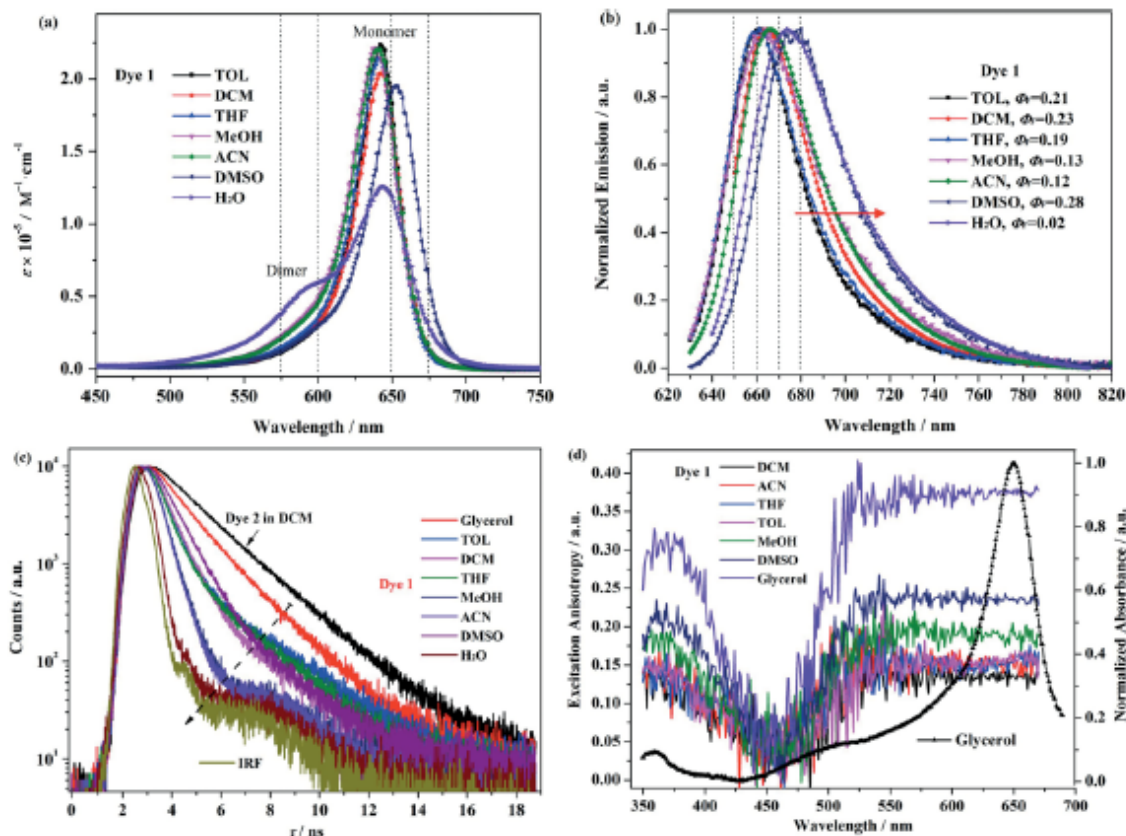
Figure 5.2 Photophysical properties. Absorption spectra (a), normalized fluorescence emission spectra (b), fluorescence lifetime kinetics (c), and excitation anisotropy (d) of SQ**1** in different solvents. The black curve (triangles) overlapping the excitation anisotropy in (d) shows the absorption spectrum of SQ**1** in glycerol. TOL: toluene, DCM: dichloromethane, THF: tetrahydrofuran, MeOH: methanol, ACN: acetonitrile, and DMSO: dimethyl sulfoxide.

The steady-state fluorescence spectra of SQ**1** exhibit a small Stokes shift (ca. 26 nm) and are independent of excitation wave-length over the entire absorption band (cf. Figure 5.3). These values are typical for squaraine dyes in monomeric form.[219] The Stokes shifts, in good agreement with the Lippert equation,[190, 220] show an approximately linear dependence on the solvent orientation polarizability (cf. Figure 5.4). The relatively large fluorescence solvatochromism suggests the presence of specific solute–solvent interaction

and that SQ**1** is weakly polar in the ground state but acquires large polarity upon photoexcitation.
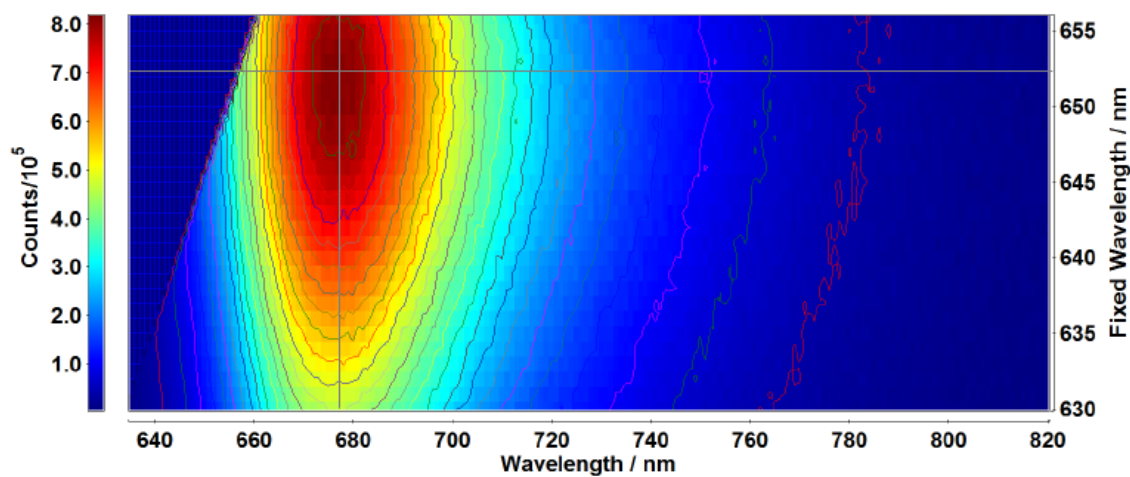
Figure 5.3 Synchronous spectra map of dye SQ1 in DMSO.
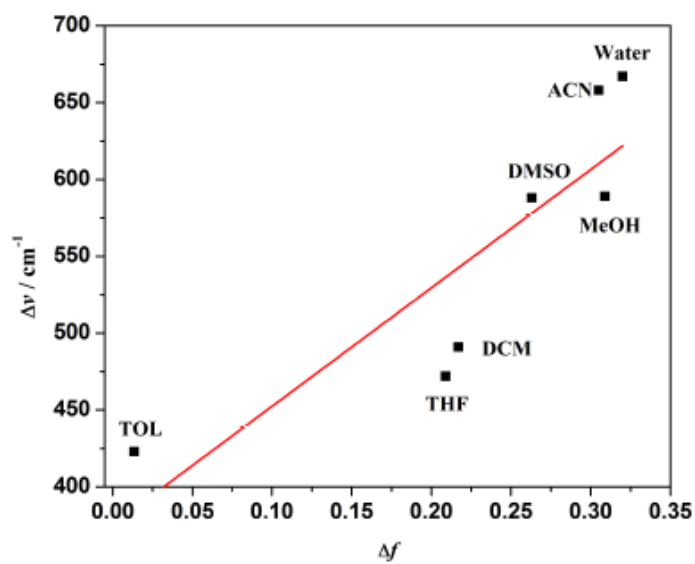
Figure 5.4 Solvatochromism of SQ1 in different solvents.

As discussed above, SQ**1** exhibits a decreasing trend in Φ_F with increasing solvent polarity, which can be explained by the solvent effect on intra- and intermolecular energy transfer. In the polar aprotic solvent DMSO, the Φ_F increased to 0.28 compared with $\Phi_F =$ 0.02 in water. Fluorescence emission decay kinetics of SQ**1** correspond to a single-exponential decay in MeOH, ACN, DMSO, and water with τ_F in the range 0.15–0.86 ns, while a double-exponential process was observed in TOL, DCM, and THF. Because of the unique electronic distribution of the four-membered squaraine core and limited optical studies on the modified dihydroxyphenyl-based squaraines, the relationship between fluorescence properties and environmental effects of squaraine dyes remains elusive. As a control, SQ**2** in DCM exhibits a nearly identical absorption maximum at 646 nm and strong fluorescence emission, with a maximum at 664 nm. Its fluorescence quantum yield is relatively high (0.68 in DCM, cf. Figure 5.5).
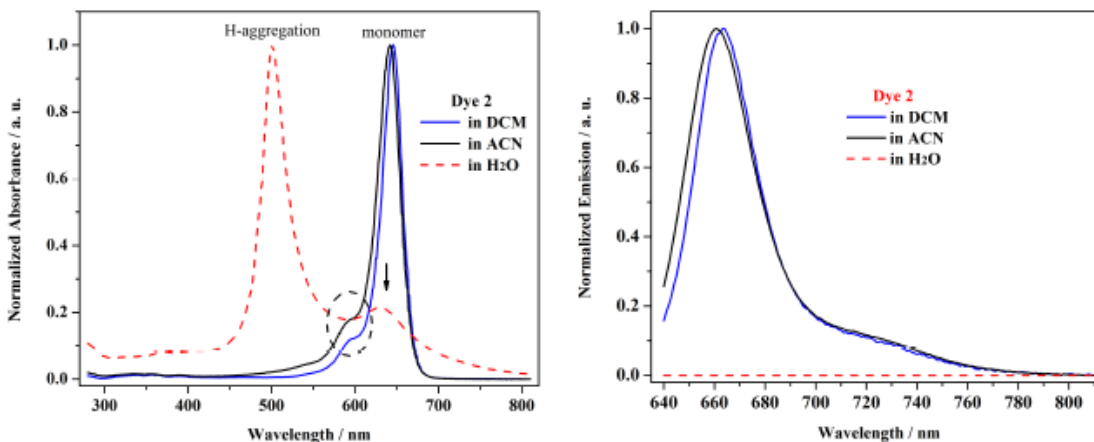
Figure 5.5 Normalized absorption and fluorescence emission spectra of dye SQ**2** in DCM, ACN, and water

Excitation anisotropy spectra provide information regarding the nature of linear absorption bands. The excitation anisotropy plots of SQ**1** in organic solvents and in viscous glycerol are presented in Figure 1d. The values of excitation anisotropy are nearly constant in the main absorption band. This reflects the electronic transition S_0–S_1 with similar dipole orientations, corresponding to the main absorption band.[221] From the functional anisotropy value $r0 = (3\cos2\alpha - 1)/5$, the angle α between absorption S_0–S_1 and emission $S1$–$S0$ transition dipole moments can be calculated. In glycerol, the excitation anisotropy reaches its maximum value $r \approx r0 \approx 0.37$, which is close to the theoretical limit 0.4, reflecting a nearly parallel orientation of the absorption and emission transition dipoles. At higher energy, the anisotropy decreases, and a dip is observed near 460 nm with $r \approx 0.05$, ascribed to an electronic transition whose absorption transition dipole moment creates an angle $\alpha \approx 50°$ with respect to the emission transition dipole moment. The curves shown in the short-wavelength range of the excitation anisotropy spectrum suggest the existence of more than one electronic excited state with mutual orientation of the corresponding electronic transitions S_0–S_n (= 1, 2, 3, ...) of SQ**1**.[222]

In low-viscosity solvents, the anisotropy values (r) decrease due to rotational movement of the molecule. The rotational correlation times (θ) and effective rotational molecular volumes (V) of SQ**1** were determined for each solvent, and the corresponding parameters η, τ_F, θ, and V are presented in Tables 5.1 and 5.2 for solvents of different polarity. According to this data, the effective rotational molecular volume V decreases with Δf, providing evidence of decreased solute–solvent interactions in polar media, where a much smaller number of solvent molecules are involved in the rotational moment of SQ**1**.

The effect of weak solute–solvent interactions in polar media can also be related the observed high quantum yield in DMSO, mentioned above.

Table 5.2 The Excitation Anisotropy of SQ1

	TOL	THF	DCM	DMSO	CAN	MeOH
r (λabs)	0.154	0.152	0.136	0.234	0.149	0.188
η /cp	0.56	0.46	0.41	2	0.37	0.54
θ /ns	0.61	0.55	0.43	1.45	0.27	0.44
V /A^3	4473	4930	4285	3018	3044	3347
Δf[a]	0.0135	0.209	0.217	0.263	0.305	0.309

The excitation anisotropy value r at λ_{abs}, the solvent viscosity η, the rotational correlation time θ, and the effective rotational molecular volume V of SQ**1** in solvents of different polarity (orientation polarizability Δf); [a] Polarity (orientation polarizability) $\Delta f = [(\varepsilon - 1)/(2\varepsilon + 1)] - [(n^2 - 1)/ (2n^2 + 1)]$; ε and n are the dielectric constant and refractive index of the solvent, respectively.

5.22 Photochemical Stability and Thermal Stability of SQ1

The photochemical stability of SQ**1** was investigated at room temperature in order to evaluate its potential for practical use. It should be emphasized that quantitative determination of photostability as Φ_{ph} is a molecular parameter, in contrast to relative kinetic absorption/emission photochemical measurements that are highly dependent on specific experimental conditions.[223,224] As shown in Table 5.1, the highest level of photostability of SQ**1** was observed in TOL solution and is at least two orders of magnitude higher in comparison to those of the best laser dyes.[225,226] The values of Φ_{ph} noticeably increase in solvents of high polarity but still remain in the range of practical utility. The photostability data indicates that this dye holds substantial promise as a probe in sensing and bioimaging applications.

Temperature effects, measured in DMSO solution, show that the fluorescence intensity, fluorescence lifetimes, and fluorescence quantum yields decrease with increasing temperature (cf. Figures 5.6). Correspondingly, the nonradiative decay rate (k_{nr}) increases with increasing temperature, while the radiative decay rate (k_r) remains approximately constant.
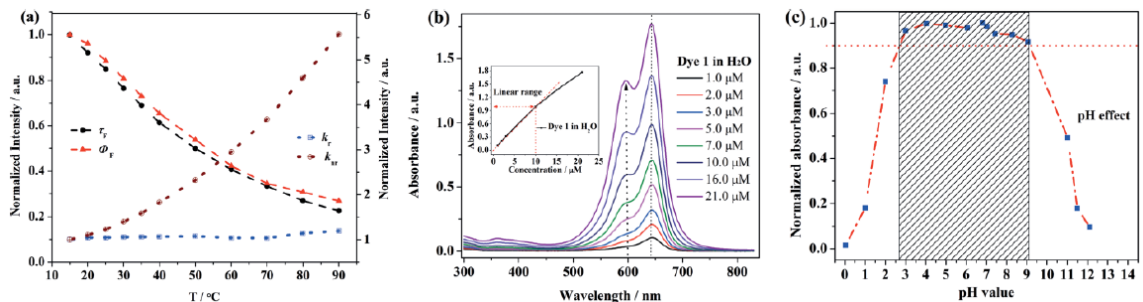
Figure 5.6 Temperature effects to SQ1. (a) Fluorescence lifetimes (τ_F), fluorescence quantum yields (Φ_F), nonradiative (k_{nr}) and radiative (k_r) decay constants for SQ**1** recorded as a function of temperature in DMSO. (b) Concentration-dependent absorption spectrum of SQ**1** in water. The inset shows the linear relation of absorption as a function of concentration. (c) The effect of pH on the optical properties of SQ**1** in aqueous solution.

5.23 SQ1 Sensing Ability Study

In order to evaluate the possible use of SQ**1** as a sensing fluorophore in aqueous solution, the influence of pH on the optical properties was determined (Figure 5.6). The absorption intensity of SQ**1** at 645 nm was unaffected in the pH range from 3.0 to 9.0. Interestingly, in acidic media (pH below 3.0, cf. Figure 5.7), a significant decrease of the main absorption, a new blueshifted band centered at 500 nm, and a clear isosbestic point around 550 nm were observed. The fluorescence was recovered by increasing the pH of the solution back to 7.0. Under basic conditions (pH above 9.0, cf. Figure 5.7), the main absorbance band decreased in intensity, and a short absorption band at 350 nm occurred, corresponding to the addition of OH to the squaraine core, in agreement with previously

published reports.[214,227] Some SQ dyes show high sensitivity towards solvent polarity, the surrounding microenvironment, and the presence of certain proteins or antibodies.[228-230] It can be seen in Figure 5.1 and Table 5.1 that SQ**1** shows sharp and strong emission in TOL (661 nm, Φ_F = 0.21) and DMSO (678 nm, Φ_F = 0.28), while exhibiting much weaker emission in water (Φ_F = 0.02). Such behavior is considered to be advantageous for the measurement of fluorescence differences in a more hydrophobic environment (e.g. micelles) relative to hydrophilic surroundings. For this reason, we examined the optical properties in aqueous solution before and after the addition of cetyltrimethylammonium bromide (CTAB; the critical micelle concentration, CMC, is about 1.0 mM).[231-233] As shown in Figure 5.8a, the addition of CTAB resulted in an increase of the sharp absorption band at 645 nm and the fluorescence intensity (about 13-fold) at 667 nm. This phenomenon is attributed to a local hydrophobic domain induced by the presence of CTAB. An encouraging result is that the fluorescence quantum yield of SQ**1** in CTAB micellar media (0.22) increased relative to that in pure water (0.02). However, a fluorescence quenching effect was detected when the dye concentration exceeded 3.4 µM (cf. Figure 5.8b and 5.9). This quenching effect is most likely due to the formation nonemissive dimers.
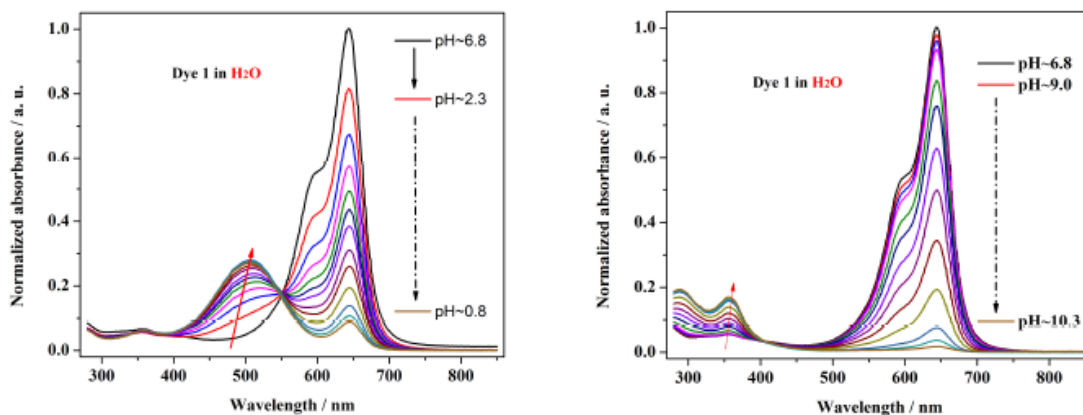
Figure 5.7 Fluorescence emission spectra of dye SQ**1** recorded in different pH ranges.
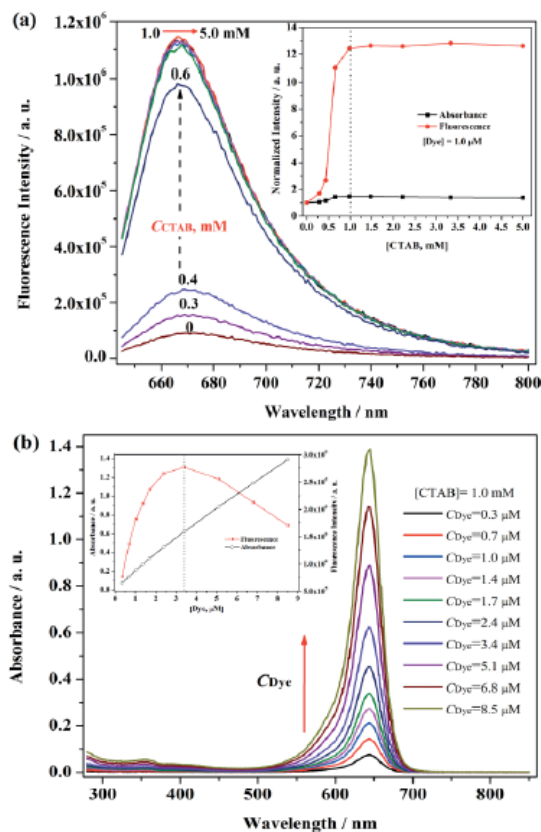
Figure 5.8 Fluorescence and absorption intensity changes of SQ1 at different CTAB concentration. (a) Fluorescence intensity changes of SQ**1** at different CTAB concentrations. The inset shows the absorbance and fluorescence emission intensity changes vs. the CTAB concentration. (b) Absorption spectra of SQ**1** upon increasing the concentration in 1.0 mM CTAB micellar media. The inset shows the absorbance and fluorescence emission intensity changes vs. the dye concentration.
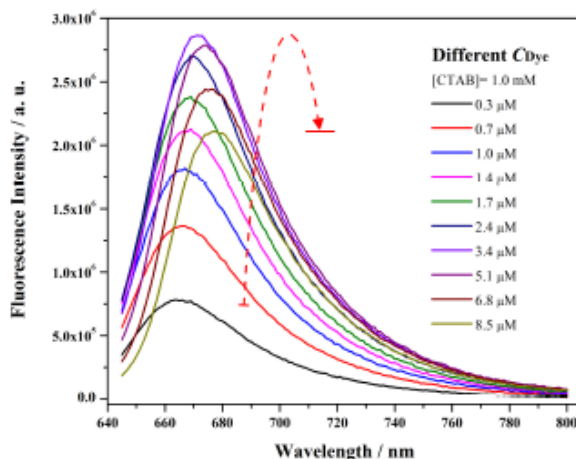
Figure 5.9 Fluorescence emission changes of dye SQ **1** at different concentrations in CTAB micellar media (1.0 mM).

CN⁻ is a reasonably strong nucleophile and very toxic, thus, fast and reliable methods to detect it in water, food, packages, and the environment are of paramount importance. Hence, the sensing properties of SQ**1** towards CN⁻ were first explored in DMSO, because of the relatively high fluorescence quantum yield of SQ**1** in DMSO. The addition of CN– resulted in a sharp decrease in the absorbance and fluorescence intensity of SQ1 (cf Figure 5.10). Thus, it appeared that this novel compound may be promising as a highly fluorescent sensor for CN⁻, although it would be more valuable to determine its sensitivity and selectivity in aqueous solution. To do so, experiments were conducted in CTAB micellar media using both absorbance and fluorescence methods, as SQ**1** itself is not very soluble in water. As shown in Figure 5.10, the fluorescence intensity (667 nm) decreases gradually with increasing CN⁻ concentration and is almost completely quenched after the addition of 70 equiv. CN⁻, accompanied by a color change from dark blue to colorless, which is readily detectable by the naked eye. Figure 4b presents the linear correlation between the ratio $I/I0$ and [CN⁻] in the range from 0 to 50.0 μM ($R_2 = 0.9925$). Furthermore, the detection limit for CN⁻ was calculated to be approximately 1.7 μM,[234,235] which is below the World Health Organization's (WHO) guideline value of 1.9 μM in drinking water and the maximum contaminant level for CN⁻ in drinking water set by the US EPA.
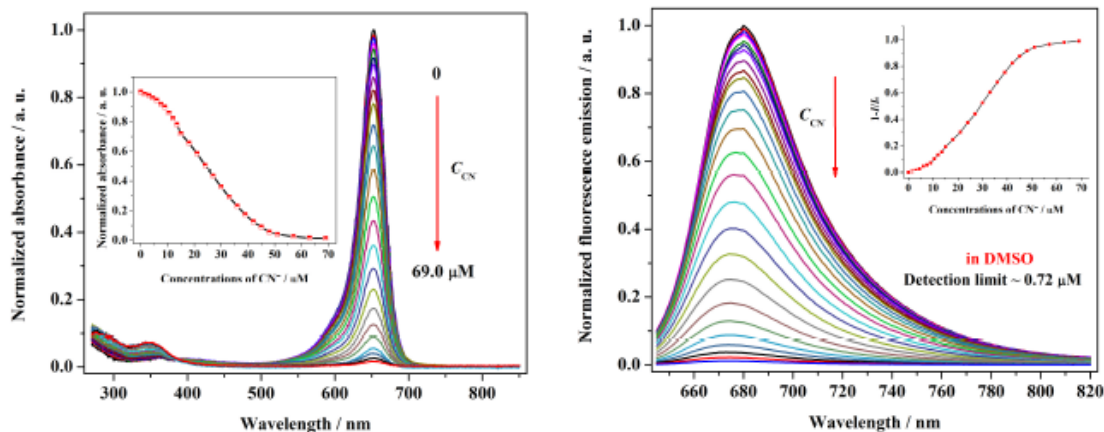
Figure 5.10 Normalized absorption (left) and fluorescence spectra (right) recorded for dye **SQ1** at different CN- concentration in DMSO (the concentration of **SQ1** is 2.0 μM).

The selectivity of **SQ1** toward CN^- was further assessed in a quantitative manner. As shown in Figure 5.10c, competing anions, such as F^-, Cl^-, Br^-, I^-, OH^-, N_3^-, HCO_3^-, Ac^-, ClO_4^-, NO_2^- and SO_4^{2-}, did not interfere in the detection of CN^-. These results demonstrated the high selectivity of **SQ1** toward CN^-. **SQ1** indicated a rapid response to CN^-, completing the reaction within several minutes, which is beneficial for real-time, in-field detection. Photos of solutions of **SQ1** in CTAB with different CN^- concentrations can be observed in Figure 5.11. Figure 5.11d demonstrates the chromatic change from blue to colorless at high concentrations of CN^- (100 to 1000 μM). An obvious change is noted when the $[CN^-]$ is above 200 μM, while at lower concentrations (10 to 100 μM), changes can also be easily seen by the naked eye as the blue solution becomes lighter or undergoes bleaching (Figure 5.11e). Thus, it is possible to estimate the $[CN^-]$ by comparing the color of the sample with those of standard solutions or, more precisely, through spectroscopic recording and comparison to standards with the help of a calibration curve.
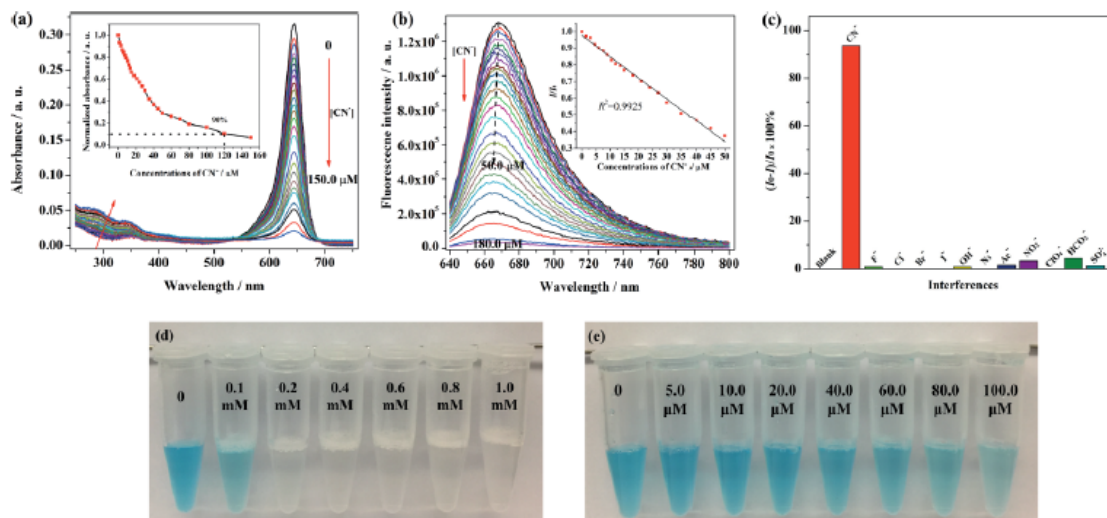
Figure 5.11 Absorption (a) and fluorescence intensity (b) changes of SQ**1** (2.0 μM) in response to varying CN⁻ concentrations in 1.0 mM CTAB micellar media. Inset: normalized intensity changes upon adding CN⁻. (c) Anion selectivity of the dye SQ**1** in 1.0 mM CTAB micellar media. (d) Different solution colors of SQ**1** (40.0 μM) in CTAB micelle media containing higher levels of CN⁻ (10 min). From left to right: 0, 0.1, 0.2, 0.4, 0.6, 0.8, 1.0 mM. (e) Different solution colors of SQ**1** (40.0 μM) in CTAB micelle media containing lower levels of CN–. From left to right: 0, 5.0, 10.0, 20.0, 40.0, 60.0, 80.0, 100.0 μM (10 min).

5.24 The Study of Interaction between SQ1 and CN⁻

To understand the interaction of SQ**1** with CN⁻, 1H NMR spectra were recorded in the absence and presence of NaCN in [D6]DMSO, and the results are shown in Figure 5.12. It can be seen that, upon addition of CN⁻, the peak of the phenol hydrogen in SQ**1** is shifted upfield and separated into two resonances, appearing at about 8.6 and 7.3 ppm. The process is supposed to involve nucleophilic attack of CN⁻ on the cyclobutene double bond of the squaraine core to yield the adduct in the middle of Figure 5.12, a hypothesis that is also confirmed by the MALDITOF MS results (cf. Figure 5.13).[212,227,238] This addition results in reducing the conjugation of the chromophore to generate a new non-fluorescent compound, which explains the rapid color change (bleaching).
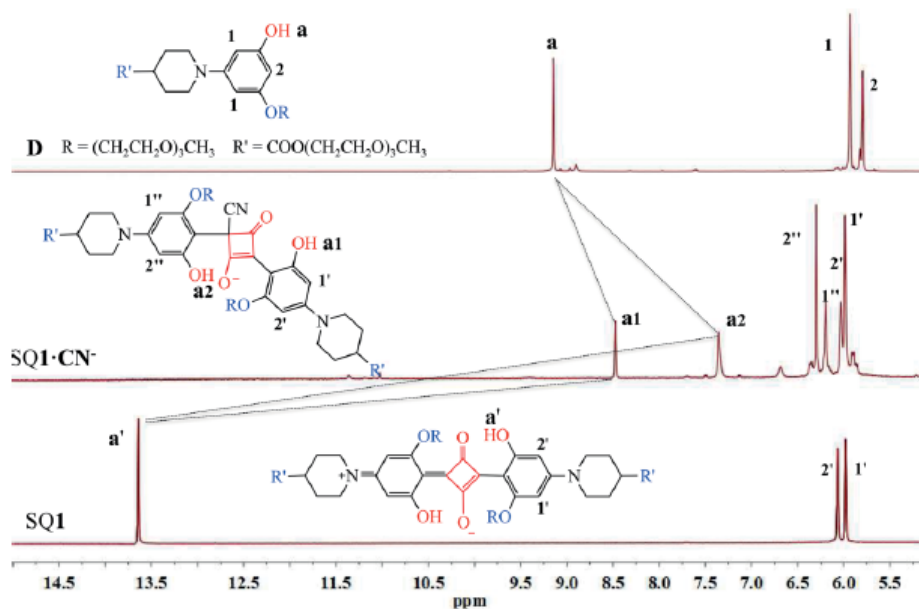
Figure 5.12 Partial ^{1}H NMR spectra of SQ1 in [D6]DMSO in the absence (bottom) and presence (middle) of CN$^-$ and intermediate **D** (top) as a control. The structures of the related compounds and the adduct **1·CN** are shown in the insets.
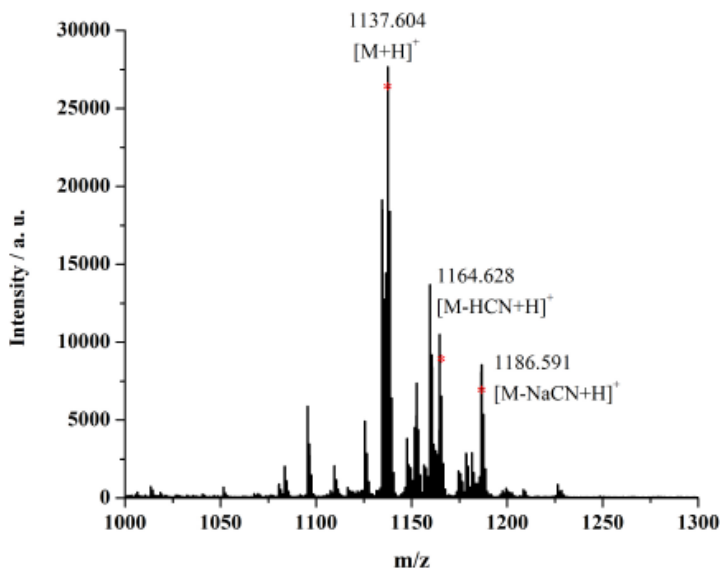
Figure 5.13 MALDI-TOF mass spectrum of the dye **SQ1** in the presence of NaCN.

5.25 The Development of Cyanide Chemosensors

With the aim of developing new cyanide chemosensors for on-site (in-field) detection, we prepared test strips following the procedures illustrated in Figure 5.14a. Briefly, SQ**1** was dissolved in DCM, then 1.0 mM CTAB solution was added, and the mixture was stirred overnight to evaporate the organic solvent.

Subsequently, a drop of the mixture was placed onto filter paper inside a glass dish. The filter paper was left to dry in air and cut into small pieces, producing test strips. It is worth mentioning that the dye concentration in CTAB solution was optimized in an effort to obtain the most extensive visual Subsequently, a drop of the mixture was placed onto filter paper inside a glass dish. The filter paper was left to dry in air and cut into small pieces, producing test strips. It is worth mentioning that the dye concentration in CTAB solution was optimized in an effort to obtain the most extensive visual changes in color of the test strips from blue to colorless for CN^- sensing. It was found that the strips exhibit excellent selectivity for CN^- as compared to that of the negative control samples (other anions or blank). As a result, the sensor strips have promising potential for on-site visual detection of CN^- pollution in water.
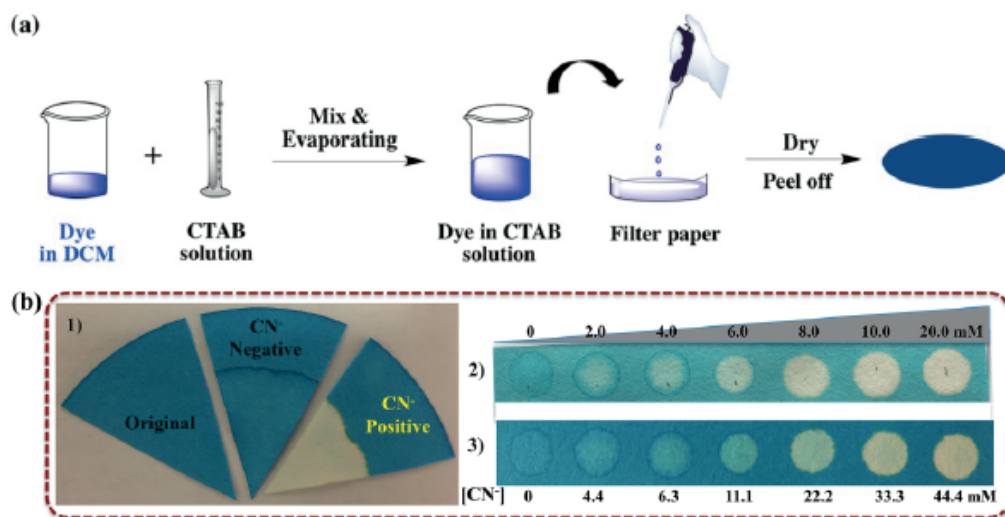
Figure 5.14 (a) Schematic diagram showing the processes of fabrication of test strips for CN⁻ sensing. (b) Color changes of the test strips after interactions with solutions containing different concentrations of CN⁻.

5.3 Experimental Section

5.31 Experimental Details

Briefly, SQ**1** was prepared from the condensation of electron-rich **D** with squaric acid using a Dean–Stark apparatus, where the water that formed was removed continuously.[240] Intermediate **B** was synthesized from **A** and triethylene glycol monomethyl ether based on the Steglich esterification reaction.[241,242] Then **C** was obtained using trifluoroacetic acid (TFA) to remove the *tert*butyloxycarbonyl protecting group in **B**, followed by the general reaction of phloroglucinol with the resultant secondary amine through its *keto* tautomer in 1-butanol/toluene mixture under reflux. By treatment with 1-(2-bromoethoxy)-2-(2-methoxyethoxy)- ethane by nucleophilic substitution under basic condition, **C** was converted into **D**. Moreover, the tetrahydroxy analog SQ**2** was synthesized under the same reaction conditions as those used for SQ**1** 1H and 13C NMR spectroscopy and MALDI-

TOF mass spectroscopy confirmed the chemical structures and purities of the related compounds.

All reagent chemicals and solvents were used as purchased without further purification unless otherwise noted. Suitable water was obtained using a Direct-Q water purification system. The anions are in the form of sodium or potassium salts. Thin-layer chromatography (TLC) was performed on precoated silica gel 60 F254 plates. Column chromatography was performed over silica gel 230-400 mesh. The 1H and ^{13}C NMR measurements were performed at room temperature by a Bruker Avance III NMR spectrometer at 500 and 126 MHz, respectively. ^{1}H NMR spectra were referenced to TMS at δ=0.0 ppm while 13C NMR spectra were referenced to CDCl3 at δ=77.0 ppm and DMSO-d6 at δ=39.5 ppm. Mass spectrometry (MALDI-TOF-MS) analysis was performed on an Ultraflex Xtreme MALDI-TOF/TOF mass spectrometer (Bruker Daltonics, Germany in positive model at the Department of Chemistry, Rutgers University-Newark, Newark, NJ. The Boc-protection of piperidine-4-carboxylic acid (**A**)[1-2] and synthesis of 1-(2-bromoethoxy)-2-(2-methoxyethoxy)ethane were performed based on the previously reported literatures, and the resulting 1H NMR spectra matched the reported data.

5.32 Synthesis of Compound B

Compound **A** (5.0 g, 21.8 mmol) and dry dichloromethane (DCM, 150 mL) were added to a 250 mL round-bottomed flask equipped with a magnetic stirring bar and a reflux condenser. Dicyclohexylcarbodiimide (4.5 g, 21.8 mmol, DCC), triethylene glycol monomethyl ether (3.8 g, 22.9 mmol), and 4-dimethylaminopyridine (0.54 g, 4.4 mmol, DMAP) were added to the solution. The reaction mixture was heated to refluxing for 12 h under N2 atmosphere, filtered, and the filtrate was concentrated under reduced pressure.

The crude mixture was purified by column chromatography (1/1, v/v, *n*-hexane/ethyl acetate on silica, R_f=0.30) to afford **B** as a colorless oil (5.9 g, 72%). ^{1}H NMR (500 MHz, CDCl$_3$) δ: 4.24 (td, *J*=4.7, 1.1 Hz, 2 H), 4.01 (d, *J*=13.4 Hz, 2 H), 3.70 (td, *J*=4.6, 1.1 Hz, 2 H), 3.67–3.61 (m, 6 H), 3.55 (ddd, *J*=5.7, 3.7, 1.1 Hz, 2 H), 3.38 (s, 3 H), 2.84 (t, *J*=12.1 Hz, 2 H), 2.54–2.44 (m, 1 H), 1.94–1.82 (m, 2 H), 1.69–1.59 (m, 2 H), 1.45 (d, *J*=1.2 Hz, 9 H). ^{13}C NMR (126 MHz, CDCl$_3$) δ: 174.38, 154.58, 79.42, 71.89, 70.58, 70.53, 69.05, 63.54, 58.95, 40.94, 28.38, 27.91.

5.33 Synthesis of Compound C

Compound **B** (5.0 g, 13.3 mmol) was dissolved in dry DCM and cooled to 0 °C. Trifluoroacetic acid (TFA) was added and the solution was allowed to warm to room temperature. After stirring until starting material was consumed (TLC monitoring), the solution was poured into water, neutralized with NaOH solution, and extracted with DCM. The combined organic layer was dried over MgSO$_4$, filtered and concentrated to give a colorless oil in quantitative yield that was used immediately in the next step. Phloroglucinol (1.7 g, 13.3 mmol), 1- butanol (40 mL) and toluene (80 mL) were added and heated at reflux with a Dean-Stark apparatus for 8 h. During that time, the solution progressed from colorless to pale red. Excess solvent was removed under reduced pressure, which left a reddish oil that was purified by column chromatography (10/1, v/v, DCM/methanol on silica, R_f=0.34), affording **C** as a colorless oil (3.0 g, 58%). ^{1}H NMR (500 MHz, CDCl$_3$) δ: 5.92 (dd, *J*=6.9, 1.9 Hz, 3 H), 4.27–4.19 (m, 2 H), 3.78–3.60 (m, 8 H), 3.59–3.53 (m, 2 H), 3.43 (dt, *J*=12.5, 4.0 Hz, 2 H), 3.37 (s, 3 H), 2.63 (td, *J*=12.3, 2.9 Hz, 2 H), 2.45–2.31 (m, 1 H), 1.89 (dd, *J*=13.6, 3.8 Hz, 2 H), 1.82–1.68 (m, 2 H). ^{13}C NMR (126 MHz, CDCl$_3$) δ: 175.21, 157.98, 153.38, 96.41, 95.13, 71.92, 70.51, 69.28, 63.66, 58.97, 53.46, 50.75,

48.90, 40.79, 27.55. MALDI-TOF-MS (m/z): $[M+H]^+$ Calculated for $C_{19}H_{30}NO_7$, 384.2017; Found, 384.202.

5.34 Synthesis of Compound D

Compound **C** (1.7 g, 4.4 mmol), 1-(2-bromoethoxy)-2-(2-methoxyethoxy)ethane (1.0 g, 4.4 mmol), 18-crown-6 (0.12 g, 0.44 mmol) and K_2CO_3 (0.61 g, 4.4 mmol) were refluxed in dry CH_3CN (50 mL). After 12 h, the solution was cooled to room temperature and concentrated before water was added. The aqueous solution was extracted three times by DCM. The combined organic phase was dried over anhydrous Na2SO4, concentrated in vacuum, and purified by column chromatography on silica (13/1, v/v, DCM/methanol on silica, R_f=0.52), affording **D** as a colorless oil (1.4 g, 58%). ^1H NMR (500 MHz, DMSO-d6) δ: 9.14 (s, 1 H), 5.93 (s, 2 H), 5.81 (s, 1 H), 4.16 (2 H), 3.97 (2 H), 3.69 (2 H), 3.61 (2 H), 3.57–3.48 (m, 14 H), 3.43 (d, J=2.9 Hz, 4 H), 3.24 (s, 6 H), 2.73 (t, J=11.9 Hz, 2 H), 1.87 (d, J=11.8 Hz, 2 H), 1.62 (dd, J=21.1, 10.5 Hz, 2 H). ^{13}C NMR (126 MHz, DMSO-d6) δ: 174.71, 160.67, 159.32, 153.21, 96.27, 94.34, 93.17, 71.74, 70.39, 70.27, 70.21, 70.08, 69.49, 68.76, 67.20, 63.68, 58.51, 48.28, 28.02. MALDI-TOF-MS (m/z): $[M+H]^+$ Calculated for $C_{26}H_{44}NO_{10}$, 530.2960; Found, 530.296.

5.35 Synthesis of SQ1

In a 100 mL round bottom flask, compound **D** (1.1 g, 2.0 mmol) and squaric acid (0.11 g, 1.0 mmol) dissolved in a 1-butanol/toluene mixture (100 mL, 1/1, v/v) were added. The resulting mixture was heated at reflux with a Dean-Stark apparatus for 2 h to generate a dark green solution. After the solvent was distilled, the reaction mixture was cooled to room temperature. The crude mixture was purified by column chromatography (10/1, v/v, DCM/methanol on silica, R_f=0.48) to afford SQ**1** as a green solid (0.47 g, 41%). ^1H NMR

(500 MHz, CDCl$_3$) δ: 14.11 (s, 2 H), 5.90 (s, 2 H), 5.78 (s, 2 H), 4.26 (t, J=4.2 Hz, 4 H), 4.18 (t, J=4.8 Hz, 4 H), 4.05 (t, J=4.8 Hz, 4 H), 3.89 (d, J=13.5, 4 H), 3.78-3.63 (m, 28 H), 3.57-3.51 (m, 8 H), 3.37 (s, 12 H), 3.15 (4 H), 2.67 (2 H), 2.02 (4 H), 1.82 (4 H). ^{13}C NMR (126 MHz, CDCl$_3$) δ: 173.82, 166.60, 162.81, 157.74, 104.47, 95.12, 89.48, 71.86, 71.84, 70.65, 70.57, 70.52, 70.49, 70.31, 69.02, 69.00, 68,46, 63.72, 59.00, 58.95, 46.50, 40.44, 27.61. MALDI-TOF-MS (m/z): [M+H]$^+$ Calculated for C$_{56}$H$_{85}$N$_2$O$_{10}$, 1137.5588; Found, 1137.596.

5.36 Synthesis of SQ2

A 100 mL round bottom flask, charged with compound **C** (3.8 g, 10.0 mmol) and squaric acid (0.57 g, 5.0 mmol) dissolved in a 1- butanol/toluene mixture (100 mL, 1/1, v/v). The resulting mixture was heated at reflux with a Dean-Stark apparatus for 8 h to generate a dark green solution. The reaction mixture was cooled to room temperature and excess solvent was removed under reduced pressure. The crude mixture was purified by column chromatography (10/1, v/v, DCM/methanol on silica, R_f=0.55) to afford SQ**2** as a blue solid (2.7 g, 64%). 1H NMR (500 MHz, CDCl3) δ: 10.90 (s, 4 H), 5.88 (s, 4 H), 4.30–4.21 (m, 4 H), 3.94–3.83 (m, 4 H), 3.75–3.61 (m, 16 H), 3.61–3.51 (m, 4 H), 3.38 (s, 6 H), 3.15 (ddd, J=13.7, 10.7, 3.0 Hz, 4 H), 2.67 (tt, J=10.2, 4.3 Hz, 2 H), 2.07–1.96 (m, 4 H), 1.87–1.73 (m, 4 H). ^{13}C NMR (126 MHz, CDCl$_3$) δ: 181.16, 173.78, 163.32, 162.05, 158.58, 103.03, 94.30, 71.95, 70.64, 70.59, 70.57, 69.06, 63.81, 59.06, 46.48, 40.41, 27.77. MALDI-TOF-MS (m/z): [M+H]$^+$ Calculated for C42H57N2O16, 845.3703; Found, 844.362.

5.37 Photophysical and Photochemical Measurements

The optical properties of the dyes were investigated in spectroscopic- grade solvents: toluene (TOL), tetrahydrofuran (THF), dichloromethane (DCM), methanol (MeOH), acetonitrile (ACN), and dimethyl sulfoxide (DMSO), which were purchased from commercial suppliers and used without further purification. UV/Vis spectra were recorded using a Tecan InfiniteR M200 PRO spectrometer in a 10 mm path length quartz cuvette. The steady-state fluorescence spectra and excitation anisotropy spectra were recorded with an Edinburgh Instruments FLS980 fluorescence spectrometer at a dye concentration of $C \approx 10^{-6}$ mol L^{-1}. The spectral responsivity values of the photomultiplier tube (PMT) detectors were corrected using correction files provided by Edinburgh Instruments. Fluorescence lifetimes (τ_F) were determined with the single-photon-counting technique (TCSPC) using a pulsed picosecond diode laser (EPL-635) as the excitation source. It should be mentioned that under the employed experimental conditions the maximum optical density of the investigated solutions did not exceed 0.1 and reabsorption effects were negligible.

Fluorescence quantum yield (Φ_F) measurements were performed by a standard procedure using cresyl violet ($\Phi_F = 0.54$ in MeOH) as the reference.[243] Temperature effects were studied using a Quantum Northwest TC 125 temperature controller. All the other absorption and emission measurements were obtained at about 20 °C. The fundamental excitation anisotropy spectrum (r_0) of SQ **1** was obtained in viscous glycerol, where depolarization effects related to molecular rotational motion are negligible (i.e., the molecular rotational correlation time, $\theta = \eta V/kT\ \tau_F$, where η, V, k, and T are the solvent viscosity, effective rotational molecular volume, Boltzmann's constant, and absolute

temperature, respectively). In this case, the observed experimental value of the anisotropy, $r = r_0/(1 + \tau_F/\theta)$, was close to r_0. The excitation anisotropy spectra of SQ **1** were also determined in low-viscosity solvents in order to analyze the influence of the solvent on the rotational movement of the solute.

5.4 Conclusion

In summary, comprehensive photophysical and anion-sensing studies of a novel SQ dye, SQ**1**, were performed in a number of solvents at room temperature. The steady-state fluorescence spectra of SQ**1** were independent of excitation wavelength, exhibiting small Stokes shifts and obvious solvatochromic behavior. The photostability of SQ**1** was found to be higher than those of the more stable organic laser dyes by quantitative determination of photodecomposition quantum yield. Significantly, SQ**1** did not aggregate in polar solvents such as DMSO or aqueous mixtures, primarily due to the introduction of TEG chains close to the squaraine core. Encapsulation of SQ**1** in CTAB micelles resulted in reasonably high fluorescence quantum yield relative to that just in water. In addition, a novel fluorescent sensing strategy using SQ**1** in CTAB micellar media was developed for the sensitive and selective detection of CN^- with a detection limit of 1.7 μM, corresponding nicely to limits established by the WHO and the US EPA. Common, potentially interfering, anions exhibited no effect on absorption or fluorescence emission spectra of SQ**1**, demonstrating its high selectivity towards CN^-. The detection results can be readily observed by the naked eye, leading to development of visual test strips that are potentially useful for in-field sensing. The probable sensing mechanism was bolstered by ^{1}H NMR spectroscopic and mass spectroscopic results: it involves a nucleophilic attack of the CN^-

110

to the cyclobutene double bond of the squaraine core, resulting in drastic reduction of chromophore conjugation and concomitant color change. It is important to remember that the results evidence an enhancement of the fluorescence quantum yield due to dye encapsulation in the hydrophobic environment. This work provides valuable information on the photophysical properties of SQ**1**, which is useful for the development of bright and stable squaraine dyes for optical applications and use as sensing probes.

CHAPTER 6

STUDY OF NOVEL NIR SQUARAINE DYE CONTAINING ADMANTYL GROUPS: J-AGGREGATION DISSOCIATION AND ITS APPLICATIONS IN CELL IMAGING

Squaraine dyes **AM-1'** and **AM-1** bearing adamantyl termini were synthesized and spectroscopically characterized. **AM-1'** exhibited intense absorption and sharp emission in the far-red to near-infrared (NIR) spectral region in various organic solvents. Fluorescence quantum yields decreased with increasing solvent polarity, with concomitant changes in fluorescence lifetimes, which reflects the rapid decay of the excited state in solvents with higher polarity. The degenerate two-photon absorption (2PA) spectrum of **AM-1'** was obtained over a broad spectral range with a maximum cross section of ~360 GM. In aqueous solutions, **AM-1'** displayed a strong tendency for J-aggregation with a red-shifted absorption centered at 760 nm and fluorescence emission at 820 nm. The dihydroxyaniline-based analog **AM-1** was also studied as a reference and exhibited entirely different aggregation behavior. We conclude that both the terminal pendant groups and substitutents adjacent to the squaraine core play important roles in determining the aggregation behaviors and optical properties of the resultant squaraine dyes. Further an **AM-1'/β-**cyclodextrin (**AM-1'$\subset \beta$-CD**) complex, based on guest-host interactions, dramatically suppressed squaraine π-π stacking and dissociated the J-aggregate. The inclusion complex **AM-1'$\subset \beta$-CD** exhibited strong fluorescence emission centered at 670 nm and low but observable fluorescence (quantum yield, Φ_F, of 0.04) in aqueous media. Fluorescence microscopy imaging of HCT 116 cells incubated with the **AM-1'$\subset \beta$-CD** complex was

accomplished, suggesting the potential application of this complex in fluorescence bioimaging.

6.1 Introduction

As a class of organic dyes, squaraine derivatives exhibit sharp and intense absorption ($\varepsilon_{max} > 10^5$ M$^{-1}\cdot$cm^{-1}) and fluorescence emission which can be tailored from far-red to near-infrared spectral region.[244-248] In recent years, squaraine dyes have been investigated for applications such as nonlinear optics,[249,250] fluorescence microscopy bioimaging,[251-253] and photosensitizers for photodynamic cancer therapy.[254-257] In general, squaraines have the tendency to form H-/J-aggregation in aqueous media and the solid state, which may restrict their optical applications to some extent due strong quenching of the fluorescence emission.[258-261] Meanwhile, a number of design strategies have been explored to understand the relationship between their molecular structures and optical properties.[262-264] As investigated by Chen *et al.*, squaraine dyes with different side chains and different numbers of OH groups exhibit substantially different aggregation behavior in solid film states, which results in dramatically different molecular orientations and photophysical properties.[262] Previously, we reported several squaraine dyes with relatively large two-photon absorption cross-sections and high photostability that could be potential candidates for multiphoton fluorescence imaging.[253,265]

Environmental effects on the optical properties of squaraine dyes should be carefully considered, such as solvent polarity and H-bonding interactions.[266-268] Recently, Kalliat and co-workers encapsulated the phloroglucinol-based squaraine dyes in the cavity of β-cyclodextrin (β-CD) moieties, as a result, the fluorescence intensity as well as lifetime of squaraine dyes in aqueous solution were obviously enhanced, indicating their effective

interaction and a decrease in nonradiative decay processes.[269] Smith and co-workers described supramolecular encapsulation strategies to increase the chemical stability of squaraine dyes, inhibit aggregation-induced broadening of its absorption spectrum, and further develop their applications in cell imaging.[260,270] Inspired by this strategy, we designed a novel squaraine dye **AM-1'** containing adamantyl as terminal groups and triethylene glycol monomethyl ether (TEG) as side chains. In particular, TEG groups introduced close to the squaraine core serve several purposes, including as solubilizing groups, and most importantly, as a source of steric hindrance to increase the twisting of the π-system, such distortion of the rigid framework by steric bulk should induce slipped stacking arrangements with unique optical properties.[271,272] The optical properties of **AM-1'** in various organic solvents and its J-aggregation behavior in aqueous media was investigated.

Strong guest-host interactions between **AM-1'** and β-CD appeared to suppress J-aggregation and restore the fluorescence emission. The investigations reported herein are significant for gathering more information about microenvironment effects on the optical properties of squaraines. Finally, the inclusion complex **AM-1'** $\subset$ **β-CD** were further applied to one- and two-photon based fluorescence cell imaging. The excitation wavelength occurred nicely in the near-infrared (NIR) window that can provide deep penetration in biological samples. Meanwhile, the dihydroxyaniline-based squaraine analog **AM-1** was prepared and studied as a reference to provide information about the relationship between the squaraine molecular structure and photophysical properties.

6.2 Results and Discussion

6.21 Synthesis

The structure and synthetic details of **AM-1'** and **AM-1** are illustrated in Figure 6.1. This type of squaraine dye is usually prepared by the condensation between squaric acid and electron-rich aromatic, heteroaromatic, or olefinic compounds in a one-pot reaction.[273,274] Briefly, intermediate **B** was synthesized from reacting compound **A** with 1-adamantanemethanol based on the Steglich esterification reaction (Figure 6.1). Then compound **C** was obtained using trifluoroacetic acid (TFA) to remove the *tert*-butyloxycarbonyl protecting group in **B**, followed by the general reaction of phloroglucinol with the resultant secondary amine through its *keto* tautomer in 1-butanol/toluene mixture at reflux temperature. By nucleophilic substitution with 1-(2-bromoethoxy)-2-(2-methoxyethoxy)ethane under basic conditions, compound **C** was converted into **D**. The symmetrical target dye **AM-1'** was then obtained from the condensation of electron-rich **D** with squaric acid using a Dean-Stark apparatus. Moreover, **AM-1** was synthesized under similar reaction conditions by condensation of **C** and squaric acid.[249] ^{1}H NMR, ^{13}C NMR, and MALDI-TOF mass spectroscopy confirmed the molecular structures and purities of the related compounds.

The ^{1}H NMR spectra provides obvious insight into the structural difference among the electron distribution in dyes **AM-1'** and **AM-1**. As one can see, the phenol-OH in **AM-1'** shifted downfield to δ 14.12 ppm in comparison with **AM-1** at δ 10.94 ppm (c.f. Figure 6.2). The remaining aromatic protons in the **AM-1'** moiety split to two peaks around δ 5.91 and 5.79 ppm. These results are suggestive of a decrease in the conjugation of **AM-1'** due to the torsional strain in the molecule after TEG modification.
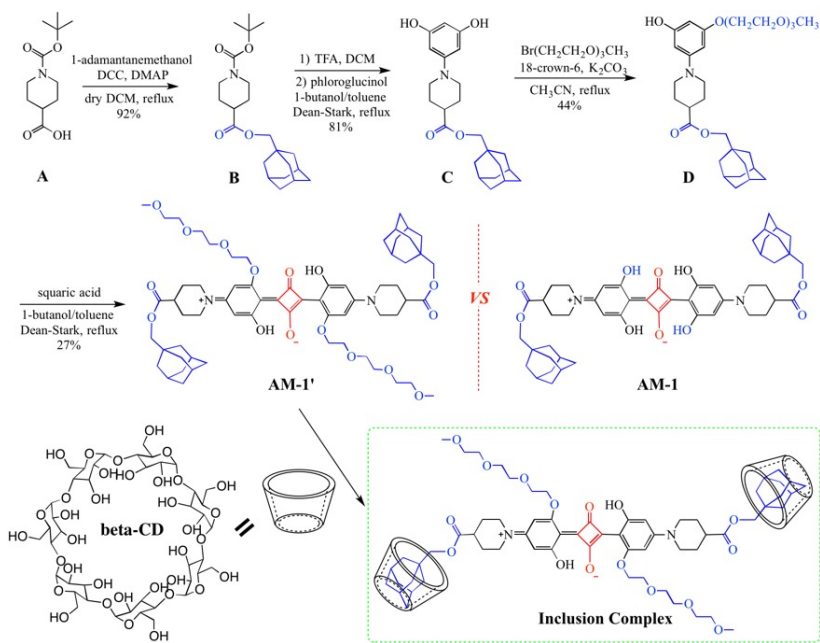
Figure 6.1 The synthesis route for dye **AM-1'**, schematic of formation of the inclusion complex **AM-1' ⊂ β-CD** based on the strong non-covalent interaction, and chemical structure of **AM-1**.
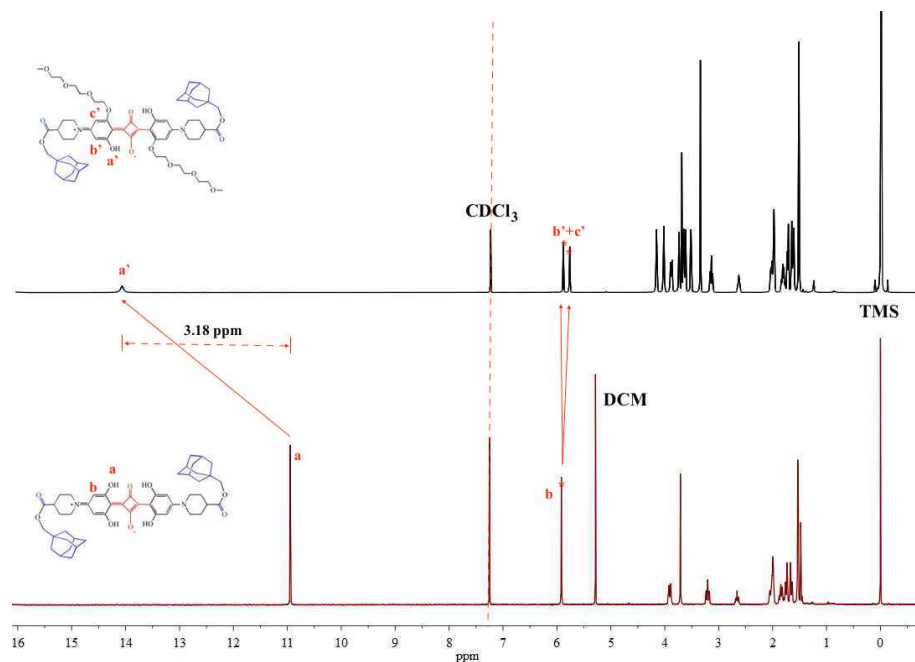
Figure 6.2 ^{1}H NMR spectra overlap of **AM-1'** and **AM-1** in CDCl$_3$.

6.22 Photophysical Properties of Dyes AM-1' and AM-1

Squaraine **AM-1'** exhibited good solubility in common organic solvents, yielding a typical blue solution with sharp absorption maximum as well as intense fluorescence emission located in the far-red spectral region. The linear spectroscopic characteristics and photochemical parameters of **AM-1'** and **AM-1** are presented in Figure 6.3 and Table 6.1. Their maximum extinction coefficients (ε_{max}) were as high as 2.0×10^5 $M^{-1} \cdot cm^{-1}$. The main linear absorption features for **AM-1'** were narrow absorption centered at 641 nm in tetrahydrofuran (THF) and 639 nm in methanol (MeOH), known to be caused by a π-π^* transition.[252,261] The steady-state fluorescence spectra exhibited small Stokes shifts and were independent of excitation wavelength over the entire absorption band (Figure 6.4). In various solvent with different polarities, similar absorption and emission spectra were exhibited, which indicate the very comparable molecular configurations of the dye in the ground states and excited states. **AM-1'** showed decreasing trends in fluorescence lifetimes (τ_F) and fluorescence quantum yields (Φ_F) with increased solvent polarity, as non-radiative decay processes dominate under these conditions.

In polar aprotic solvent such as MeOH, **AM-1'** showed slightly blue-shifted maximum absorption, red-shifted emission and low τ_F and Φ_F values. We may conclude that the ability of forming hydrogen bonding between squaraine molecules and MeOH prevents certain flexibility in the molecular framework. Moreover, the existence of hydrogen bonding can also increase the twist angle (torsional strain) and distort the co-planarity of the donor-acceptor-donor structure, thereby resulting in reduced τ_F and Φ_F values.[276] It has been proposed that the major non-radiative decay of the excited-state squaraine chromophore is caused by the rotation of the C-C bond between the phenyl ring

and the four-membered core unit. As the twist angle increases, non-radiative deactivation increased.[275,276] In comparison, **AM-1** in THF exhibited identical absorption maximum at 646 nm and strong fluorescence emission centered at 660 nm with Φ_F equal to 0.47 (Figure 6.3a and Table 6.2). The 5 nm blue-shift of the maximum absorption, absence of vibronic band around 600 nm, and relatively low Φ_F values for **AM-1'** indicates the effect of TEG groups on the photophysical properties of hydroxyaniline-based squaraine dyes.

Excitation anisotropy spectra provided information regarding the nature of linear absorption bands.[276] Evident in Figure 1c, values of excitation anisotropy for AM-1' in ploytetrahydrofuran (*p*THF) were nearly constant in the main absorption band, which reflects the S_0-S_1 electronic transition with similar dipole orientations. Based on the functional anisotropy value $r_0=(3\cos^2\alpha-1)/5$, we calculated the angle α between absorption and emission transition dipole moments. In *p*THF, excitation anisotropy reached its maximum value $r\approx r_0\approx 0.35$, which is close to the theoretical limit of 0.4, reflecting a nearly parallel orientation of the absorption and the emission transition dipoles (α~16 °). At higher energy, the anisotropy decreased and a dip was observed near 470 nm with r~0.10, which can be ascribed to an electronic transition whose absorption transition dipole moment has an angle of α~45 ° with respect to the emission transition dipole moment. Curves shown in the excitation anisotropy spectrum in short-wavelength region suggests the existence of more than one mutual orientations of the corresponding electronic transitions S_0-S_n (=1,2,3, ...) for **AM-1'**.

The degenerate 2PA spectra of **AM-1'** were obtained over a broad spectral range by the open aperture Z-scan technique and presented in Figure 6.3c. The shape of the spectrum is similar to than for symmetrical squaraine derivatives with maximum linear

absorption wavelengths at ~600-700 nm.[278,279] The absolute 2PA cross section values up to ~360 GM Were observed for symmetrical squaraine **AM-1'** in the short wavelength two-photon allowed absorption range, which can be explained by an extremely high maximum extinction coefficient ~2×10^5 $M^{-1}\cdot cm^{-1}$ (see Table 6.1) and close to double resonance excitation conditions.[280] In the long wavelength, one-photon allowed spectral range, 2PA efficiency decreased dramatically consistent with the selection rules for electronic dipole transitions. The small maximum at ~1100 nm can be attributed to vibronic coupling, resulting in corresponding changes in the selection rules and increased 2PA efficiency.
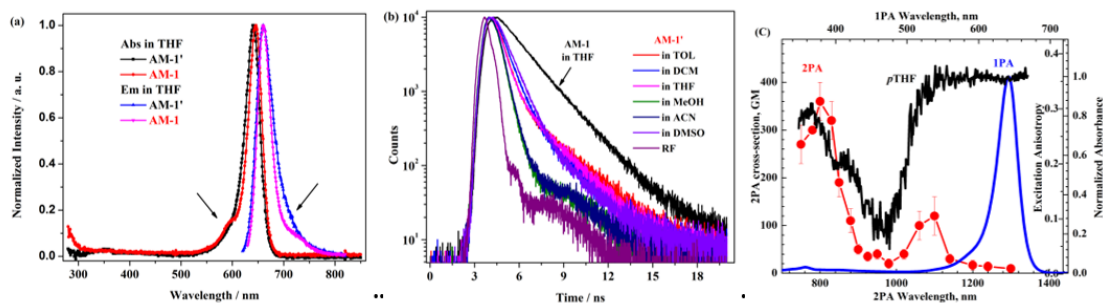
Figure 6.3 Photophysical properties of **AM-1** and **AM-1'**. (a) Normalized absorption spectra and fluorescence emission spectra of **AM-1'** and **AM-1** in THF; (b) Fluorescence lifetime kinetics of dye **AM-1'** in different solvents; (c) Excitation anisotropy in *p*THF and 2PA spectrum of dye **AM-1'** in DCM.

Table 6.1 Main Photophysical and Photochemical Parameters of Dye **AM-1' and AM-1**

Comps	Solvs	λ_{abs} (nm, ±1)	ε_{max} (×10^5 M^{-1}·cm^{-1})	λ_{em} (nm, ±1)	$\Delta\lambda$ (nm, ±2)	FWHM (nm, ±2)	τ_F (ns, ±5%)	Φ_F (±5%)
	TOL	641	2.29	660	19	38	0.84	0.19
	DCM	641	2.15	664	23	41	0.82	0.21
AM-1'	THF	641	2.09	660	19	41	0.79	0.18
	MeOH	639	2.28	665	26	49	0.41	0.11
	ACN	641	2.27	664	23	45	0.42	0.13
	DMSO	653	2.15	677	24	47	0.85	0.26
AM-1	THF	646	2.9	660	14	30	1.74	0.67

λ_{abs} and λ_{em}-absorption and emission wavelengths maximum. ε_{max}-molar extinction coefficient at λ_{abs}. $\Delta\lambda$-Stokes shift. FWHM-full width at half maximum. Φ_F-fluorescence quantum yield. τ_F- average fluorescence lifetime.
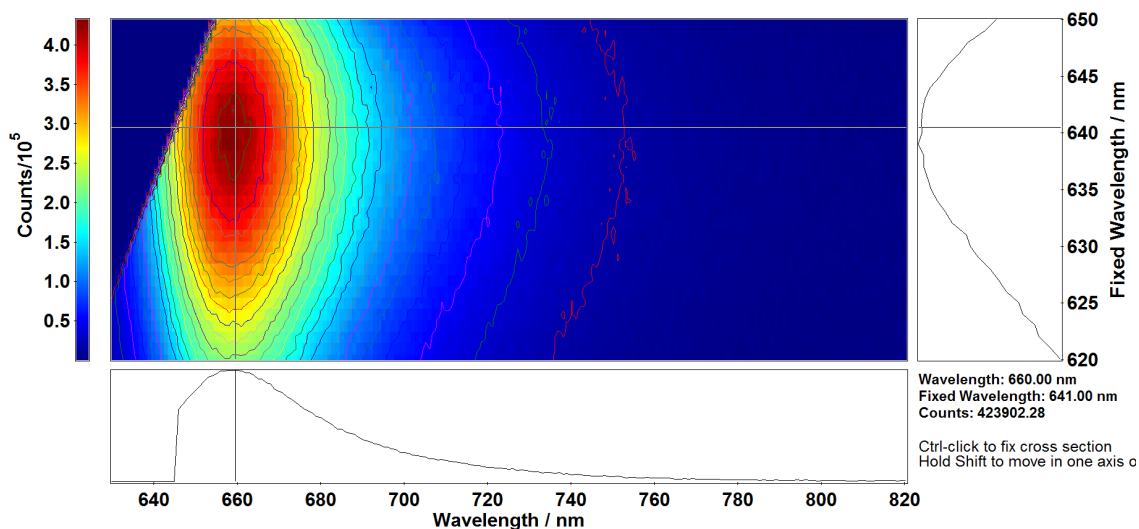
Figure 6.4. Synchronous spectra map of **AM-1'** in THF.

Table 6.2 Main Photophysical Parameters of Dye **AM-1** in Different Solvents

Solvents	ε_{max} $[\times 10^5\,M^{-1}\cdot cm^{-1}]$	λ_{abs} [nm]	λ_{em} [nm]	$\Delta\lambda$ [nm]	τ_F [ns]	Φ_F
THF	2.90	646	660	14	1.74	0.67
ACN	2.88	642	659	17	1.65	0.77
TOL	3.42	646	659	13	1.86	0.81
DCM	2.98	646	659	13	1.81	0.88
DMSO	1.23	652	674	22	---	---

6.23 Aggregation Properties of Dyes AM-1' and AM-1 in Aqueous Solutions

One important aspect of many squaraines is their tendency to form aggregates *via* van der Waals' forces and π-π stacking interactions. Typical assignments of aggregation state are based on aggregation-induced spectral shifts in absorption spectra, where a red-shift is characteristic of J-aggregate and a blue-shift is characteristic of H-aggregate, as originally described by Kasha.[281] Aggregation of squaraine compounds is significantly less efficient in neat organic solvents as compared to in aqueous/organic solvent mixtures or aqueous media.[281-285] No observation of aggregates for **AM-1'** was found even in polar solvents such as MeOH and dimethyl sulfoxide (DMSO). While **AM-1** in DMSO showed a blue-shifted absorption band at 552 nm in addition to the monomer at 650 nm as shown in Figure 6.5, which is attributed to the H-aggregate related to the strong π-π intermolecular interactions.[286] In light of these observations, we further examined the optical changes of these two compounds in the presence of water. In THF-H_2O mixtures, no shift of maximum absorption was found for **AM-1'**, while the intensity decreased until THF content reached 40% (Figure 6.6a). Below this point, a new, low-energy absorption band at 760 nm indicated the formation of J-aggregation triggered by the presence of water. We also

investigated their absorption properties in the presence of ionic and nonionic surfactants such as cetyltrimethylammonium bromide (CTAB, 1.0 mM) and Pluronic F-127 (2.0 wt%), respectively. Interestingly, instead of disrupting J-aggregation, it appears that these surfactants support the formation of J-aggregates. Notably, the strong tendency for **AM-1** to undergo H-aggregation under the same conditions are consistent with previously reported results,[263,287] with the contrasting aggregation tendency due to the major structural differences of the two squaraines (Figures 6.6b and 6.5).

The fluorescence emission spectrum for J-aggregated **AM-1'** consisted a weak emission band centered at 820 nm with a large Stokes shift (Figure 6.6c). Despite the structural distortion, the core of the dye retains a certain amount of overall planarity, which would still facilitate intermolecular π-π stacking interaction. In the aggregated state of **AM-1'**, the slipped stack may comfortably accomodate the large adamantyl arms and, at the same time, enable short interplanar spacing.[288-291]
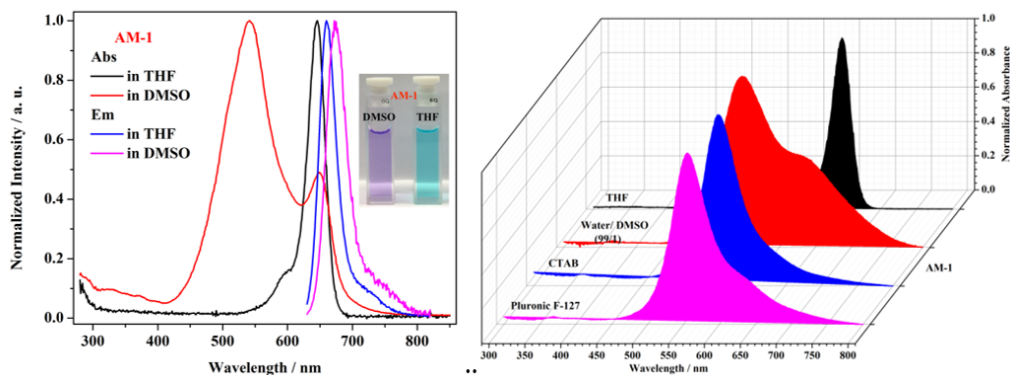
Figure 6.5 Normalized absorption and emission spectra of **AM-1** in THF and DMSO. Inset shows the color of **AM-1** solution in pure DMSO and THF (left). Absorption spectra of **AM-1** in THF, water-DMSO mixture, CTAB and pluronic F-127 micellar solutions (right).
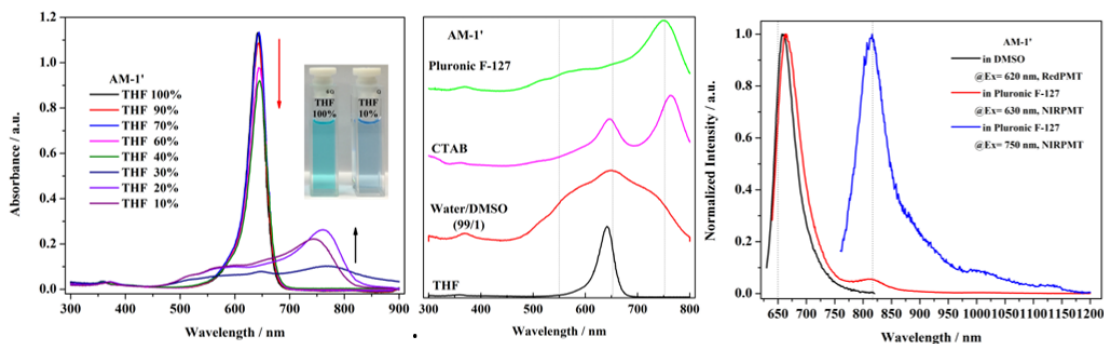
Figure 6.6 Absorption changes of **AM-1'** in THF-H$_2$O mixtures. Inset shows the color of **AM-1'** in pure THF and 10% THF solution (a); Absoprtion spectrum of **AM-1'** in different aqueous media (d); Emission spectrum of **AM-1'** in DMSO excited at 620 nm with RedPMT detector and pluronic F-127 micellar solutions excited at 630 nm and 750 nm with NIRPMT detector, respectively.

6.24 Fluorescence Emission "Turn-on" Response of Dye AM-1' Towards *β*-CD

It is well known that cyclodextrins (CDs) possess unique structures that make its outer surface hydrophilic and its inner surface hydrophobic; thus it can form supramolecular inclusion complexes with hydrophobic small molecules fit into its 5-8 Å cavity.[270] The fluorescence intensity, water solubility (and probable biocompatibility), and photostability of the guest fluorophores may be enhanced through complexation with CDs. Moreover, the adamantyl group is known for its capability to form stable guest-host inclusion complexes with *β*-CD derivatives with high association constants (K_a) on the order of 10^4-10^5, as shown in Scheme 1.[292-296] To examine the guest-host effect on photophysical properties, absorption and emission spectral changes of the two compounds in the presence of *β*-CD were monitored. Figure 6.7a shows the continuous enhancement of the fluorescence intensity of **AM-1'** in water with gradual addition of *β*-CD, with the inset showing the absorption change in the absence as well as the presence of 5.0 mM of *β*-CD. Interestingly, a decrease in the J-aggregation absorption was found in the presence of *β*-CD while the

monomer absorption and the fluorescence emission were recovered (c.f. Figure 6.7b). The inclusion of hydrophobic guest molecule **AM-1'** into the cavity of β-CD increases the hydrophobicity of the microenvironment, which resulted in the enhancement of the fluorescence intensity. The involvement of pendant β-CD also increased the steric hindrance and the so-called adjacent distance between the molecular transition dipoles in stacked molecules, leading to reduced efficiency of J-aggregation.

The fluorescence quantum yield of the inclusion complex **AM-1'$\subset\beta$-CD** was was ca. 0.04 (τ_F=0.58 ns), and the fluorescence intensity reached a maximum at a 4.5 μM concentration of **AM-1'** in 5 mM β-CD solution (c.f. Figure 6.7c). The binding interaction between **AM-1'** and β-CD in water was analyzed by the Benesi-Hildebrand equation, showing a 1:2 complex formation and a calculated equilibrium constant of 1.1×10^4 L$^2\cdot$mol^{-2} (Figure 6.8).[297-299] It should be noted that one unusual phenomena of the high ratio of the host molecules to guest molecules was observed by the fluorescence intensity changes. With the adamantyl group known to have highly affinity and tight binding to β-CD, the main body of the squaraine core is reasoned to remain outside of the CD cavity (Scheme 1) and surrounded by water molecules. However, the effect of polarity and hydrogen bonding of solvents to squaraines on the fluorescent properties is not easy to predict.[300,301] It seems that the fluorescence intensity was enhanced by both the guest-host interactions and hydrophobic microenvironment provided by β-CD. Solutions containing the complex **AM-1'$\subset\beta$-CD** were further prepared at the optimized concentration ratio for cell imaging.
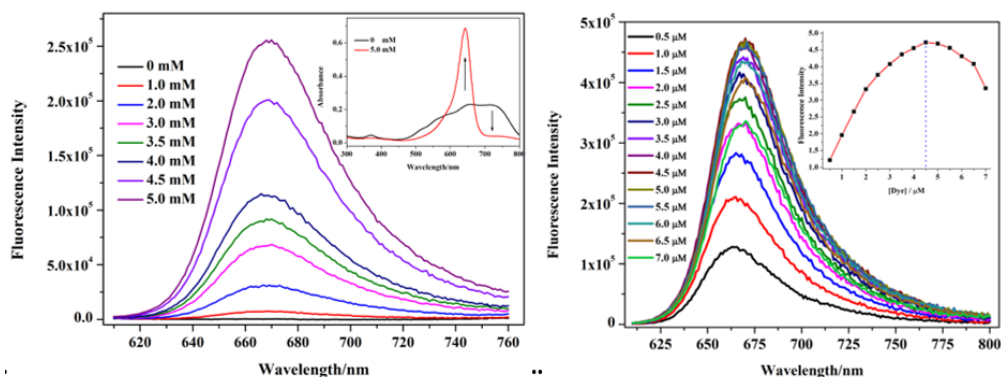
Figure 6.7 (a) Fluorescence emission changes of **AM-1'** in water upon the addition of β-CD. Inset show the absorption changes in the absence and presence of 5.0 mM β-CD. (b) Fluorescence emission of increasing the dye concentration in 5.0 mM β-CD. Inset plots show fluorescence emission maximum intensity as a function of the concentration of the dye.
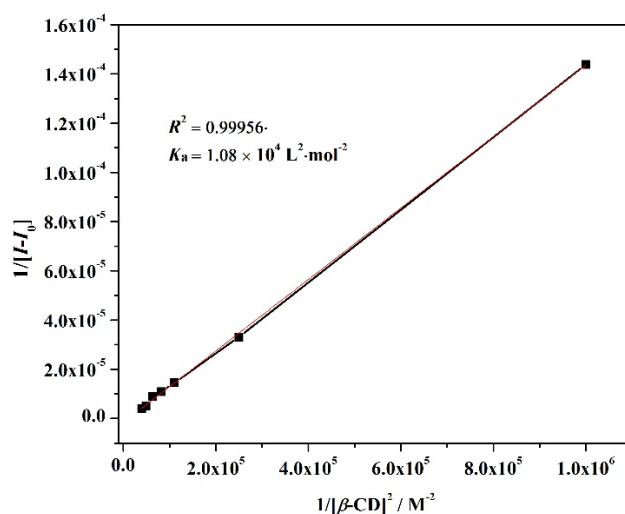
Figure 6.8 Benesi-Hildebrand plot of the binding interaction between **AM-1'** and β-CD in water.

6.25 One- and Two-photon Fluorescence Bioimaging

Exploiting the interactions between adamantane and β-CD, the potential utility of the complex **AM-1'$\subset\beta$-CD** for fluorescence microscopy cellular imaging was explored using HCT 116 cells (human colorectal carcinoma cell line). Cell viability of the **AM-1'$\subset\beta$-CD** complex was evaluated using HCT 116 cells via the MTS assay (Figure 6.9).[302,303] The

results indicate that the complex **AM-1'⊂β-CD** solution exhibits low cytotoxicity over a concentration range from 23.4 μM to 5.0 mM, appropriate for cell imaging.
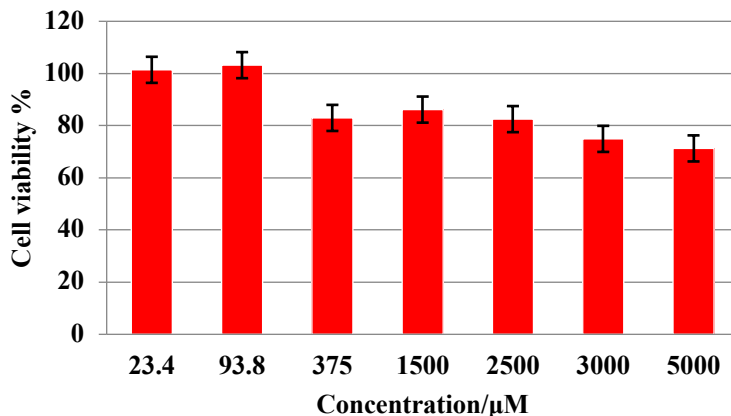
Figure 6.9 Cell viability assay of HCT 116 cell line incubated with the inclusion complex **AM-1'⊂β-CD**.

On the basis of cell viability results, 3 μM **AM-1'** with 3 mM β-CD in culture medium solution was used for fluorescence cell imaging with HCT 116 cells. Cells incubated with the dye-CD complex exhibited bright fluorescence from an area surrounding nucleus (Figure 6.10). By comparison, no fluorescence was observed for cells incubated with compound AM-1' alone (not shown). In addition, the two-photon fluorescence imaging was also conducted. As presented in Figure 6.11, the three-dimensional (3D) profile of HCT 116 cells incubated with the **AM-1'⊂β-CD** complex was revealed by image reconstruction using Fiji software, and the orthoslice image indicated strong fluorescence from the y- and z-views. The excitation wavelength employed in the two-photon fluorescence microscopy (2PFM) imaging experiment was 860 nm, which is in the near infrared window, potentially facilitating deeper penetration compared with typical one-photon excitation in the visible range. One- and two-photon fluorescence

microscopy imaging results indicate that the **AM-1' ⊂ β-CD** complex may possess
potential for use in two-photon deep tissue imaging, an aspect to be explored in future
studies.

| DIC | Inclusion complex | Hoechst | Merged |
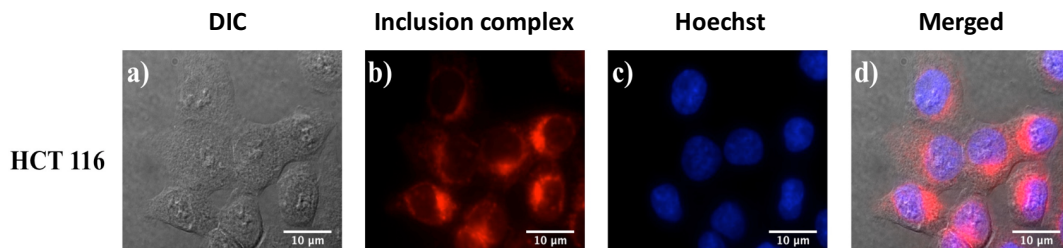
Figure 6.10. Fluorescence images of HCT 116 cells incubate with **AM-1'⊂β-CD** complex
(3 μM and 3 mM, respectively) and Hoechst (1 μg/ml). (a) DIC; (b) **AM-1' ⊂ β-CD**
complex; (c) Hoechst; and (d) Merged image (Ex: 562/40nm; Em: 624/40nm; TxRed filter;
60x oil immersion objective).
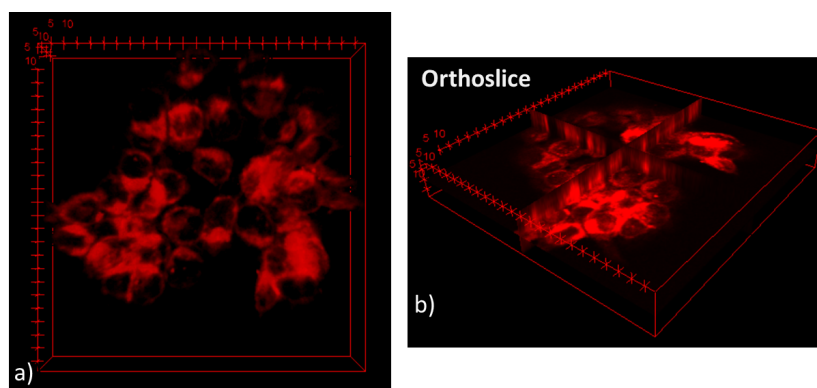
Figure 6.11 (a)3D reconstruction image and (b)orthoslice image show strong
fluorescence in HCT 116 cells. (76 MHz, 200 fs pulse width, Ex: 860 nm; Em: 660/50
nm; 20x water immersion objective).

6.3 Experimental Details

6.31 Materials and Methods

All reagent chemicals and solvents were used as purchased without further purification
unless otherwise noted. Thin-layer chromatography (TLC) was performed on pre-coated
silica gel 60 F254 plates. Column chromatography was performed over silica gel 230-400

mesh. The ^{1}H and ^{13}C NMR measurements were performed at room temperature by a Bruker Avance III NMR spectrometer at 500 and 126 MHz respectively, with tetramethylsilane (TMS) as an internal reference. Liquid chromatography was performed on a Waters Acquity UPLC system (Waters, Milford, MA) equipped with a photodiode array detector monitored in wide band from 190 to 400 nm. The mobile phase program is isocratic with 90% B for 2 min with flow rate at 0.1 mL/min (A=0.1% formic acid in water; B=0.1% formic acid in acetonitrile). Waters QTOF Premier mass spectrometer (Waters, Milford, MA) was operated in the positive ion, V-mode at a mass resolution of 9000 (FWHM) at m/z 556. Melting points are uncorrected. The Boc-protection of piperidine-4-carboxylic acid (**A**) and 1-(2-bromoethoxy)-2-(2-methoxyethoxy)ethane were performed based on the previously reported literatures.

6.32 Linear Photophysical and Photochemical Measurements

The optical properties of compound AM-1 and AM-1' were investigated in spectroscopic-grade solvents: toluene (TOL), tetrahydrofuran (THF), dichloromethane (DCM), methanol (MeOH), acetonitrile (ACN), and dimethyl sulfoxide (DMSO), purchased from commercial suppliers and used without further purification. UV-Vis spectra were recorded using a Tecan Infinite® M200 PRO plate reader spectrometer in 10 mm path length quartz cuvettes. The steady-state fluorescence spectra and excitation anisotropy spectra were recorded with an Edinburgh Instruments FLS980 fluorescence spectrometer and dye concentration, $C\sim10^{-6}$ mol/L. Fluorescence lifetimes (τ_F) were determined with the single photon counting technique (TCSPC) with the same Edinburgh FLS980 spectrometer using a pulsed picosecond diode laser (EPL-635) as the excitation source. Examining the mono- or bi-exponential decay and minimizing the χ^2 value checked the quality of fits. It should

be mentioned that under the employed experimental conditions the maximum optical density of the investigated solutions did not exceed 0.1 and all reabsorption effects were negligible. Fluorescence quantum yield (Φ_F) measurements were performed by using the standard procedure with cresyl violet in MeOH ($\Phi_F = 0.54$) as reference compound.[5] All the absorption and emission measurements were performed around 20 ºC. Stock solutions of the dyes in THF were prepared at a concentration of ~ 0.3 mg/mL. In the mixed solvent studies, injecting the stock solution into the blank solvent blends with different volumes made the final solutions. The pure blank solvent blends were used to set the baseline of the instrument before taking the absorption measurement for each corresponding mixed-solvent solution.

6.33 Determination of the Fluorescence Quantum Yields (Φ_F)

Fluorescence quantum yields were determined by a standard relative method using the equation (6.1) as follows,

$$\Phi_F = \frac{I}{I_R} \times \frac{OD_R}{OD} \times \frac{n^2}{n_R^2} \times \frac{RP_R}{RP} \times \Phi_F^R \tag{6.1}$$

where Φ_F is the fluorescence quantum yield, the subscript R refers to the reference, I is the integrated emission signal, OD is the optical density at the excitation wavelength, n is the refractive index of the solvent, and RP is the relative power of the light source of the spectrofluorimeter at the excitation wavelength.

6.34 2PA Measurements

Degenerate 2PA spectra of new squaraines were obtained with a femtosecond 1 kHz laser system (Ti:sapphire regenerative amplifier (Legend Duo$^+$) pumping OPO (HE-TOPAS), all lasers from Coherent, Inc.) using open aperture Z-scan technique. All measurements were performed in 1 mm quartz cells with dye concentrations ~10^{-3} M. Experimental Z-scan setup was calibrated with ZnSe, CdSe and SiO$_2$ as standards.

6.35 Cell Culture and Incubation

To estimate the cytotoxicity of the inclusion complex **AM-1'⊂β-CD**, HCT 116 cells were cultured in Minimum Essential Medium supplemented with 10% fetal bovine serum and 1% penicillin, 1% streptomycin at 37 ℃, in a 95% humidified atmosphere containing 5% CO$_2$. Cells were seeded in 96-well plates (Corning, USA) at a concentration of 5×10^3 cells/well for 48 h. Next, HCT 116 cells were incubated with different concentrations of the inclusion complex (complex contains **AM-1'⊂β-CD** in a concentration ratio of 1: 1000). Stock complex solution was diluted into a final solution containing 23.4 μM, 93.8 μM, 375.0 μM, 1500.0 μM, 2500.0 μM, 3000.0 μM, 5000.0 μM β-CD. Cells were then incubated with diluted solution for 22 h. After that, 20 μL of Cell Titer 96 Aqueous One solution reagent was added into each well followed by incubation for 2 h additionally. The respective absorbance values were measured on a Tecan Infinite® M200 PR plate reader spectrometer at 490 nm to determine the relative amount of formazan produced. Cell viabilities were calculated based on the following equation (6.2):

$$\text{Cell viability (\%)} = \frac{\text{Abs}^{\text{S}}_{490\text{nm}} - \text{Abs}^{\text{D}}_{490\text{nm}}}{\text{Abs}^{\text{C}}_{490\text{nm}} - \text{Abs}^{\text{D2}}_{490\text{nm}}} \times 100\% \tag{6.2}$$

where $\mathrm{Abs}_{490\mathrm{nm}}^{\mathrm{S}}$ is the absorbance of the cells incubated with different concentrations of the dye solutions, $\mathrm{Abs}_{490\mathrm{nm}}^{\mathrm{D}}$ is the absorbance of cell-free well containing only dye at the investigated concentration, $\mathrm{Abs}_{490\mathrm{nm}}^{\mathrm{C}}$ is the absorbance of the cells only incubated in medium, and $\mathrm{Abs}_{490\mathrm{nm}}^{\mathrm{D2}}$ is the absorbance of the cell-free well.

6.36 One- and Two-photon Fluorescence Microscopy Cell Imaging

HCT 116 and CHO-K1 cells were placed onto poly-D-lysine coated coverslips in 24-well plated at the density of 5×10^4 cells/well and incubated for 48 h. The investigated complex solution was diluted to the concentration of 3 μM dye and 3 mM β-CD and added to cells. After 1.5 h incubation, the complex solutions were extracted and the coverslipped cells were washed abundantly with PBS buffer (2×). After incubated with medium containing 1 μg/ml Hoechst for nucleic acid staining, cells were fixed with 3.7% formaldehyde solution in PBS buffer at room temperature for 10 min. The fixing agent was extracted and washed (2×) with PBS. A fresh solution of $NaBH_4$ (1.0 mg/mL) in PBS buffer was used to treat the fixed cells for 10 min (2×) to reduce the autofluorescence. The coveslipped cells were then washed with PBS buffer (2×), deionized water (1×), and mounted on microscope slides using an antifade mounting media (Prolong Gold) for imaging.

Conventional fluorescence cell images were obtained on an inverted microscope (Olympus IX71) equipped with a Q-Imaging cooled CCD and a 100 W mercury lamp. The TexRed filter cube (Ex: 562/40; DM: 593; Em: 624/40) was used to match the excitation wavelength of the inclusion complex and to capture most of its emission profile. A customized filter cube (Ex: 377/50 nm; DM: 420 nm; Em: 460/40 nm) was used for the nucleic acid imaging.

2PFM imaging was performed using a Bruker Ultima fluorescence microscopy system equipped with a Coherent Mira 900F laser source (76 MHz, mode-locked, 200 fs pulse width). Cells were excited at 860 nm and the emission was collected using an external non-descanned PMT detector (NDD) (Em: 660/50 nm). A 20x, 1.0 N.A. water immersion objective was employed for the 2PFM imaging. 3D reconstruction and statistical analysis of scanned images was performed with the Fiji software.

6.37 Synthesis of Compound B, C and D

In a 250 mL round-bottomed flask equipped with a magnetic stir bar and a reflux condenser, compound **A** (5.0 g, 21.8 mmol), DCC (4.5 g, 21.8 mmol), 1-adamantanemethanol (3.8 g, 22.9 mmol), DMAP (0.54 g, 4.4 mmol) and dry DCM (150 mL) were added. The reaction mixture was heated to refluxing for 12 h under N_2 atmosphere. After cooling down, the mixture was filtered and the filtrate was concentrated under reduced pressure to afford a colorless oil. The crude mixture was purified by column chromatography (10/1, *v/v*, *n*-hexane/ethyl acetate on silica, R_f=0.40), affording compound **B** as a colorless oil (7.6 g, 92%). ^{1}H NMR (500 MHz, CDCl$_3$) δ: 4.02 (s, 2 H), 3.68 (s, 2 H), 2.84 (t, J = 11.3 Hz, 2 H), 2.47 (ddd, J = 11.0, 7.3, 4.0 Hz, 1 H), 1.98 (s, 3 H), 1.90 (d, J = 12.0 Hz, 2 H), 1.74 (s, 2 H), 1.67 (dd, J = 20.6, 9.9 Hz, 6 H), 1.52 (m, 6 H), 1.46 (s, 9 H). ^{13}C NMR (126 MHz, CDCl$_3$) δ: 174.58, 154.69, 79.52, 73.97, 43.29, 41.32, 39.26, 36.91, 33.26, 28.40, 28.05, 27.97.

Compound **B** (6.0 g, 15.9 mmol) was dissolved in 100 mL DCM and cooled to 0 °C. TFA was added and the solution was allowed to warm to room temperature. After stirring at room temperature until starting material was consumed (TLC monitoring), the solution was poured into water, neutralized with NaOH solution, and extracted. The

combined organic layer was dried over MgSO₄, filtered and concentrated to give a colorless oil in quantitative yield that was used immediately for the next step. Phloroglucinol (2.0 g, 15.9 mmol), 1-butanol (40 mL) and toluene (80 mL) were added to the above intermediate and heated at reflux with a Dean-Stark apparatus for 8 h. During that time, the solution progressed from colorless to pale red. Excess solvent was removed under reduced pressure, which left a reddish oil that was purified by column chromatography (1/1, *v/v*, *n*-hexane/ethyl acetate on silica, R_f=0.46), affording **C** as a white solid (5.0 g, 81%). ¹H NMR (500 MHz, DMSO-d_6) δ: 8.92 (s, 2 H), 5.77 (s, 2 H), 5.68 (s, 1 H), 3.65 (s, 2 H), 3.47 (d, *J* = 12.5 Hz, 2 H), 2.68 (t, *J* = 11.2 Hz, 2 H), 2.47 (s, 1 H), 1.94 (s, 3 H), 1.87 (d, *J* = 11.4 Hz, 2 H), 1.69 (s, 2 H), 1.62 (t, *J* = 12.2 Hz, 6 H), 1.49 (m, 6 H). ¹³C NMR (126 MHz, DMSO-d_6) δ: 174.68, 159.22, 153.30, 95.02, 94.47, 73.35, 48.43, 40.88, 39.14, 36.90, 33.42, 27.99, 27.86. LC-MS (*m/z*): [M+H]⁺ Calculated for $C_{23}H_{32}NO_4$, 386.2326; Found, 386.2327.

Compound **C** (2.3 g, 6.0 mmol), 1-bromo-2-(2-(methoxyethoxy)ethoxy)ether (1.5 g, 6.6 mmol), 18-crown-6 (0.16 g, 0.6 mmol) and K_2CO_3 (0.91 g, 6.6 mmol) were refluxed in CH_3CN (100 mL). After 12 h, the solution was cooled to room temperature and concentrated before water was added. The aqueous solution was extracted by dichloromethane three times. The combined organic phase was dried over anhydrous Na_2SO_4, concentrated in vacuum, and purified by column chromatography on silica (2/1, *v/v*, ethyl acetate/hexane on silica, R_f=0.34), affording the final product **D** as a yellowish oil (1.4 g, 44%). ¹H NMR (500 MHz, CDCl₃): δ 6.85 (s, 1 H), 6.07 (s, 2 H), 5.95 (s, 1 H), 4.02 (t, *J* = 4.6 Hz, 2 H), 3.78 (t, *J* = 4.6 Hz, 2 H), 3.73-3.63 (m, 8 H), 3.61-3.53 (m, 4 H), 3.38 (s, 3 H), 2.75 (t, *J* = 11.3 Hz, 2 H), 2.45 (t, *J* = 10.9 Hz, 1 H), 2.00 (d, *J* = 15.1 Hz, 5

H), 1.86 (dd, J = 21.4, 10.8 Hz, 2 H), 1.73 (d, J = 12.0 Hz, 3 H), 1.65 (d, J = 11.9 Hz, 3 H),

1.53 (m, 6 H). ^{13}C NMR (126 MHz, CDCl$_3$) δ 175.00, 160.60, 157.99, 153.01, 97.13, 96.30,

94.06, 74.06, 71.89, 70.65, 70.63, 70.43, 69.73, 67.36, 58.97, 49.20, 41.16, 39.30, 36.95,

33.30, 28.01, 27.87. LC-MS (m/z): [M+H]$^+$ Calculated for C$_{30}$H$_{46}$NO$_7$, 532.3269; Found,

532.3255.

6.38 Synthesis of Dye AM-1' and AM-1

In a 250mL round bottom flask, compound **D** (1.1 g, 2.0 mmol) and squaric acid (0.11 g,

1.0 mmol) were dissolved in a 1-butanol/toluene mixture (100 mL, 1/1, v/v). The resulting

mixture was heated at reflux with a Dean–Stark apparatus for 2 h to generate a dark green

solution. After most of the solvent was distilled, the reaction mixture was cooled to room

temperature and dried under reduced pressure. The crude mixture was purified by column

chromatography (9/1, v/v, DCM/methanol on silica, R_f=0.58) to afford dye **AM-1'** as a blue

solid (0.31 g, 27%). M. p.: 173-174 °C. ^{1}H NMR (500 MHz, CDCl$_3$) δ: 14.12 (s, 2 H),

5.91 (s, 2 H), 5.79 (s, 2 H), 4.18 (t, J = 5.0 Hz, 4 H), 4.04 (t, J = 5.1 Hz, 4 H), 3.91 (d, J =

13.6 Hz, 4 H), 3.79-3.73 (m, 4 H), 3.71 (s, 4 H), 3.70-3.66 (m, 4 H), 3.66-3.62 (m, 4 H),

3.57-3.51 (m, 4 H), 3.36 (s, 6 H), 3.16 (t, J = 11.5 Hz, 4 H), 2.70-2.60 (m, 2 H), 2.04 (d, J

= 11.3 Hz, 4 H), 2.00 (s, 6 H), 1.82 (dd, J = 21.0, 10.4 Hz, 4 H), 1.74 (d, J = 12.1Hz, 6 H),

1.65 (d, J = 12.3 Hz, 6 H), 1.53 (m, 12 H). ^{13}C NMR (126 MHz, CDCl$_3$) δ: 173.91, 166.64,

162.86, 157.79, 104.53, 95.81, 89.58, 74.22, 71.91, 70.71, 70.59, 70.38, 69.10, 68,54,

59.00, 46.68, 40.85, 39.32, 36.93, 33.31, 28.03, 27.84. M. p.: 173-174 °C. LC-MS (m/z):

[M+H]$^+$ Calculated for C$_{64}$H$_{89}$N$_2$O$_{16}$, 1141.6207; Found, 1141.6223.

In a 250 mL round bottom flask, compound **C** (3.8 g, 10.0 mmol) and squaric acid

(0.57 g, 5.0 mmol) were dissolved in a 1-butanol/toluene mixture (100 mL, 1/1, v/v). The

resulting mixture was heated at reflux with a Dean-Stark apparatus for 8 h to generate a dark green solution. After most of the solvent was distilled, the reaction mixture was cooled to room temperature. The precipitation product was collected by filtration and washed with cold methanol, affording the final product **AM-1** as a blue-green solid (2.1 g, 50%). M. p.: 298-299 °C. ^{1}H NMR (500 MHz, CDCl$_3$) δ: 10.94 (s, 4 H), 5.92 (s, 4 H), 3.91 (dt, J = 13.6, 4.4 Hz, 4 H), 3.71 (s, 4 H), 3.20 (ddd, J = 13.8, 10.6, 3.1 Hz, 4 H), 2.65 (dq, J = 9.7, 4.8, 4.4 Hz, 2 H), 2.08–1.94 (m, 10 H), 1.85 (m, 4 H), 1.75 (d, J = 12.5 Hz, 6 H), 1.69-1.60 (m, 6 H), 1.53 (dd, J = 2.8, 1.2 Hz, 12 H). ^{13}C NMR (126 MHz, CDCl$_3$) δ: 181.30, 173.78, 163.43, 162.32, 158.68, 103.05, 94.32, 74.30, 53.42, 46.68, 40.77, 39.33, 36.93, 33.32, 27.99, 27.95. LC-MS (m/z): [M+H]$^+$ Calculated for C$_{50}$H$_{61}$N$_2$O$_{10}$, 849.4321; Found, 849.4344.

6.4 Conclusion

In this work, two novel squaraine compounds bearing admantyl termini were designed and synthesized. The various photophysical properties for the two squaraine derivatives, resulting from molecular structure differences, have been characterized and compared. In summary, **AM-1** underwent H-aggregation in aqueous media while compound **AM-1'** displayed a tendency to form J-aggregates. Further investigation demonstrated that the introduction of β-CD successfully interrupted the aggregation propensity of **AM-1'** in aqueous media and enhanced the fluorescence intensity. Moreover, one- and two-photon fluorescence imaging of HCT 116 cells incubated with the **AM-1'** $\subset$ **β-CD** complex exhibited bright far-red to near-IR fluorescence, suggesting its potential as a probe for use in 2PFM tissue imaging.

REFERENCES

1.   J. R. Lakowicz in *Principles of Fluorescence Spectroscopy*, Springer, New York, N. Y. **1999,** pp. 1-25.

2.   G. Weber, D.M. Hercules, in *Fluorescence and Phosphorescence Analysis. Principles and Applications* (J. Wiley & Sons), Interscience Publishers，New York, N.Y. **1966**, pp. 217-240.

3.   T. Liu, X. Liu, M. A. Valencia, B. Sui, Y. Zhang, K. D. Belfiled, *Eur. J. Org. Chem.* **2017**, *22*, 3957-3964.

4.   X. Liu, A. Ardizzone, B. Sui, M. Anzola, N. Ventosa, T. Liu, J. Vecoana, K. D. Belfield, *ACS Omega*, **2017**, *2*, 4112-4122.

5.   H. Sosa, A. B. Astnjo, E. J. G. Peterman, *Methods in Cell Biology*, **2010**, *95*, 505-519.

6.   A. Jablonski, *Bull l'Acad Pol Sci, Ser A*, **1960**, *8*, 259-264.

7.   T. Heyduk, Y. Ma, H. Tang, R. H. Ebright, *Methods Enzymol*, **1996**, *274*, 492-503.

8.   A. Marczak, *Bioelectrochemistry*, **2009**, *74*, 236-239.

9.   H. Zhang, Q. Wu, M. Y. Berezin, *Expert Opin Drug Discov*, **2015**, *10*, 1145-1161.

10.   K. Svoboa, R. Yasuda, *Neuron*, **2006**, *50*, 823-839.

11.   J. Yum, P. Walter, S. Huber, D. Rentsch, T. Geiger, F. Nuesch, F. D. Angelis, M. Gratzel, M. K. Nazeeruddin, *J. Am. Chem. Soc.* **2007**, *129*, 10320-10321.

12.   G. Wei, X. Xiao, S.Wang, J. D. Zimmerman, K. Sun, V. V. Diev, M. E. Thompsom, S. R. Forrest, *Nano Lett.* **2011**, *11*, 4261-4264.

13.   C. C. Corredor, Z. L. Huang, K. D. Belfield, *Adv. Mater*. **2006**, *18*, 2910-2914.

14.   C. C. Corredor, Z, Huang, K. D. Belfield, A. R. Morales, M. V. Bondar, *Chem. Mater.* **2007**, *19*, 5165-5173.

15.   M. Ha-Thi, M. Penhoat, D. Drouin, M. Blanchard-Desce, V. Michelet, I. Leray, *Chem. Eur. J.* **2008***, 14*, 5941-5950.

16.   X. Yue, C. O. Yanez, S. Yao, K. D. Belfield, *J. Am. Chem. Soc.* **2013**, *135*, 2112-2115.

17.   A. Fadhel, X. Yue, E. H. G. Zadeh, M. V. Bondar, K. D. Belfield, *Int. J. Nanomedicine*. **2016**, *11*, 6161-6168.

18.   H. Y. Ahn, S. Yao, X. Wang, K. D. Belfield, *ACS Appl. Mater. Interface.* **2010,** *4*, 2847-2854.

19.   G. M. Tozer, S. M. Ameer-Beg, J. Baker, P. R. Barber, S. A. Hill, R. J. Hodgkiss, R. Locke, V. E. Prise, I. Wilson, B. Vojnovic, *Adv. Drug Deliver Rev.* **2005**, *57*, 135-152.

20.   S. Yao, K. J. Schafer-Hales, K. D. Belfield, *Org. Lett.* **2007**, *9*, 5645–5648.

21.   P. Jiang, Z. Q. Tian, C. N. Zhu, Z. L. Zhang, D. W. Pang, *Chem. Mater*. **2012**, *24*, 3−5.

22.   L. Ren, F. Liu, X. Shen, C. Zhang, Y. Yi, X. Zhu, *J. Am. Chem. Soc.* **2015**, *137*, 11294−11302.

23.   C. Wu, J. Yu, F. Ye, Y. Rong, M. E. Gallina, B. S. Fujimoto, Y. Zhang, Y. H. Chan, W. Sun, X. H. Zhou, C. Wu, D. T. Chiu, *J. Am. Chem. Soc.* **2015**, *137*, 173−178.

24.   C. Tchounwou, S. S. Sinha, B. P. Viraka Nellore, A. Pramanik, R. Kanchanapally, S. Jones, S. R. Chavva, P. C. Ray, *ACS Appl. Mater. Interfaces* **2015**, *7*, 20649−20656.

25.   D. K. Bwambok, B. El-Zahab, S. K. Challa, M. Li, L. Chandler, G. A. Baker, I. M. Warner, *ACS Nano* **2009**, *3*, 3854−3860.

26.   L. Yuan, W. Lin, Y. Yang, H. A. Chen, *J. Am. Chem. Soc.* **2012**, *134*, 1200−1211.

27.   U. Oguz, E. U. Akkaya, J. Org. Chem. **1998**, *63*, 6059−6060.

28.   T. Goh, J. S. Huang, E. A. Bielinski, B. A. Thompson, S. Tomasulo, M. L. Lee, M. Y. Sfeir, N. Hazari, A. D. Taylor, *ACS Photonics* **2015**, *2*, 86−95.

29.   D. Yang, Y. Zhu, Y. Jiao, L. Yang, Q. Yang, Q. Luo, X. Pu, Y. Huang, S. Zhao, Z. Lu, *RSC Adv.* **2015**, *5*, 20724−20733.

30. T. Maeda, S. Nitta, H. Nakao, S. Yagi, H. Nakazumi, *J. Phys. Chem. C* **2014**, *118*, 16618−16625.

31. C. C. Corredor, Z. L. Huang, K. D. Belfield, *Adv. Mater.* **2006**, *18*, 2910−2914.

32. M. Emmelius, G. Pawlowski, H. W. Vollmann, *Int. Ed. Engl.* **1989**, *28*, 1445−1471.

33. V. B. Jipson, C. R. Jones, *J. Vac. Sci. Technol.* **1981**, *18*, 105−109.

34. Y. Zhang, B. Kim, S. Yao, M. V. Bondar, K. D. Belfield, *Langmuir* **2013**, *29*, 11005−11012.

35. C. L. Sun, Q. Liao, T. Li, J. Li, J. Q. Jiang, Z. Z. Xu, X. D. Wang, R. Shen, D. C. Bai, Q. Wang, et al. *Chem. Sci.* **2015**, *6*, 761−769.

36. S. Lee, B. A. Son, Y. A. Rao, *Sens. Sens. Actuators, B* **2015**, *210*, 519−532.

37. Ajayaghosh, *Acc. Chem. Res.* **2005**, *38*, 449−459.

38. A. Karpenko, A. S. Klymchenko, S. Gioria, R. Kreder, I. Shulov, P. Villa, Y. Mely, M. Hibert, D. Bonnet, *Chem. Commun.* **2015**, *51*, 2960−2963.

39. C. Luo, Q. Zhou, G. Jiang, L. He, B. Zhang, X. Wang, *New J. Chem.* **2011**, *35*, 1128−1132.

40. S. A. Kurhuzenkau, A. W. Woodward, S. Yao, K. D. Belfield, Y. O. Shaydyuk, C. Sissa, M. V. Bondar, A. Painelli, *Phys. Chem. Chem. Phys.* **2016**, *18*, 12839−12846.

41. S. Wang, L. Hall, V. V. Diev, R. Haiges, G. Wei, X. Xiao, P. I. Djurovich, S. R. Forrest, M. E. Thompson, *Chem. Mater.* **2011**, *23*, 4789−4798.

42. H. Chen, M. S. Farahat, K. Y. Law, D. G. Whitten, *J. Am. Chem. Soc.* **1996**, *118*, 2584−2594.

43. S. Bruck, C. Krause, R. Turrisi, L. Beverina, S. Wilken, W. Saak, A. Lutzen, H. Borchert, M. Schiek, J. Parisi, *Phys. Chem. Chem. Phys.* **2014**, *16*, 1067−1077.

44. M. Tian, M. Furuki, I. Iwasa, Y. Sato, L. S. Pu, S. Tatsuura, *J. Phys. Chem. B* **2002**, *106*, 4370−4376.

45. G. Chen, H. Sasabe, Y. Sasaki, H. Katagiri, X. F. Wang, T. Sano, Z. Hong, Y. Yang, J. Kido, *Chem. Mater.* **2014**, *26*, 1356−1364.

46.   Y. Law, *J. Phys. Chem.* **1987**, *91*, 5184−5193.

47.   X. D. Liu, R. Sun, J. F. Ge, Y. J. Xu, Y. Xu, J. M. Lu, *Org. Biomol. Chem.* **2013**, *11*, 4258−4264.

48.   APEX2 (2009.11−0). Program for Bruker CCD X-ray Diffractometer Control Bruker AXS Inc.: Madison, WI, USA, 2009.

49.   G. M. Sheldrick, *Acta Crystallogr., Sect. A: Found. Adv.* **2015**, *71*, 3−8.

50.   G. M. Sheldrick, *Acta Crystallogr., Sect. C: Struct. Chem.* **2015**, *71*, 3−8.

51.   V. Dolomanov, L. J. Bourhis, R. J. Gildea, J. A. K. Howard, H. Puschmann, *J. Appl. Crystallogr.* **2009**, *42*, 339−341.

52.   P. Emsley, K. Cowtan, *Acta Crystallogr., Sect. D: Biol. Crystallogr.* **2004**, *60*, 2126−2132.

53.   M. Barkauskas, V. Martynaitis, A. Šačkus, R. Rotomskis, V. Sirutkaitis, M. Vengris, *J. Phys.* **2008**, *48*, 231−242.

54.   Redeckas, V. Voiciuk, R. Steponavičiūtė, V. Martynaitis, A. Šačkus, M. Vengris, *J. Photochem. Photobiol. A*, **2014**, *285*, 7−15.

55.   M. Sheik-Bahae, A. A. Said, T. H. Wei, D. J. Hagan, E. W. Van Stryland, *IEEE J. Quantum Electron.* **1990**, *26*, 760−769.

56.   A. Ajayaghosh, P. Chithra, R. Varghese, *Angew. Chem., Int. Ed.* **2007**, *46*, 230−233.

57.   L. Hu, Z. Yan, H. Xu, *RSC Adv.* **2013**, *3*, 7667− 7676.

58.   Y. Law, *J. Phys. Chem.* **1995**, *99*, 9818−9824.

59.   T. Chen, S. R. Marder, L. T. Cheng, *J. Am. Chem. Soc.* **1994**, *116*, 3117−3118.

60.   P. M. Kazmaier, G. K. Hamera, R. A. Burt, *Can. J. Chem.* **1990**, *68*, 530−536.

61.   L. Tong, P. Bi-Xian, B. Fenglian, *Dyes Pigm.* **1999**, *43*, 67−71.

62.   Yang, Y. Zhu, Y. Jiao, D. Yang, Y. Chen, J. Wu, Z. Lu, S. Zhao, X. Pu, Y. Huang, *Dyes Pigm.* **2017**, *145*, 222−232.

63.   A. Ajayaghosh, E. Arunkumar, *Org. Lett.* **2005**, *7*, 3135−3138.

64.   W. Dirk, W. C. Herndon, F. Cervantes-Lee, H. Selnau, S. Martinez, P. Kalamegham, A. Tan, G. Campos, M. Velex, *J. Am. Chem. Soc.* **1995**, *117*, 2214−2225.

65.   A. Karpenko, M. Collot, L. Richert, C. Valencia, P. Villa, Y. Mely, M. Hibert, D. Bonnet, A. S. Klymchenko, *J. Am. Chem. Soc.* **2015**, *137*, 405−412.

66.   J. Hestand, C. Zheng, A. R. Penmetcha, B. Cona, J. A. Cody, F. C. Spano, C. J. Collison, *J. Phys. Chem. C* **2015**, *119*, 18964−18974.

67.   V. Ros-Lis, R. Martinez-Manez, J. Soto, L. A. Villaescusa, K. Rurack, *J. Mater. Chem.* **2011**, *21,* 5004−5010.

68.   K. D. Belfield, C. D. Andrade, C. O. Yanez, M. V. Bondar, F. E. Hernandez, O. V. Przhonska, *J. Phys. Chem. B* **2010**, *114*, 14087−14095.

69.   C. Toro, L. D. Boni, S. Yao, J. P. Ritchie, A. E. Masunov, K. D. Belfield, F. E. Hernandez, *J. Chem. Phys.* **2009**, *130*, 214504.

70.   R. S. Stoll, N. Severin, J. P. Rabe, S. Hecht, *Adv. Mater.* **2006**, *18*, 1271−1275.

71.   K. D. Belfield, M. V. Bondar, H. S. Haniff, I. A. Mikhailov, G. Luchita, O. V. Przhonska, *Chem-PhysChem* **2013**, *14*, 3532−3542.

72.   S. Webster, D. Peceli, H. Hu, L. A. Padilha, O. V. Przhonska, A. E. Masunov, A. O. Gerasov, A. D. Kachkovski, Y. L. Slominsky, A. I. Tolmachev, et al. *J. Phys. Chem. Lett.* **2010**, *1*, 2354−2360.

73.   L. Horng, J. A. Gardecki, A. Papazyan, M. Maroncelli, *Revisited. J. Phys. Chem.* **1995**, *99*, 17311−17337.

74.   T. Liu, M. V. Bondar, K. D. Belfield, D. Anderson, A. E. Masunov, D. J. Hagan, E. W. V. Stryland, *J. Phys. Chem. C* **2016**, *120,* 11099−11110.

75.   S. A. Odom, S. Webster, L. A. Padilha, D. Peceli, H. Hu, G. Nootz, S. J. Chung, S. Ohira, J. D. O. V. Matichak, Przhonska, et al. *J. Am. Chem. Soc.* **2009**, *131*, 7510−7511.

76.   J. Fu, L. A. Padilha, D. J. Hagan, E. W. Van Stryland, O. V. Przhonska, M. V. Bondar, Y. L. Slominsky, A. D. Kachkovski, *J. Opt. Soc. Am. B* **2007**, *24*, 67−76.

77.   M. Della Pelle, P. J. Homnick, Y. Bae, P. M. Lahti, *J. Phys. Chem. C* **2014**, *118*, 1793−1799.

78. D. Yang, L. Yang, Y. Huang, Y. Jiao, T. Igarashi, Y. Chen, Z. Lu, X. Pu, H. Sasabe, J. Kido, *ACS Appl. Mater. Interfaces* **2015**, *7*, 13675−13684.

79. J. Kim, Y. S. Kwon, W. S. Shin, S. J. Moon, T. Park, *Macromolecules* **2011**, *44*, 1909−1919.

80. T. Liu, L. Ding, G. He, Y. Yang, W. Wang, Y. Fang, *ACS Appl. Mater. Interfaces* **2011**, *3*, 1245−1253.

81. T. Liu, K. Zhao, K. Liu, L. Ding, S. Yin, Y. Fang, *J. Hazard. Mater.* **2013**, *246−247*, 52−60.

82. F. Terenziani, A. Painelli, C. Katan, M. Charlot, *J. Am. Chem. Soc.* **2006**, *128*, 15742−15755.

83. C. Sissa, F. Terenziani, A. Painelli, R. Bhaskar Kanth Siram, S. Patil, *J. Phys. Chem. B* **2012**, *116*, 4959−4966.

84. K. M. Shafeekh, S. Das, C. Sissa, A. Painelli, *J. Phys. Chem. B* **2013**, *117*, 8536−8546.

85. J. Fu, L. A. Padilha, D. J. Hagan, E. W. Van Stryland, O. V. Przhonska, M. V. Bondar, Y. L. Slominsky, A. D. Kachkovski, *J. Opt. Soc. Am. B* **2007**, *24*, 67−76.

86. C. Sissa, P. Mohamadzadeh Jahani, Z. G. Soos, A. Painelli, *ChemPhysChem* **2012**, *13*, 2795−2800.

87. X. Yue, A. R. Morales, G. W. Githaiga, A. W. Woodward, S. Tang, J. Sawada, M. Komatsu, X. Liu, K. D. Belfield, *Org. Biomol. Chem.* **2015**, *13*, 10716−10725.

88. C. O. Yanez, A. R. Morales, X. Yue, T. Urakami, M. Komatsu, T. A. H. Järvinen, K. D. Belfield, *PLoS One* **2013**, *8*, No. e67559.

89. X. Wang, A. R. Morales, T.Urakami, L. Zhang, M. V. Bondar, M. Komatsu, K. D. Belfield, *Bioconjugate Chem.* **2011**, *22*, 1438−1450.

90. M.-H. Ha-Thi, M. Penhoat, D. Drouin, M. Blanchard-Desce, V. Michelet, I. Leray, *Chem. − Eur. J.* **2008**, *14*, 5941−5950.

91. H. Maeda, D. L. Tierney, P. S. Mariano, M. Banerjee, D. Cho, U. Yoon, *Tetrahedron* **2008**, *64*, 5268.

92.   M. Zhang, Yu, F. Li, M. Zhu, M. Li, Y. Gao, L. Li, Z. Liu, J. Zhang, D. Zhang, T. Yi, C. Huang, *J. Am. Chem. Soc.* **2007**, *129*, 10322−10323.

93.   X. Yue, C. O. Yanez, S. Yao, K. D. Belfield, *J. Am. Chem. Soc.* **2013**, *135*, 2112−2115.

94.   A. Fadhel, X. Yue, E. H. G. Zadeh, M. V. Bondar, K. D. Belfield*, Int. J. Nanomed.* **2016**, *11*, 6161−6168.

95.   S. Yao, K. J. Schafer-Hales, K. D. Belfield, *Org. Lett.* **2007**, *9*, 5645−5648.

96.   K. D. Belfield, M. V. Bondar, A. R. Morales, X. Yue, G. Luchita, O. V. Przhonska, O. D. Kachkovsky, *ChemPhysChem* **2012**, *13*, 3481−3491.

97.   C. Khaokeaw, M. Sukwattanasinitt, P. Rashatasakhon, *J. Fluoresc.* **2016**, *26*, 745−752.

98.   S. Yao, H. Y. Ahn, X. Wang, J. Fu, E. W. V. Stryland, D. J. Hagan, K. D. Belfield, *J. Org. Chem.* **2010**, *75*, 3965−3974.

99.   Yamada, Y. Hiruta, J. Wang, E. Ayano, H. Kanazawa, *Biomacromolecules* **2015**, *16*, 2356−2362.

100.   L. Cheng, W. He, H. Gong, C. Wang, Q. Chen, Z. Cheng, Z. Liu, *Adv. Funct. Mater.* **2013**, *23*, 5893−5902.

101.   L. Ferrer-Tasies, E. M. Calvo, M. C. Sarabia, M. A. Arzo, A. Angelova, S. Lesieur, S. Ricart, J. Faraudo, N. Ventosa, J. Veciana, *Langmuir* **2013**, *29*, 6519−6528.

102.   I. Cabrera, E. Elizonda, O. Esteban, J. L. Corchero, M. Melgarejo, D. Pulido, A. Cordoba, E. Moreno, U. Unzueta, E. Vazquez, I. Abasolo, S. Schwartz, A. Jr. Villaverde, F. Albericio, M. Royo, M. F. G. Parajo, N. Ventosa, J. Veciana, *Nano Lett.* **2013**, *13*, 3766−3774.

103.   X. Wang, D. M. Nguyen, C. O. Yanez, L. Rodriguez, H. Y. Ahn, M. V. Bondar, K. D. Belfield, *J. Am. Chem. Soc.* **2010**, *132*, 12237−12239.

104.   B. Yapici, Y. Bi, P. Li, X. Chen, X. Yan, S. Mandalapu, M. Faucett, S. Jockusch, J. Ju, K. M. Gibson, W. J. Pavan, L. Bi, *Sci. Rep.* **2015**, *5*, No. 8576.

105.   H. Maes, P. Agostinis, *Mitochondrion* **2014**, *19*, 58−68.

106. A. Thorburn, D. H. Thamm, D. L. Gustafson, *Mol. Pharmacol.* **2014**, *85*, 830−838.

107. X. He, J. Li, S. An, C. Jiang, *Ther. Delivery* **2013**, *4*, 1499−1510.

108. S. E. Kim, M. Overholtzer, *Semin. Cancer Biol.* **2013**, *23*, 329−336.

109. M. Hamasaki, N. Furuta, A. Matsuda, A. Nezu, A. Yamamoto, N. Fujita, H. Oomori, T. Noda, T. Haraguchi, Y. Hiraoka, A. Amano, T. Yoshimori, *Nature* **2013**, *495*, 389−393.

110. L. Hughes, D. E. Gottschling, *Nature* **2012**, *492*, 261−265.

111. X. Chen, Y. Bi, T. Wang, P. Li, X. Yan, S. Hou, C. E. Bammert, J. Ju, K. M. Gibson, W. J. Pavan, L. Bi, *Sci. Rep.* **2015**, *5*, No. 9004.

112. C. D. Andrade, C. O. Yanez, M. A. Qaddoura, X. Wang, C. L. Arnett, S. A. Coombs, J. Yu, R. Bassiouni, M. V. Bondar, K. D. Belfield, *J. Fluoresc.* **2011**, *21*, 1223−1230.

113. E. Elizondo, J. Larsen, N. S. Hatzakis, I. Cabrera, T. Bjornholm, J. Veciana, D. Stamou, N. Ventosa, *J. Am. Chem. Soc.* **2012**, *134*, 1918−1921.

114. J. Peterson, M. Werre, Y. C. Simon, E. B. Coughlin, K. R. Carter, *Macromolecules* **2009**, *42*, 8594−8598.

115. X. G. Liu, W. Sun, *J. Phys. Chem. A* **2014**, *118*, 10318−10325.

116. S. A. Kurhuzenkau, A. W. Woodward, S. Yao, K. D. Belfield, Y. O. Shaydyuk, C. Sissa, M. V. Bondar, A. Painelli, *Phys. Chem. Chem. Phys.* **2016**, *18*, 12839−12846.

117. Y. Zhang, X. Yue, B. Kim, S. Yao, M. V. Bondar, K. D. Belfield, *ACS Appl. Mater. Interfaces* **2013**, *5*, 8710−8717.

118. D. Belfield, A. R. Morales, B. S. Kang, J. M. Hales, D. J. Hagan, E. W. V. Stryland, V. M. Chapela, J. Percino, *Chem. Mater.* **2004**, *16*, 4634−4641.

119. G. M. Cooper, E. H. Robert, The Cell: A Molecular Approach, 6th ed. Sinauer Associates: Sunderland, MA, **2013**, pp 412−416.

120. M. Kalbácová, F. Verdánová, T. Mravec, F. Halasová, M. Pekai, *Colloids Surf., A* **2014**, *460*, 204−208.

121. N. Vlachy, D. Touraud, J. Heilmann, W. Kunz, *Colloids Surf., B* **2009**, *70*, 278−280.

122. B. Sui, X. Liu, M. Wang, K. D. Belfield, *Chem.−Eur. J.* **2016**, *22*, 10351−10354.

123. P. Carmeliet, *Nature.* **2005**, *15*, 932-936.

124. A. Saaristo, T. Karpanen, K. Alitalo, *Oncogene.* **2000**, *19*, 6122-6129.

125. J. Folkman, *Nat. Rev. Drug Discov.* **2007**, *6*, 273-286.

126. H. Hashizume, P. Baluk, S. Morikawa, J. W. McLean, G. Thurston, S. Roberge, R. K. Jain, D. M. McDoanld. *Am. J. Patho.* **2000**, *156*, 1363-1380.

127. C. Brooks, R. A. Clark, D. A. Cheresh, *Science.* **1994**, *264*, 569-571.

128. C. J. Avraamides, B. Garmy-Susini, J. Varner, *Nat. Rev. Cancer.* **2008**, *18*, 604-617.

129. J. D. Hood, D. A. Cheresh, *Nat. Rev. Cancer*, **2002**, *2*, 91-100.

130. E. Ruoslahti, *Annu. Rev. Cell Dev. Biol.* **1996**, *12*, 697-715.

131. M. Pfaff, K. Tangemann, B. Muller, M. Gurrath, G. Muller, H. Kessler, R. Timpl, J. Engel, *J. Biol. Chem.* **1994**, *269*, 20233-20238.

132. A. Dechantsreiter, E. Planker, B. Matha, E. Lohof, G. Holzemann, A. Jonczyk, S. L. Goodman, H. Kessler, *J. Med. Chem.***1999**, *42*, 3033-3040.

133. X. Yue, A. R. Morales, G. W. Githaiga, A. W. Woodward, S. Tang, J. Sawada, M. Komatsu, X. Liu, K. D. Belfield, *Org. Biomol. Chem.* **2015**, *13*, 10716-10725.

134. C. O. Yanez, A. R. Morales, X. Yue, T. Urakami, M. Komatsu, T. A. H. Jarvinen, K. D. Belfield, *PLoS ONE.* **2013** *8*, 67559-67565.

135. K. Chen, X. Chen, *Curr. Top. Med. Chem.* **2010**, *10*, 1227-1236.

136. J. Yum, P. Walter, S. Huber, D. Rentsch, T. Geiger, F. Nuesch. F. D. Angelis, M. Gratzel, M.K. Nazeeruddin, *J. Am. Chem. Soc.* **2007**, *129*, 10320-10321.

137. G. Wei, *et al. Nano Lett.* **2011**, *11*, 4261-4264.

138. C. C. Corredor, Z. Huang, K. D. Belfield, *Adv. Mater.* **2006**, *18*, 2910-2914.

139. C. C. Corredor, Z. Huang, K. D. Belfield, A. R. Morales, M. V. Bondar, *Chem. Mater.* **2007**, *19*, 5165-5173.

140. M. Ha-Thi, *et al. Chem. Eur. J.* **2008**, *14*, 5941-5950.

141. X. Yue, C. O. Yanez, S. Yao, K. D. Belfield, *J. Am. Chem. Soc.* **2013**, *135*, 2112-2115.

142. A. Fadhel, X. Yue, E. H. G. Zadeh, M. V. Bondar, K. D. Belfield, *Int. J. Nanomedicine*. **2016**, *11*, 6161-6168.

143. H. Y. Ahn, S. Yao, X. Wang, K. D. Belfield, *ACS Appl. Mater. Interface.* **2010**, *4*, 2847-2854.

144. G. M. Tozer, *et al. Adv. Drug Deliver Rev.* **2005**, *57*, 135-152.

145. S. Yao, K. J. Schafer-Hales, K. D. Belfield, *Org. Lett.* **2007**, *9*, 5645–5648.

146. C. Khaokeaw, M. Sukwattanasinitt, P. Rashatasakhon, *J. Fluoresc.* **2016**, *26* 745-752.

147. X. Wang, A. R. Moralest, T. Urakami, L. Zhang, M. V. Bondar, M. Komatsu, K. D. Belfield, *Bioconjugate Chem.* **2011**, *22*, 1438-1450.

148. L. Cheng, W. He, H. Gong, C. Wang, Q. Chen, Z. Cheng, Z. Liu, *Adv. Funct. Mater.* **2013**, 23, 5893-5902.

149. A. Vasconcelos, E. Vega, Y. Perez, M. J. Gomara, M. L. Garcia, I. Haro, *Int J Nanomedicine*. **2015**, *10*, 609-631.

150. S. Yao, K. D. Belfield, *Eur. J. Org. Chem.* **2012**, *17*, 3199-3217.

151. J. Yang, S. R. Dave, X. Gao, *J. Am. Chem. Soc.* **2008**, *130*, 5286-5292.

152. D. Corato, A. Quarta, P. Piacenza, A. Raguse, A. Figuerola, R. Bunosanti, R. Cingolani, L. Manna, T. Pellegrino, *J. Mater. Chem.* **2008**, *18*, 1991-1996.

153. W. W. Yu, E. Chang, J. C. Falkner, J. Zhang, A. M. Al-Somat, C. M. Sayes, J. Johns, R. Drezek, V. L. Colvin, *J. Am. Chem. Soc.* **2007**, *129,* 2871-2879.

154. Y. D. Lee, C. K. Lim, S. Kim, I. C. Kwon, J. Kim, *Adv. Funct. Mater.* **2010**, *20*, 2786-2793.

155. Anees, S. Sreejith, A. Ajayaghosh, *J. Am. Chem. Soc.* **2014**, *136*, 13233-13239.

156. M. Tian, M. Furuki, I. Iwasa, Y. Sato, L. S. Pu, S. Tatsuura, *J. Phys. Chem. B.* **2002**, *106*, 4370-4376.

157. J. J. McEwen, K. J. Wallace, *Chem. Commun.* **2009**, *42*, 6339-6351.

158. S. Das, K. G. Thomas, K. J. Thomas, V. Madhavan, *J. Phys. Chem.* **1996**, *100*, 17310-17315.

159. H. Chen, M. Farahat, K. Law, D. Whitten, *J. Am. Chem. Soc.* **1996**, *118*, 2584-2594.

160. H. Chen, W. Herkstroeter, J. Peristein, K. Law, D. Whitten, *J. Phys. Chem.* **1994**, *98*, 5138-5146.

161. K. Liang, K. Y. Law, D. G. Whitten, *J. Phys. Chem.* **1994**, *98*, 13379-13384.

162. L. Beverina, P. Salice, *Eur. J. Org. Chem.* **2010**, *7*, 1207−1225.

163. Y. Zhang, B. Kim, S. Yao, M. V. Bondar, K. D. Belfield, *Langmuir.* **2013**, *29*, 11005-11012.

164. K. Y. Law, *J. Phys. Chem.* **1987**, *91*, 5184-5193.

165. K. D. Belfield, M. V. Bondar, H. Z. Haniff, I. A. Mikhailov, G. Luchita, O. Przhonska, *ChemPhysChem.* **2013**, *14*, 3532-3542.

166. T. Liu, M. V. Bondar, K. D. Belfield, D. Anderson, A. Mansunov, D. J. Hagan, E. W.V. Stryland, *J. Phys. Chem. C.* **2016**, *120*, 11099-11110.

167. M. Sheik-Bahae, A. A. Said, T. Wei, D. J. Hagan, E. W. V. Stryland, *IEEE J. Quantum Elect.* **1990**, *26*, 760-769.

168. S. Webster, *et al. J. Phys. Chem. Lett.* **2010**, *1*, 2354-2360.

169. M. L. Horng, J. A. Gardecki, A. Papazyan, M. Maroncelli, *J. Phys. Chem.* **1995**, *99*, 17311-17337.

170. S. A. Odom, *et al. J. Am. Chem. Soc.* **2009**, *131*, 7510-7511.

171. J. Fu, L. A. Padilha, D. J. Hagan, E. W. V. Stryland, *J. Opt. Soc. Am. B.* **2007**, *24*, 67-76.

172. X. Wang, D. M. Nguyen, C. O. Yanez, L. Rodriguez, H. Ann, M. V. Bondar, K. D. Belfield, *J. Am. Chem. Soc.* **2010**, *132*, 12237-12239.

173. B. Sui, X. Liu, M. Wang, K. D. Belfield, *Chem. Eur. J.* **2016**, *22*, 10351-10354.

174. C. Brooks, A. M. Montgomery, M. Rosenfeld, R. A. Reisfeld, T. Hu, G. Klier, D. A. Cheresh, *Cell*. **1994**, *79*, 1157-1164.

175. L. Hu, Z. Yan, H. Xu, *RSC Adv.* **2013**, *3*, 7667–7676.

176. G. Chen, H. Sasabe, T. Igarashi, Z. Hong, J. Kido, *J. Mater. Chem. A* **2015**, *3*, 14517– 14534.

177. T. Goh, J.-S. Huang, E. A. Bielinski, B. A. Thompson, S. Tomasulo, M. L. Lee, M. Y. Sfeir, N. Hazari, A. D. Taylor, *ACS Photonics* **2015**, *2*, 86–95.

178. D. Yang, Y. Zhu, Y. Jiao, L. Yang, Q. Yang, Q. Luo, X. Pu, Y. Huang, S. Zhao, Z. Lu, *RSC Adv.* **2015**, *5*, 20724–20733.

179. T. Maeda, S. Nitta, H. Nakao, S. Yagi, H. Nakazumi, *J. Phys. Chem. C* **2014**, *118*, 16618–16625.

180. C. C. Corredor, K. D. Belfield, M. V. Bondar, O. V. Przhonska, S. Yao, *J. Photochem. Photobiol. A* **2006**, *184*, 105–112.

181. M. Emmelius, G. Pawlowski, H. W. Vollmann, *Angew. Chem. Int. Ed. Engl.* **1989**, *28*, 1445–1471; *Angew. Chem.* **1989**, *101*, 1475.

182. B. Jipson, C. R. Jones, *J. Vac. Sci. Technol.* **1981**, *18*, 105–109.

183. S. Lee, B. A. Rao, Y.-A. Son, *Sens. Actuators B* **2015**, *210*, 519–532.

184. A. Ajayaghosh, *Acc. Chem. Res.* **2005**, *38*, 449–459.

185. X. D. Liu, R. Sun, J. F. Ge, Y. J. Xu, Y. Xu, J. M. Lu, *Org. Biomol. Chem.* **2013**, *11*, 4258–4264.

186. S. Webster, J. Fu, L. A. Padilha, O. V. Przhonska, D. J. Hagan, E. W. Van Stryland, M. V. Bondar, Y. L. Slominsky, A. D. Kachkovski, *Chem. Phys.* **2008**, *348*, 143–151.

187. K. D. Belfield, M. V. Bondar, H. S. Haniff, I. A. Mikhailov, G. Luchita, O. V. Przhonska, *ChemPhysChem* **2013**, *14*, 3532– 3542.

188. A. Karpenko, A. S. Klymchenko, S. Gioria, R. Kreder, I. Shulov, P. Villa, Y. Mely, M. Hibert, D. Bonnet, *Chem. Commun.* **2015**, *51*, 2960–2963.

189. C. Luo, Q. Zhou, G. Jiang, L. He, B. Zhang, X. Wang, *New J. Chem.* **2011**, *35*, 1128–1132.

190. S. A. Kurhuzenkau, A. W. Woodward, S. Yao, K. D. Belfield, Y. O. S, C. Shaydyuk, M. V. Bondar, A. Painelli, *Phys. Chem. Chem. Phys.* **2016**, *18*, 12839–12846.

191. Y. Zhang, B. Kim, S. Yao, M. V. Bondar, K. D. Belfield, *Langmuir* **2013**, *29*, 11005–11012.

192. T. Liu, M. V. Bondar, K. D. Belfield, D. Anderson, A. E. Masunov, D. J. Hagan, E. W. Van Stryland, *J. Phys. Chem. C* **2016**, *120*, 11099–11110.

193. C. Sun, Q. Liao, T. Li, J. Li, J. Jiang, Z. Xu, X. Wang, R. Shen, D. Bai, Q. Wang, S. Zhang, H. Fu, H. Zhang, *Chem. Sci.* **2015**, *6*, 761– 769.

194. E. Arunkumar, N. Fu, B. D. Smith, *Chem. Eur. J.* **2006**, *12*, 4684–4690.

195. J. J. McEwen, K. J. Wallace, *Chem. Commun.* **2009**, 6339–6351.

196. A. Ajayaghosh, E. Arunkumar, *Org. Lett.* **2005**, *7*, 3135–3138.

197. L. Beverina, R. Ruffo, M. M. Salamone, E. Ronchi, M. Binda, D. Natali, M. Sampietro, *J. Mater. Chem.* **2012**, *22*, 6704–6710.

198. K. Umezawa, D. Citterio, K. Suzuki, *Anal. Sci.* **2008**, *24*, 213–217.

199. S. Paek, H. Choi, C. Kim, N. Cho, S. So, K. Song, M. K. Nazeeruddin, J. Ko, *Chem. Commun.* **2011**, *47*, 2874–2876.

200. H.-Y. Ahn, S. Yao, X. Wang, K. D. Belfield, *ACS Appl. Mater. Interfaces* **2012**, *4*, 2847–2854.

201. W. Xu, X. Zhu, G. Wang, C. Sun, Q. Zheng, H. Yang, N. Fu, *RSC Adv.* **2014**, *4*, 52690–52693.

202. Y. Shiraishi, S. Sumiya, K. Manabe, T. Hirai, *ACS Appl. Mater. Interfaces* **2011**, *3*, 4649–4656.

203. H. Evans, P. D. Beer, *Angew. Chem. Int. Ed.* **2014**, *53*, 11716–11754.

204 H. Evans, P. D. Beer, *Angew. Chem.* **2014**, *126*, 11908.

205. J. Ma, P. K. Dasgupta, *Anal. Chim. Acta* **2010**, *673*, 117–125.

206. Z. Xu, X. Chen, H. N. Kim, J. Yoon, *Chem. Soc. Rev.* **2010**, *39*, 127–137.

207.	S. C. Wei, P. H. Hsu, Y. F. Lee, Y. W. Lin, C. C. Huang, *ACS Appl. Mater. Interfaces* **2012**, *4*, 2652–2658.

208.	X. Lou, Y. Zhang, S. Li, D. Ou, Z. Wan, J. Qin, Z. Li, *Polym. Chem.* **2012**, *3*, 1446–1452.

209.	Z. Ekmekci, M. D. Yilmaz, E. U. Akkaya, *Org. Lett.* **2008**, *10*, 461–464.

210.	Z. Shojaeifard, B. Hemmateenejad, M. Shamsipur, *ACS Appl. Mater. Interfaces* **2016**, *8*, 15177–15186;

211.	W. C. Lin, S. K. Fang, J. W. Hu, H. Y. Tsai, K. Y. Chen, *Anal. Chem.* **2014**, *86*, 4648–4652.

212.	J. Yoshino, N. Kano, T. Kawashima, *J. Org. Chem.* **2009**, *74*, 7496–7503.

213.	J. V. Ros-Lis, B. Garcia, D. Jimenez, R. Martinez-Manez, F. Sancenon, J. Soto, F. Gonzalvo, M. C. Valldecabres, *J. Am. Chem. Soc.* **2004**, *126*, 4064–4065.

214.	J. V. Ros-Lis, R. Martinez-Manez, J. Soto, *Chem. Commun.* **2002**, 2248–2249.

215.	H. S. Hewage, E. V. Anslyn, *J. Am. Chem. Soc.* **2009**, *131*, 13099–13106.

216.	G. Wang, H. Chen, Y. Chen, N. Fu, *Sens. Actuators B* **2016**, *233*, 550–558.

217.	H. Yu, M. Fu, Y. Xiao, *Phys. Chem. Chem. Phys.* **2010**, *12*, 7386–7391.

218.	D. Galliani, L. Mascheroni, M. Sassi, R. Turrisi, R. Lorenzi, A. Scaccabarozzi, N. Stingelin, L. Beverina, *Adv. Opt. Mater.* **2015**, *3*, 1164–1168.

219.	J. R. Lakowicz, *Principles of Fluorescence Spectroscopy*, 3rd ed., Springer, New York, N. Y. **2006**, pp. 353–378.

220.	L. Beverina, P. Salice, *Eur. J. Org. Chem.* **2010**, 7, 1207–1225.

221.	A. Filarowski, M. Kluba, K. Cieslik-Boczula, A. Koll, A. Kochel, L. Pandey, W. M. De Borggraeve, M. Van der Auweraer, J. Catalan, N. Boens, *Photochem. Photobiol. Sci.* **2010**, *9*, 996–1008.

222.	K. D. Belfield, C. D. Andrade, C. O. Yanez, M. V. Bondar, F. E. Hernandez, O. V. Przhonska, *J. Phys. Chem. B* **2010**, *114*, 14087–14095.

223.	C. Toro, L. D. Boni, S. Yao, J. P. Ritchie, A. E. Masunov, K. B. Belfield, F. E. Hernandez, *J. Chem. Phys.* **2009**, *130*, 214504–1–214504–6.

224. K. D. Belfield, M. V. Bondar, O. V. Przhonska, K. J. Schafer, *Photochem. Photobiol. Sci.* **2004**, *3*, 138–141;

225. K. D. Belfield, M. V. Bondar, O. V. Przhonska, K. J. Schafer, *J. Photochem. Photobiol. A* **2004**, *162*, 489–496.

226. S. A. Azim, S. M. Al-Hazmy, E. M. Ebeid, S. A. El-Daly, *Opt. Laser Technol.* **2005**, *37*, 245–249;

227. R. Rosenthal, *Opt. Commun.* **1978**, *24*, 164–166.

228. V. Ros-Lis, R. Martinez-Manez, J. Soto, L. A. Villaescusa, K. Rurack, *J. Mater. Chem.* **2011**, *21*, 5004–5010.

229. Y. Zhang, X. Yue, B. Kim, S. Yao, K. D. Belfield, *Chem. Eur. J.* **2014**, *20*, 7249–7253;

230. D. S. Pisoni, M. P. de Abreu, C. L. Petzhold, F. S. Rodembusch, L. F. Campo, *J. Photochem. Photobiol. A* **2013**, *252*, 77–83;

231. T. Arun, D. Ramaiah, *J. Phys. Chem. A* **2005**, *109*, 5571–5578.

232. S. Mohd Yusof, M. N. Khan, M. Ashokkumar, *J. Phys. Chem. C* **2012**, *116*, 15019–15027;

233. T. J. V. Prazeres, M. Beija, F. V. Fernandes, P. G. A. Marcelino, J. P. S. Farinha, J. M. G. Martinho, *Inorg. Chim. Acta* **2012**, *381*, 181–187;

234. S. Bairu, G. Ramakrishna, *J. Phys. Chem. B* **2013**, *117*, 10484– 10491.

235. T. Liu, L. Ding, G. He, Y. Yang, W. Wang, Y. Fang, *ACS Appl. Mater. Interfaces* **2011**, *3*, 1245–1253;

236. T. Liu, L. Ding, K. Zhao, W. Wang, Y. Fang, *J. Mater. Chem.* **2012**, *22*, 1069– 1077.

237. Y.-K. Yang, J. Tae, *Org. Lett.* **2006**, *8*, 5721–5723;

238. Y. Yang, Q. Zhao, W. Feng, F. Li, *Chem. Rev.* **2013**, *113*, 192–270.

239. P. Anees, S. Sreejith, A. Ajayaghosh, *J. Am. Chem. Soc.* **2014**, *136*, 13233– 13239.

240. U. Oguz, E. U. Akkaya, *J. Org. Chem.* **1998**, *63*, 6059–6060.

241.   I. Adamovskyi, O. S. Artamonov, A. V. Tymtsunik, O. O. Grygorenko, *Tetrahedron Lett.* **2014**, *55*, 5970–5972.

242.   D. Magde, J. H. Brannon, T. L. Cremers, J. Olmsted, *J. Phys. Chem.* **1979**, *83*, 696–699;

243.   S. J. Isak, E. M. Eyring, *J. Phys. Chem.* **1992**, *96*, 1738– 1742.

244.   M. Pawlicki, H. A. Collins, R. G. Denning, H. L. Anderson, *Angew. Chem. Int. Ed*. **2009**, *48*, 3244-3266.

245.   Y. Niko, Moritomo, H. Sugihara, H. Suzuki, Y. Kawamata, J. Konishi, G. A *J. Mater. Chem. B* **2015**, *3*, 184-190.

246.   S. Yao, K. D. Belfield, *Eur. J. Org. Chem*. **2012**, *12*, 3199-3217.

247.   D. Kim, H. G. Ryu, K. H. Ahn, *Org. Biomol. Chem*. **2014**, *12*, 4550-4566.

248.   J. J. McEwen, K. J. Wallace, *Chem. Commun*. **2009**, *6*, 6339-6351.

249.   T. Liu, M. V. Bondar, K. D. Belfield, D. Anderson, A. E. Masunov, D. J. Hagan, E. W. V.Stryland, *J. Phys. Chem. C* **2016**, *120*, 11099-11110.

250.   C. L. Sun, Q. Liao T. Li, J. Li, J. Q. Jiang, Z. Z. Xu, X. D. Wang, R. Shen, D. C. Bai, Q. Wang, et al. *Chem. Sci.* **2015**, *6*, 761-769.

251.   S. Lee, B. A. Rao, Y.-A. Son, *Sens. Actuators B* **2015**, *210*, 519-532.

252.   A. Ajayaghosh, *Acc. Chem. Res*. **2005**, *38*, 449-459.

253.   H. Y. Ahn, S. Yao, X. Wang, K. D. Belfield, *ACS Appl. Mater. Interfaces* **2012**, *4*, 2847-2854.

254.   C. Luo, Q. Zhou, G. Jiang, L. He, B. Zhang, X. Wang, *New J. Chem*. **2011**, *35*, 1128-1132.

255.   E. Arunkumar, P. K. Sudeep, P. V. Kamat, B. C. Nolla, B. D. Smith, *New J. Chem*. **2007**, *31*, 677-683.

256.   D. P. Ferreira, D. S. Conceição, F.Fernandes, T.Sousa, R. C. Calhelha, I. C. Ferreira, F. R. Santos, L. F. V. Ferreira, *J. Phys. Chem. B* **2016**, *120*, 1212-1220.

257.   R. R. Avirah, D. T. Jayaram, N. Adarsh, D. Ramaiah, *Org. Biomol. Chem*. **2012**, *10*, 911-920.

258. Y. Zhang, B. Kim, S. Yao, M. V. Bondar, K. D. Belfield, *Langmuir* **2013**, *29*, 11005-11012.

259. J. R. Johnson, N. Fu, E. Arunkumar, W. M. Leevy, S. T. Gammon, *Angew. Chem. Int. Ed. Eng.* **2007**, *46*, 5528-5531.

260. J. M. Baumes, J. J. Gassensmith, J. Giblin, J. J. Lee, A. G. White, W. J. Culligan, W. M. Leevy, M. Kuno, B. D. Smith, *Nat. Chem.* **2010**, *2*, 1025-1030.

261. H. Chen, M. S. Farahat, K.-Y. Law, D. G. Whitten, *J. Am. Chem. Soc.* **1996**, *118*, 2584-2594.

262. G. Chen, H. Sasabe, Y. Sasaki, H. Katagiri, X.-F. Wang, T. Sano, Z. Hong, Y. Yang, J. Kido, *Chem. Mater.* **2014**, *26*, 1356-1364.

263. E. Arunkumar, C. C. Forbes, B. C. Noll, B. D. Smith, *J. Am. Chem. Soc.* **2005**, *127*, 3288-3289.

264. S. Y. Hsueh, C. C. Lai, Y. H. Liu, Y. Wang, S. M. Peng, S. H. Chiu, *Org. Lett.* **2007**, *9*, 4523-4526.

265. K. D. Belfield, M. V. Bondar, H. S. Haniff, I. A. Mikhailov, G. Luchita, O. V. Przhonska, *Chemphyschem* **2013**, *14*, 3532-3542.

266. K. T. Arun, D. Ramaiah, *J. Phys. Chem. A* **2005**, *109*, 5571-5578.

267. Y. Zhang, M. Jiang, G. Han, K. Zhao, B. Z. Tang, K. S. Wong, *J. Phys. Chem. C* **2015**, *119*, 27630-27638.

268. K. Y. Law, *J. Phys. Chem.* **1995**, *99*, 9818-9824.

269. K. T. Arun, D. T. Jayaram, R. R. Avirah, D. Ramaiah, *J. Phys. Chem. B* **2011**, *115*, 7122-7128.

270. E. Arunkumar, N. Fu, B. D. Smith, *Chem. Eur. J. Chem.* **2006**, *12*, 4684-4690.

271. J. M. W. Chan, J. R. Tischler, S. E. Kooi, V. Bulović, T. M. Swager, *Chem. Soc.* **2009**, *131*, 5659-5666.

272. F. Würthner, *Chem. Commun.* **2004**, 1564-1579.

273. B. Jin, X. Zhang, W. Zheng, X. Liu, J. Zhou, N. Zhang, F. Wang, D. Shangguan, *Anal. Chem.* **2014**, *86*, 7063-7070.

274.   U. Oguz, E. U. Akkaya, *J. Org. Chem.* **1998**, *63*, 6059-6060.

275.   J. R. Lakowicz in *Principles of Fluorescence Spectroscopy*, Springer *&* Business Media, New York, **1999**, pp. 150-300.

276.   S. Das, K. G. Thomas, R. Ramanathan, M. V. George, P. V. Kamat, *J. Phys. Chem*. **1993**, *97*, 13625-13628.

277.   S. A. Odom, S. Webster, L. A. Padilha, D. Peceli, H. Hu, G. Nootz, S. J. Chung, S. Ohira, J. D. Matichak, O. V. Przhonska, et al. *J. Am. Chem. Soc.* **2009**, *131*, 7510-7511.

278.   S. Webster, D. Peceli, H. Hu, L. A. Padilha, O. V. Przhonska, A. E. Masunov, A. Gerasov, O. Kachkovski, A. D. Slominsky, Y. L. Tolmachev, et al. *J. Phys. Chem. Lett.* **2010**, *1*, 2354-2360.

279.   J. Fu, L. A. Padilha, D. J. Hagan, E. W. Van Stryland, O. V. Przhonska, M. V. Bondar, Y. L. Slominsky, A. D. Kachkovski, *J. Opt. Soc. Am. B* **2007,** *24*, 67-76.

280.   G. Miguel. M. Marchena, M. Zitnan, S. Pandey, S. Hayase, S. Douhal, A. Femto, *Phys. Chem. Chem. Phys*. **2012**, *14*, 1796-1805.

281   J. R. Lakowicz, *Principles of Fluorescence Spectroscopy*, 3ʳᵈ Edition, Springer, New York, N. Y. **2006**.

282.   E. Arunkumar, P. Chithra, A. Ajayaghosh, *J. Am. Chem. Soc*. **2004**, *126*, 6590-6598.

283.   C. Zheng, A. R. Penmetcha, B. Cona, S. D. Spencer, B. Zhu, P. Heaphy, J. A. Cody, C. J. Collison, *Langmuir* **2015**, *31*, 7717-7726.

284.   V. V. Prokhorov, O. M. Perelygina, S. I. Pozin, E. I. Mal'tsev, A. V. Vannikov, *J. Phys. Chem. B* **2015**, *119*, 15046-15053.

285.   S. Biswas, H. -Y. Ahn, M. V. Bondar, K. D. Belfield, *Langmuir* **2012**, *28*, 1515-1522.

286.   N. J. Hestand, C. Zheng, A. R. Penmetcha, B. Cona, J. A. Cody, F. C. Spano, C. J. Collison, *J. Phys. Chem. C* **2015**, *119*, 18964-18974.

287.   C. W. Dirk, W. C. Herndon, F. Cervantes-Lee, H. Selnau, S. Martinez, P. Kalamegham, A. Tan, G. Campos, M. Velez, J. Zyss, I. Ledoux, et al. *J. Am. Chem. Soc*. **1995**, *117*, 2214-2225.

288. T. T. Vu, M. Dvorko, E. Y. Schmidt, J. F. Audibert, P. Retailleau, B. A. Trofimov, R. B. Pansu, G. Clavier, R. Méallet-Renault, *J. Phys. Chem. C* **2013**, *117*, 5373-5385.

289. K. Cai, J. Xie, D. Zhao, *J. Am. Chem. Soc.* **2014**, *136*, 28-31.

290. M. Gsänger, E. Kirchner, M. Stolte, C. Burschka, V. Stepanenko, J. Pflaum, F. Würthner, *J. Am. Chem. Soc.* **2014**, *136*, 2351-2362.

291. S. Wang, L. Hall, V. V. Diev, R. Haiges, G. Wei, X. Xiao, P. I. Djurovich, S. R. Forrest, M. E. Thompson, *Chem. Mater.* **2011**, *23*, 4789-4798.

292. M. Xu, S. Wu, F. Zeng, C. Yu, *Langmuir* **2010**, *26*, 4529-4534.

293. W. C. Cromwell, K. Bystrom, M. R. Eftink, *J. Phys. Chem.* **1985**, *89*, 326-332.

294. W. Pu, Y. Yang, B. Wei, C. Yuan, *Ind. Eng. Chem. Res.* **2016**, *55*, 8679-8689.

295. X. Ma, Y. Zhao, *Chem. Rev.* **2015**, *115*, 7794-7839.

296. W. Xu, X. Zhu, G. Wang, C. Sun, Q. Zheng, H. Yang, N. Fu, *RSC Adv.* **2014**, *4*, 52690-52693.

297. M. Hariharan, P. P. Neelakandan, D. Ramaiah, *J. Phys. Chem. B* **2007**, *111*, 11940-11947.

298. J. J. Michels, J. Huskens, D. N. Reinhoudt, *J. Am. Chem. Soc.* **2002**, *124*, 2056-1064.

299. N. Hobeika, J. P. Malval, H. Chaumeil, V. Roucoules, F. Morlet-Savary, D. L. Nouen, F. Gritti, *J. Phys. Chem. A* **2012**, *116*, 10328-10337.

300. L. Wang, C. Zhong, P. Xue, E. Fu, *J. Org. Chem.* **2011**, *76*, 4874-4883.

301. K. Zhao, T. Liu, G. Wang, X. Chang, D. Xue, K. D. Belfield, Y. Fang, *J. Phys. Chem. B* **2013**, *117*, 5659-5667.

302. B. Sui, X. Liu, M. Wang, K. D. Belfield, *Chem. Eur. J.* **2016**, 22, 10351-10354.

303. X. Liu, A. Ardizzone, B. Sui, M. Anzola, N. Ventosa, T. Liu, J. Veciana, K. D. Belfield, *ACS Omega* **2017**, *2*, 4112-4122.